

**SHOCK-TURBULENCE INTERACTIONS AT HIGH TURBULENCE
INTENSITIES: THEORY AND DIRECT NUMERICAL
SIMULATIONS**

A Dissertation

by

CHANG-HSIN CHEN

Submitted to the Office of Graduate and Professional Studies of
Texas A&M University
in partial fulfillment of the requirements for the degree of

DOCTOR OF PHILOSOPHY

Chair of Committee,	Diego A. Donzis
Committee Members,	Rodney D. W. Bowersox
	Sharath S. Girimaji
	Simon W. North
Head of Department,	Rodney D. W. Bowersox

December 2018

Major Subject: Aerospace Engineering

Copyright 2018 Chang-Hsin Chen

ABSTRACT

The interaction of turbulence with shock waves, while very common in nature and engineered systems, is a very difficult problem from a theoretical, numerical and experimental perspective. A main challenge comes from the two-way coupling between the shock and turbulence which occurs over a wide range of scales in time and space. As a result, many investigations have resorted to strong simplifications such as the linearization of the governing equations or the assumption of mean conditions across the shock independent of turbulent fluctuations. When the interaction is strong, a condition that is realized when turbulence is relatively intense, much less is known about the behavior of both the shock and turbulence. The focus of this work, thus, is on shock-turbulence interactions (STI) at high turbulent intensities using high-fidelity direct numerical simulations (DNS) that fully resolve the shock. Highly accurate methods are developed to simulate a stationary normal shock as the turbulent flow passes through the domain and used to generate a massive highly resolved database at a wide range of conditions. The numerical study is guided by novel theoretical work that result in analytical expressions for thermodynamic jumps across the shock that, unlike previous results in the literature, depend on turbulence characteristics. Comparison with DNS data shows that these expressions can indeed predict quantitatively a number of statistical variables of interest. The theory also predicts the emergence of new regimes of the interaction which results in distinct amplification or attenuation of different variables depending on governing parameters. This previously unseen behavior is verified against DNS as well. Results on the

shock structure are used to validate previous theoretical proposals and extend the analysis to much stronger interactions which leads to the observation of a new regime (a vanished regime in addition to the well-known wrinkled and broken regimes) in which turbulence undergoes a classical spatial decay as it crosses the shock. Finally, the amplification of turbulence across the shock is studied using our DNS results as well as the large collection available in the literature. Disagreements in the literature on Reynolds stresses are resolved by recognizing a special kind of similarity scaling on two different parameters in two different limits. This analysis reconciles apparently contradicting results in the literature. This analysis is extended to other quantities of interest such as enstrophy and mass flux with similar success.

To my father and mother,
Yen-Dan Chen and Kuei-Fang Liu,
whose endurance made this possible.

ACKNOWLEDGMENTS

This work is supported by Air Force of Scientific Research (AFOSR) and National Science Foundation (NSF). The computational resources for present simulations were provided by Extreme Science and Engineering Discovery Environment (XSEDE), Texas Advanced Computing Center (TACC), Texas A&M High performance Research Computing, Argonne National Laboratory, The National Institute for Computational Sciences (NICS) and Oak Ridge National Laboratory.

I would like to express my deepest gratitude to Prof. Donzis for guiding me through my PhD. It has been a wonderful journey being a part of his team. He is a great scientist with extensive knowledge of science and computation expertise, but his characters have made him a lifelong role model for me. I have seen so many times how he transformed a crisis into an opportunity; how he brought hope into a hopeless situation. In the beginning, I thought this PhD is a lesson of research, but it is actually a lesson of life. There is no word to describe how thankful I am to Prof. Donzis who gave me a chance when I haven't proven myself, who trusted me when he hasn't met me. It is truly my honor to work for him.

I am thankful for the opportunity I have to interact with distinguished scholars. A special thank goes to Drs. Bowersox, Girimaji and North for serving in my thesis committee and for sharing with me their professional knowledge in many aspects of research. I would also like to thank Drs. Larsson and Pantano who shared their expertise in shock waves and turbulence with me.

I would like to give a big thanks to the professional staff in my Department, Ms.

Knabe, Ms. Marianno, Ms. Leatherman and Ms. Rowe. Their timely help and generous support have made my studies much easier than it could be. I would also like to express my gratitude to the Scholarships and Financial Aids Department in Texas A&M University for the constant support with grants.

My friends in Antioch Community Church have been a great company in the past few years. The discipleship and life group are important to my life. To all the labmates, Agustin, Shriram, Aditya, John, Sualeh, Komal, Akanksha and Biswajeet. It is a pleasure to work with them. I am specially thankful to Shriram, Agustin and Aditya. They have offered so much help and beer that I will always remember. To a great friend, Zach Harris, whose friendship has been a blessing to me and keeps me in his prayer. To another great friend, Jonathan Ben Benjamin, whose companionship has been a grace to me. To Mona Karimi, Steven Anderson and Bryan Zak, who shared with me their work experience.

This work cannot be accomplished without my family. I am truly grateful for all the support from my father and mother. They teach me to be a good man, and they inspire me to be a better man I can be. It is their sacrifices that built up my life. I will always remember the siblinship with my sister, Bernice. The time we had together truly enriched my life. To my little sister, Hurley who has been a blessing in my life. She has shared a lot of patience and compassion in times of need and lots of joy to brighten up my days. To all the relative, Uncles Lii, Yang and Liu, Aunts Lii, Yang and Liu, and Jonathan, Cathy, Eric, Alice, Emily and Daniel. Thank you for always open your houses for me. Your compnay is a great support in my research.

Finally, all the thanks to my God who created the heavens and the earth, who saves me from the dark and leads me in his light. Thank you Lord.

CONTRIBUTORS AND FUNDING SOURCES

Contributors

This work was supervised by a dissertation committee consisting of Professors Donzis (advisor), Bowersox, and Girimaji of the Department of Aerospace Engineering, and Professor North of the Department of Chemistry.

All the work conducted for the thesis was completed by the student under the guidance of the advisor, Dr. Donzis.

Funding Sources

The study was supported by an assistantship from Texas A&M University, and grants from Air Force of Scientific Research (AFOSR), and National Science Foundation (NSF).

TABLE OF CONTENTS

	Page
ABSTRACT	ii
DEDICATION	iv
ACKNOWLEDGMENTS	v
CONTRIBUTORS AND FUNDING SOURCES	vii
TABLE OF CONTENTS	viii
LIST OF FIGURES	x
LIST OF TABLES	xvi
I. INTRODUCTION	1
I.A Turbulence and Shock Waves: An Overview	1
I.B Background and Literature Review: Shock-turbulence Interactions	3
I.C Objective of Present Work	11
II. DIRECT NUMERICAL SIMULATIONS	12
II.A Model Descriptions	12
II.A.1 Governing equations	12
II.A.2 Shock Stabilization and Boundary Conditions	13
II.B Turbulence Generation	16
II.B.1 Forcing scheme	16
II.B.2 Isotropic and anisotropic turbulence	17
II.C Numerical Algorithm	18
II.C.1 Temporal derivatives	18
II.C.2 Spatial derivatives	20
II.D Averages and Characteristic Locations	30
II.E Resolution and DNS Database	37
III. TURBULENT SHOCK JUMPS OF THERMODYNAMIC VARIABLES ...	44
III.A Theoretical Background: Quasi-equilibrium Assumption and Truncated Integrals	44

	Page
III.B Turbulence Shock Jumps of Thermodynamic Quantities	53
III.C Summary	74
IV. SHOCK STRUCTURE	76
IV.A Scaling of Rms-to-mean Shock Dilatation	76
IV.B A New Regime: Vanished Shocks.....	79
IV.C Rms-to-mean Dilatation Beyond Wrinkled Shocks	85
IV.D Truncated Integrals on Dilatation	87
IV.E Summary	92
V. TURBULENCE AMPLIFICATION	94
V.A Reynolds Stresses	95
V.B Enstrophy	103
V.C Kolmogorov Length Scale and Viscous Dissipation.....	108
V.D Mass Flux Variance.....	111
V.E Thermodynamic Quantities	115
V.F Summary	117
VI. CONCLUSIONS AND FUTURE WORK	118
VI.A Conclusions.....	118
VI.B Future Work	123
REFERENCES	125
APPENDIX A. EXPLICIT SOLUTIONS OF LIA	132

LIST OF FIGURES

FIGURE	Page
II.1 A schematic of shock interacts with (a) isotropic turbulence and (b) anisotropic turbulence in the computational domains.	14
II.2 Grid independence tests with sixth order scheme (solid) and tenth order scheme (dashed) for (a) amplification factors, and (b) rms-to-mean ratio of dilatation.	31
II.3 Typical streamwise distribution of (a) Reynolds stress R_{11} and (b) pressure both normalized by their upstream value at $M = 1.2$, $R_\lambda \approx 25$, and $M_t = 0.21$	34
II.4 Normalized distributions of Reynolds stress R_{11} (solid), transverse enstrophy Ω_{22} (dashed), mass flux variance J_{11} (thick dashed), dissipation ϵ (dotted) and Kolmogorov length scale η (dash-dotted) at $M = 1.2$, $R_\lambda \approx 25$ and $M_t = 0.21$. Same vertical dashed lines as in figure II.3.	34
II.5 Location of minimum in Reynolds stresses and maximum of pressure both downstream of the shock ($x_{2'_{R11}}$ and $x_{2'_p}$, respectively) relative to x_1 with $M = 1.1$ (circles), $M = 1.2$ (squares) and $M = 1.4$ (diamonds). Dashed lines with slope for reference. Different tones of grays represent different values of R_λ from 5 (lightest) to 65 (darkest).	36
II.6 Grid-independence test with different $\delta_l/\Delta x$ at $M = 1.1$, $M_t = 0.21$ and $R_\lambda \approx 25$ for (a) amplification factor and (b) rms-to-mean dilatation. The dashed line represents $\delta_l/\Delta x = 4.5$	41
II.7 Distribution of R_{11} at $M = 1.2$, $M_t = 0.23$ and $R_\lambda \approx 10$ with $\Delta = 0.5\pi$ (\bullet), 1.1π (dashed), 2.2π (dash-dotted) and 3.3π (dotted)	42
II.8 Test of distance between shock and sponges for (a) G and (b) Θ at $M = 1.2$, $M_t = 0.23$ and $R_\lambda \approx 10$	43
III.1 Perturbations in a flow with a moving wave	44

- III.2 Even moments of (a) velocity fluctuation $\langle u'^n \rangle / \langle u'^2 \rangle^{n/2}$ and (b) Mach number fluctuation $\langle m^n \rangle / \langle m^2 \rangle^{n/2}$ as function of K at location 1 for all the simulations in tables II.1 and II.2: $M = 1.1$ (circles), $M = 1.2$ (squares), and $M = 1.4$ (diamonds). Open and closed symbols are for IT and SDT simulations. From bottom to top $n = 4, 6$, and 8 . Dashed lines correspond to Gaussian values at $3, 15$ and 105 , respectively. 52
- III.3 Probability of subsonic regions upstream of the shock. Solid line: theoretical $P_s = P(m < -\Delta M)$ with Gaussian p.d.f. for m . Symbols for DNS data at $R_\lambda \approx 5$ (stars), $R_\lambda \approx 10$ (circles), $R_\lambda \approx 25$ (squares), $R_\lambda \approx 45$ (diamonds), and $R_\lambda \approx 65$ (plus signs). Open and closed symbols are for IT and SDT simulations, respectively. Gray dashed line at $M_t/\Delta M = 0.6$ for reference. 54
- III.4 (a) Pressure and (b) density profile of normal shocks interacting with isotropic turbulence at $M = 1.2$, $R_\lambda \approx 25$ and $M_t = 0.12$ (solid), 0.21 (dashed), 0.32 (dashed-dotted) and 0.44 (dotted). Gray lines correspond to the laminar inviscid limit, namely, RH jumps. 55
- III.5 Mean density jumps from IT (squares) and SDT (circle) simulations at $M = 1.1$ (dark), 1.2 (medium) and 1.4 (light). Other symbols are for Larsson & Lele (2009) (∇), and Larsson *et al.* (2013) (\triangleleft). Solid lines correspond to the analytical solution Eq. (III.33) at $M = 1.1, 1.2, 1.28, 1.4, 1.5$ and 1.87 (bottom to top). Gray dashed line at $M_t/\Delta M = 0.6$ separates the wrinkled (W) and broken (B) regimes. Vanished regime lines at $R_\lambda \approx 5$ (V_5) and $R_\lambda \approx 65$ (V_{65}) also included as gray dashed lines. 58
- III.6 Mean pressure and temperature jumps from IT (squares) and SDT (circles) simulations, Lee *et al.* (1993) (\triangleright) and Larsson *et al.* (2013) (\triangleleft). Solid lines correspond to the analytical solution (III.38) at $M = 1.1, 1.2, 1.4$, and 1.5 (bottom to top). Gray dashed line at $M_t/\Delta M = 0.6$ separates the wrinkled (W) and broken (B) regimes. Vanished regime lines at $R_\lambda \approx 5$ (V_5) and $R_\lambda \approx 65$ (V_{65}) also included as gray dashed lines. 63

- III.7 Relative departures from laminar RH jumps for (a) density $R_\rho(M, M_t)$, (b) pressure $R_p(M, M_t)$, and (c) temperature $R_T(M, M_t)$ at $M_t = 0.1, 0.3, 0.5$, and 0.8 . Gray dashed line at $M_t/\Delta M = 0.6$ separates the wrinkled (W) and broken (B) regimes. Vanished regime lines at $R_\lambda \approx 5$ (V_5) and $R_\lambda \approx 65$ (V_{65}) also included as gray dashed lines. 65
- III.8 (a) Critical Mach numbers ($M_{cr}^X(M_t)$) for density ($X = \rho$, solid), pressure ($X = p$, dashed), and temperature ($X = T$, dashed-dotted). Gray dashed line at $M_t/\Delta M = 0.6$ separates the wrinkled (W) and broken (B) regimes. Vanished regime lines at $R_\lambda \approx 5$ (V_5) and $R_\lambda \approx 65$ (V_{65}) also included as gray dashed lines. (b) Maximum weakening of shock jumps due to turbulence measured as the maximum relative departure from RH relations for density ($X = \rho$, solid), pressure ($X = p$, dashed), and temperature ($X = T$, dash-dotted) for a given M_t 66
- III.9 Variation of normalized pressure (solid, $q = p$), density (dashed, $q = \rho$) and temperature (dash-dotted, $q = T$) across the shock. (a) $(M, M_t, R_\lambda) \approx (1.2, 0.39, 13)$ which corresponds to $M < M_{cr}^T$ and $M > M_{cr}^p, M_{cr}^\rho$. Inset: detailed view of temperature around $x_{2'}$. (b) $(M, M_t, R_\lambda) \approx (1.1, 0.29, 10)$ which corresponds to $M < M_{cr}^T, M_{cr}^p, M_{cr}^\rho$. Grey solid lines represent the laminar inviscid limits. Vertical grey dashed lines indicate the location of $x_{2'}$ 67
- III.10 Theoretical solution of density jump from Eq. (III.33) in terms of M and M_t 68
- III.11 Mean entropy increase from IT (■) and SDT (●) simulations. Solid lines correspond to the analytical solution (III.48) at $M = 1.1, 1.2, 1.4$, and 1.5 (bottom to top) with $\alpha_s = 1.176$. Gray dashed line at $M_t/\Delta M = 0.6$ separates the wrinkled (W) and broken (B) regimes. Vanished regime lines at $R_\lambda \approx 5$ (V_5) and $R_\lambda \approx 65$ (V_{65}) also included as gray dashed lines. 72
- III.12 Theoretical solution of density jump from Eq. (III.33) in terms of M and M_t 73
- III.13 Polytropic exponents at (a) $x = 1$ and (b) $x = 2'$ from IT (squares) and SDT (circle) simulations at $M = 1.1$ (dark), 1.2 (medium) and 1.4 (light). Solid lines correspond to the isentropic value, 1.4 73

- IV.1 Rms-to-mean dilatation at the shock plotted as a function of (a) $M_t/(M^2 - 1)$ and (b) $M_t/\Delta M$. Dash-dotted lines is Eq. (IV.2) and solid lines is best fit with $e_1 = 0.502$ and $e_2 = 0.114$. Vertical gray dashed line at $M_t/\Delta M = 0.6$ for reference. Symbols are: Jamme *et al.* (2002)(\times), Larsson & Lele (2009)(∇) and Boukharfane *et al.* (2018)(\triangleleft). Reprinted from (Donzis, 2012b). 78
- IV.2 Rms-to-mean dilatation at the shock for $R_\lambda \approx 5$ (red stars), $R_\lambda \approx 10$ (green circles), $R_\lambda \approx 25$ (blue squares), $R_\lambda \approx 45$ (magenta diamonds), $R_\lambda \approx 65$ (cyan plusses). Open and closed symbols are for IT and SDT simulations, respectively. Dash-dotted lines is Eq. (IV.2) and solid lines is best fit with $e_1 = 0.577$ and $e_2 = 0.114$. Vertical gray dashed line at $M_t/\Delta M = 0.6$ for reference. Horizontal dashed lines: average of DNS data at high $M_t/\Delta M$ for $R_\lambda \approx 5, 10, 25, 45$ and 65 from bottom to top. Other symbols: Jamme *et al.* (2002)(\times), Larsson & Lele (2009)(∇) and Boukharfane *et al.* (2018)(\triangleleft). 80
- IV.3 Instantaneous dilatation normalized by laminar condition (θ_l) along streamwise direction at different transverse locations (grey) and their mean (black) at $M = 1.1$, $R_\lambda \approx 10$ and (a) $M_t = 0.05$ (wrinkled), (b) $M_t = 0.14$ (broken) and (c) $M_t = 0.34$ (vanished). 81
- IV.4 One instantaneous dilatation normalized by laminar condition (θ_l) at $M = 1.1$, $R_\lambda \approx 10$, $M_t = 0.34$. The dashed line is the location of the shock from $\min(\partial u/\partial x)$ 81
- IV.5 Distributions of R_{11} at $M = 1.1$, (a) $R_\lambda \approx 10$ and $M_t = 0.05$ (solid), $M_t = 0.14$ (dashed) and $M_t = 0.34$ (dash-dotted) and (b) $R_\lambda \approx 25$ and $M_t = 0.22$ (solid), $M_t = 0.3$ (dashed) and $M_t = 0.44$ (dash-dotted). Distribution of p at, (c) $R_\lambda \approx 10$ and $M_t = 0.05$ (solid), $M_t = 0.14$ (dashed) and $M_t = 0.34$ (dash-dotted), and (d) $R_\lambda \approx 25$ and $M_t = 0.14$ (solid), $M_t = 0.22$ (dashed) and $M_t = 0.44$ (dash-dotted). The vertical dashed lines are the shock location based on $\min(\partial \langle u \rangle / \partial x)$ 84
- IV.6 Asymptotic value of Θ as a function of R_λ . Different symbols represent the average of DNS data at a fixed R_λ in the asymptotic state (see text). Symbols as in figure IV.2. Solid line is Eq. (IV.4) with $c_1 = 1.756$ and $c_2 = 0.8217$ 87

IV.7	Rms-to-mean dilatation at the shock with (a) linear correlation between the supersonic and subsonic regions with $\alpha_\theta = (2.5, 0.6, 0.05, 0.01, 0)$ and $\beta_\theta = (0.01, 0.025, 0.5, 3, 4)$ and (b) dissipative anomaly for the subsonic regions with $\alpha_\theta = (5, 2, 0.05, 0)$ and $\beta_\theta = (0.01, 0.1, 1.5, 10000)$. Same colors and symbols as in figure IV.2.	89
IV.8	Normalized dissipation rate from Donzis <i>et al.</i> (2005) (solid) and present simulations at x_1 . Red circles correspond to $M = 1.1$, blue squares to $M = 1.2$ and green diamonds to $M = 1.4$. Open and closed symbols are for IT and SDT simulations, respectively.	91
V.1	A wave rider in hypersonic flight with $M = 6$. Visible Mach lines and boundary layers are shown. Courtesy of Prof. Bowersox.	95
V.2	Normalized distribution of (a) R_{11} , (b) R_{22} and (c) R_{11}/R_{22} with $M = 1.2$, $R_\lambda \approx 25$ and $M_t = 0.12$ (solid), 0.21 (dashed), 0.32 (dash-dotted) and 0.44 (dotted).	96
V.3	(a) Collection of amplification factors of streamwise velocity as a function of ΔM along with LIA prediction (Ribner, 1954b). (b) Same data as a function of $K = M_t/(R_\lambda^{1/2}\Delta M)$. Horizontal dashed lines: LIA prediction for $M = 1.1, 1.2, 1.3, 1.4, 1.5$ and 1.8 from bottom to top. In both figures red circles correspond to $M = 1.1$, blue squares to $M = 1.2$ and green diamonds to $M = 1.4$. Open and closed symbols are for IT and SDT simulations, respectively. Other symbols: Lee <i>et al.</i> (1993, 1997) (\triangleright), Hannappel & Friedrich (1995) (+), Barre <i>et al.</i> (1996) (\triangleleft), Mahesh <i>et al.</i> (1997) (\triangle), Jamme <i>et al.</i> (2002) (\times), Larsson & Lele (2009) and Larsson <i>et al.</i> (2013) (∇), Ryu & Livescu (2014) (*, grey levels for $M = 1.1, M = 1.2$ and $M = 1.4$ from light to dark), Boukharfane <i>et al.</i> (2018) (\blackstar) and Tanaka <i>et al.</i> (2018) (\star , grey levels for $M = 1.1, M = 1.3$ and $M = 1.5$ from light to dark). ..	100
V.4	Universality of amplification factor based on the scaling of (V.2) for data with $M < 2$. Same colors and symbols as in figure V.3.	103
V.5	Normalized distribution of (a) Ω_{11} , (b) Ω_{22} and (c) Ω_{22}/Ω_{11} with $M = 1.2$, $R_\lambda \approx 25$ and $M_t = 0.12$ (solid), 0.21 (dashed), 0.32 (dash-dotted) and 0.44 (dotted).	104

V.6	(a) Collection of amplification factors of transverse vorticity as a function of ΔM along with LIA prediction (Ribner, 1954 <i>b</i>). (b) Same data as a function of $K = M_t/(R_\lambda^{1/2}\Delta M)$. Horizontal dashed lines: LIA prediction for $M = 1.1, 1.2, 1.4, 1.8, 2.2$ and 3.5 from bottom to top. Same colors and symbols as in figure V.3.	106
V.7	Universality of amplification of transverse enstrophy based on the scaling of (V.4) for data with $M > 1.1$. Same colors and symbols as in figure V.3.	108
V.8	Normalized distributions η with $M = 1.2$, $R_\lambda \approx 25$ and $M_t = 0.12$ (solid), 0.21 (dashed), 0.32 (dash-dotted) and 0.44 (dotted).	110
V.9	Normalized distribution ϵ with $M = 1.2$, $R_\lambda \approx 25$ and $M_t = 0.12$ (solid), 0.21 (dashed), 0.32 (dash-dotted) and 0.44 (dotted).	110
V.10	Normalized distributions of J_{11} with $M = 1.2$, $R_\lambda \approx 25$ and $M_t = 0.12$ (solid), 0.21 (dashed), 0.32 (dash-dotted) and 0.44 (dotted).	112
V.11	Amplification factors of J_{11} with $M = 1.2$, $R_\lambda \approx 25$ and $M_t = 0.12$ (solid), 0.21 (dashed), 0.32 (dash-dotted) and 0.44 (dotted).	113
V.12	Distributions of J_{11} normalized by (a) laminar shock thickness and (b) mean free path with $M = 1.2$, $R_\lambda \approx 25$ and $M_t = 0.12$ (solid), 0.21 (dashed), 0.32 (dash-dotted) and 0.44 (dotted).	114
V.13	Location of maximum J_{11} downstream of the shock ($x_{2',J_{11}}$) relative to x_1 normalized by (a) laminar shock thickness and (b) mean free path with $M = 1.1$ (circles), $M = 1.2$ (squares) and $M = 1.4$ (diamonds). Dashed lines with slope for reference. Different tones of grays represent different values of R_λ	115
V.14	Normalized distributions of (a) $\langle \rho'^2 \rangle$, (b) $\langle p'^2 \rangle$ and (c) $\langle T'^2 \rangle$ with $M = 1.2$, $R_\lambda \approx 25$ and $M_t = 0.12$ (solid), 0.21 (dashed), 0.32 (dash-dotted) and 0.44 (dotted).	116
A.1	A normal shock wave travels from the left to the right at a speed w . The flow at the upstream is assumed incompressible while the downstream consists of solenoidal and dilatational motions.	132

LIST OF TABLES

TABLE	Page
II.1 DNS database of isotropic turbulence passing through a shock: number of grid points, mean Mach number (M), turbulent Mach (M_t) and Taylor Reynolds numbers (R_λ), normalized shock thickness and Kolmogorov length scale. The regime correspond to the criterion in (Donzis, 2012 <i>b</i>): $M_t/\Delta M$ less than and greater than 0.6 for the wrinkled and broken regimes respectively. Conditions for vanished regimes (marked with *) are computed at the upstream minimum for pressure as that for R_{11} disappears in this regime.	38
II.2 DNS database of anisotropic turbulence passing through a shock: number of grid points, mean Mach number (M), turbulent Mach (M_t) and Reynolds numbers (R_λ), normalized shock thickness and Kolmogorov length scale, shock regime Donzis (2012 <i>b</i>). Conditions for vanished regimes (marked with *) are computed at the upstream minimum for pressure as that for R_{11} disappears in this regime.	39
II.3 STI data from other simulations and experiments.....	39
III.1 Low order moments of m for a Gaussian distribution.	53

I. INTRODUCTION

I.A Turbulence and Shock Waves: An Overview

Turbulence is a natural phenomenon in fluid dynamics that exists in many natural and engineering systems. Its unpredictable and unrepeatable nature have made it one of the most challenging long-standing scientific problems. The seemingly stochastic motions observed in turbulent flows and its sensitivity to initial conditions, numerical methods and experimental facilities, make the problem extraordinary difficult. The governing laws given by the Navier-Stokes equations are a set of non-linear PDEs of such complexity that proofs of existence and uniqueness of solution currently stand as one of the well-recognized millennium problems. Another important characteristic of turbulence is the wide range of temporal and spatial scales. Such wide range of scales increases computational demands and experimental resources for capturing phenomena at both large and small scales. Though turbulent flows are chaotic with sensitivity to initial conditions and environmental disturbances, the statistical properties of a fully-developed turbulent flow tends to possess universal statistics features. This has been indeed a common trend in turbulence research through its history.

Generally, turbulence in compressible flows comprises solenoidal and dilatational motions. The former represents the rotational nature of turbulence and is associated with negligible density fluctuations. Additionally, for purely solenoidal flows, hydrodynamics is typically decoupled from thermodynamics in solenoidal components which provides a formidable simplification to the problem. In this cases, tur-

bulence is said to be incompressible and has been studied widely over the decades and a rich literature exist that document the advances in the field (Monin & Yaglom, 1975*a,b*; Pope, 2000). However, in many situations of practical interests the flow is compressible with considerable density fluctuations. These compressibility effects are accounted for in the dilatational component of fluctuations which result in additional complexity and a much more challenging set of phenomena to be understood.

A shock wave is a thin region of rapid compression where hydrodynamics and thermodynamics conditions change drastically. The formation of a shock wave occurs when a moving object exceeds the speed of sound and forces sound waves to collapse and propagate downstream. The compression exerted from the shock on the flow converts the mean kinetic energy to internal energy, resulting in lower velocity and higher temperature downstream of the shock. Though the region of variation is only a few mean free paths, properties of flows and thermodynamics are generally continuous across the shock. One of the challenges of studying shock waves comes from the very small shock thickness which requires substantial computational resources to fully resolve the region. Experimental efforts also face great challenges to capture the phenomena across the shock. The second challenge is shock stability as the stability of the location of the shock may depend on proper downstream conditions which may themselves be affected by turbulence. Slight change in post-shock conditions can result in shock unsteadiness. Another challenge is the validity of a continuum approach. A very strong shock wave in a fluid is known to present some deviations from the one described by the Navier-Stokes equations at high Mach numbers.

Here, we aim to study the interaction of isotropic turbulence and a normal

shock wave using a theoretical approach based on the quasi-equilibrium assumption (Donzis, 2012*b*) and direct numerical simulations (DNS) at a range of mean Mach number where a Navier-Stokes description of the relevant physical phenomena is still valid. Thus, we confine ourselves to relatively low Mach numbers.

I.B Background and Literature Review: Shock-turbulence Interactions

Shock-turbulence interactions are observed in a number of contexts including supersonic aerodynamics, turbulent combustion, and astrophysical flows among others, making it an important topic in fluid dynamics. The existence of a shock in a turbulent flow can significantly alter both the mean fields and turbulent characteristics in the vicinity and downstream of the shock (Andreopoulos *et al.*, 2000; Chen & Donzis, 2018). At the same time, turbulence can also change the structure of the shock. This two-way coupling makes well-known laminar theories predicting, for example, properties jumps across the shock inapplicable in the general case (Lele, 1992*a*; Lee *et al.*, 1993; Larsson & Lele, 2009; Velikovich *et al.*, 2012; Larsson *et al.*, 2013). The complexities associated with such flows have made investigations very challenging from the theoretical, experimental and numerical standpoints. To make progress, therefore, it seems necessary to devise flow configurations that reduce complexity yet maintain the essential physics and features of interest. Thus, the canonical interaction of isotropic turbulence with a normal shock without complexities due to boundary conditions, mean shear stresses, or externally imposed unsteady effects, have received substantial interest and a large body of literature is devoted to the topic (Sagaut & Cambon, 2008; Gatski & Bonnet, 2009).

Early theoretical studies (Ribner, 1954*a*; Moore, 1954; Ribner, 1954*b*) analyzed

the impingement of different disturbances on a normal shock where the shock is considered a discontinuity and the disturbances are small. The formulation further assumed an inviscid flow and that the incoming disturbance can be constructed as a linear combination of simple waves, typically assumed to follow the first-order decomposition of Kovasznay (1953) into vortical, entropy and acoustic modes. If the governing equations and jumps conditions across the shock are linearized, one can obtain a closed solution, now known as the linear interaction analysis (LIA). Decades later, Wouchuk *et al.* (2009) generalized the analytical solutions originally developed by Ribner and provided explicit expressions for different amplification factors across a shock. They also discussed additional limiting cases in terms of compressibility which were missing in Ribner’s pioneering work. Although LIA can indeed, under certain conditions, predict some of the trends associated of amplification of turbulence, evidence from experiments (Andreopoulos *et al.*, 2000) and simulations (Lee *et al.*, 1993; Mahesh *et al.*, 1995; Lee *et al.*, 1997; Larsson & Lele, 2009; Donzis, 2012a) have shown that other characteristics of the incoming turbulence not taken into account in the theory can strongly modify the outcome of the interaction. Since the shock is essentially a very strong longitudinal velocity gradient, it may seem that rapid distortion theory (RDT) can also provide complementary insight. This has indeed been done by Jacquin *et al.* (1993) and Kitamura *et al.* (2016) who also used Helmholtz’s decomposition to obtain amplification factors for turbulent kinetic energy. However, RDT was found to overestimate turbulence amplification, in part, due to the non-homogeneous compression induced by the shock (Jacquin *et al.*, 1993).

Because of the analytical intractability of the problem, direct numerical simulations (DNS) have become over the last few decades an invaluable and mature tool to

seek fundamental insight into STI. A number of DNS studies that investigated STI have also presented comparisons with different theories. Lee *et al.* (1993), without any technique of shock fitting or shock capturing, used DNS to investigate the interactions of vortical turbulence with a weak shock and found an increase in Reynolds stresses and enstrophy but a reduction of turbulent length scales. Pressure work was found to be the dominant mechanism in the rapid evolution of turbulent kinetic energy (TKE). Amplified fluctuations were also reported in thermodynamic properties in the vicinity of the shock due to the shock compression. As the flows pass through the shock, the evolution of thermodynamic fluctuations show a rapid decay mediated mainly by density-dilatation correlations. Further analysis showed that the polytropic exponent relating pressure and density fluctuations satisfies the isentropic relation even inside the shock. Subsequent numerical work relied on shock-capturing schemes to extend the range of Mach numbers and turbulent strength upstream of the shock (Lee *et al.*, 1997; Larsson & Lele, 2009). These numerical schemes, while able to capture the very steep gradients present in strong shocks, can also artificially dampen some turbulence scales close to those shocks (Johnsen *et al.*, 2010). Still, the conclusions from these investigations are consistent, at least qualitatively, with previous findings: amplification of Reynolds stresses and enstrophy and a decrease of turbulent length scales. A number of studies focused on the influence of the characteristics of the incoming turbulence based on Kovasznay decomposition (Hannappel & Friedrich, 1995; Mahesh *et al.*, 1997; Jamme *et al.*, 2002; Quadros *et al.*, 2016a) for which LIA provides specific predictions. Consistent results were obtained and showed that compared to pure vortical fluctuations the presence of entropy fluctuations upstream of the shock enhances the amplification of Reynolds stresses and transverse

enstrophy. On the other hand, the presence of these fluctuations further decreases transverse Taylor microscales and integral length scales. In contrast, the presence of acoustic fluctuations upstream of shock results in a reduction of the amplification of stresses and the reduction of transverse Taylor microscales. As amplification factors are different in the streamwise and transverse directions, Larsson *et al.* (2013) investigated the induced anisotropy behind shock waves. Unlike Reynolds stresses, enstrophy was found to return to isotropy over a long distance behind the shock. Using fully resolved simulations and LIA to generate high R_λ post-shock fields, Ryu & Livescu (2014) and Livescu & Ryu (2016) also investigated postshock anisotropy and showed that the postshock probability density function (PDF) of the deviatoric strain rate becomes more symmetric as the Mach number increases, indicating a decrease of vortex stretching and an increase in skewness of longitudinal velocity derivatives. Recently, Quadros *et al.* (2016*a,b*) studied the heat flux by looking at the correlation of velocity and internal energy fluctuation using both LIA and DNS. Their results suggest that the near-field correlation is dominated by pressure-energy and pressure-dilatation terms which come from the acoustic mode; the far field is governed by the other two modes. Besides the turbulence amplification found across the shock, Boukharfane *et al.* (2018) cast the attention to the turbulent mixing of a passive scalar in the presence of a normal shock. A significant enhancement of scalar mixing was reported downstream of the shock: the postshock p.d.f. of the scalar shows a much smaller standard deviation compared to the decaying turbulence. In contrast to the evolution of velocity fluctuations, attenuation is found in the scalar variance across the shock dominated by diffusive transport term.

As DNS data accumulated over the years, it became also clear that the result of

the interaction depends on characteristics of turbulence not accounted for in theoretical approaches such as LIA. In LIA, for example, the only parameter that determines the amplification of turbulence is the mean Mach number M . However, the collection of amplification factors of streamwise velocity ($G \equiv u_2'^2/u_1'^2$, where primes indicate root-mean-square quantities and 1 and 2 indicate locations upstream and downstream of the shock) in Donzis (2012*a*) shows, as mentioned above, systematic trends with Reynolds and turbulent Mach numbers in addition to M . These observations suggest that some of the assumptions behind LIA (linearity, no viscosity effects, shock wave as a discontinuity) are not satisfied, at least for the conditions presented in the literature. It was then proposed an alternative scaling parameter, K , that includes not only the mean Mach number but also the turbulent Mach number and the Reynolds number. This parameter $K \equiv M_t/R_\lambda^{1/2}(M - 1)$, which can be written as the ratio of laminar shock thickness to Kolmogorov length scale, was shown to provide a good collapse of the available data. While some new numerical studies have appeared since then (which are also compared against predictions below), the main focus has been on relatively strong shocks. Regimes where, instead, turbulence is relatively strong—and where assumptions behind classical theories may be inapplicable—have thus received relatively less attention, and is a thrust in the present work.

Experimental investigations, while very challenging, have also been pursued using different facilities and means of turbulence generation. The interaction of a normal shock with grid-generated turbulence inside a shock tube was measured by hot-wire anemometry (Honkan & Andreopoulos, 1992) and in wind tunnel (Inokuma *et al.*, 2017), while hot-wire and laser Doppler velocimetry were both used by Barre *et al.* (1996), and a new multi-hot-wire probe which is capable of measuring quantities re-

lated velocity gradient was developed (Agui *et al.*, 2005). Qualitatively, experimental results are consistent with simulations: turbulence was observed to be amplified with decreased length scales. However, also consistent with simulations, data suggest that the interaction depends on other characteristics not included in classical theoretical approaches such as the turbulence integral scale of the incoming turbulence (Agui *et al.*, 2005).

Of interest also is the effect of turbulence on the shock, especially when turbulence is relatively intense. The degree of variation in the peak compression inside a shock wave has been used as an indicator of the relative strength of the turbulence to the shock. When the turbulence is relatively weak, the dilatation along different streamlines across shock front shows similar compression peaks. When turbulence is strong, however, the shock characteristics become less homogeneous across the shock surface. At high enough turbulent intensities, it has been found that the shock may present “holes” on its surface along which variables do not undergo a steep gradient change consistent with classical one-dimensional inviscid theoretical results. Instead, variables can change smoothly or present multiple peaks. These two qualitatively distinct regimes have been termed wrinkled and broken (Lee *et al.*, 1993; Larsson & Lele, 2009) and have been traditionally determined from visual observations of flow fields.

To quantify the effects of turbulence on the shock, one can consider the rms-to-mean ratio of dilatation at the shock, Θ (described more precisely below). For a shock in a laminar uniform flow we have $\Theta = 0$, and as turbulence becomes stronger, Θ increases too. Thus Θ is a natural measure of how distorted the shock front is due to turbulence. Under the so-called quasi-equilibrium (QE) assumption (that

is, as explained more fully in subsequent sections, the assumption that the shock locally adjust instantaneously to local conditions generated by turbulent fluctuations) we have derived an expression for Θ which depends solely on the parameter $M_t/\Delta M$ (Donzis, 2012b) and that collapsed the data available then. Furthermore, we proposed a mechanism for the creation of holes as the response to subsonic regions resulting from strong turbulent fluctuations upstream of the shock. While the proposed criterion ($M_t/\Delta M \approx 0.6$) indeed identified correctly wrinkled and broken regimes (Donzis, 2012b), no data was available to test directly the appearance of subsonic regions. In this work we are able to both test this result as well as validate and extend the analytical expression obtained for Θ to the case of strong turbulence.

It has also been observed that turbulence fluctuations can affect the mean properties of the flow around the shock. The well-known Rankine-Hugoniot (RH) relations provide an exact solution to the governing equations for the change of properties across a one-dimensional steady laminar normal shock Thompson (1984). These expressions depend only on M . From theoretical considerations when turbulence is present, however, one can expect the results to depend also on turbulent characteristics, in particular the strength of the incoming fluctuations. Lele (1992b) considered shock jumps of density and pressure in the presence of upstream turbulence and suggested weakened jumps as turbulence intensity increases. In particular using an RDT closure he derived closed expressions for these jumps as a function of M and M_t . However, Larsson *et al.* (2013) suggested that while results were in qualitative agreement with DNS data, there were substantial quantitative disagreement and proposed an empirical dependence on M_t/M instead. In addition to its fundamental importance, understanding the effect of turbulence on mean fields has implications

for stability of shock waves in practical devices such as scramjets as well as in simulations of STI. It is indeed for the latter that this effect has been discussed most extensively mainly because imposing a laminar RH jump in pressure, leads to a moving instead of stationary shock wave (Larsson & Lele, 2009; Ryu & Livescu, 2014). Corrections to eliminate this so-called drift are typically found in an trial and error manner. Thus, there is a clear need to further our fundamental understanding of the effect of turbulence on mean fields, an effort that is undertaken here as well. Interestingly we found, for example, that in some circumstances jumps are weakened but in others are strengthened. It is also noteworthy that the widely used LIA approach assumes the mean flow to be known from laminar conditions and unaffected by fluctuations. Thus discrepancies between DNS and LIA may, in part, stem from this neglected effect on the mean hydrodynamic and thermodynamic properties of the flow downstream of the shock.

Besides thermodynamic variables, hydrodynamic properties across the shock have also been studied. An analytical expression for vorticity jump was provided by Truesdell (1952) by applying RH relations and assuming no viscosity and thermal conduction. The result showed that shock curvature is the only mechanism that contribute to vorticity even for an irrotational flow. Years later, other expressions were derived by Kevlahan (1997) that includes the baroclinic effects and shock compression which also imposed RH relations. In addition, Velikovich *et al.* (2012) studied the modified shock jump conditions with preshock density nonuniformity which is locally homogeneous and isotropic. The theory was based on small-amplitude limits and assumed no preshock velocity fluctuations. Unlike thermodynamic jumps, no comparison was provided to verify the accuracy of vorticity jump predictions given in the literature.

In what follows we present theory and a large DNS database to study jump relations for STI, statistics of the shock structure as well as regimes of the interaction, and amplification factors. The rest of the paper is organized as follows. In section 2, the details of the numerical methods used including grid convergence and domain size effects are introduced. In section 3, the quasi-equilibrium assumption is described and utilized to obtain thermodynamic jumps and rms-to-mean dilatation at the shock which are compared with DNS data. Amplification factors are discussed in section 4. Finally, conclusions are presented in section 5.

I.C Objective of Present Work

In this work we propose to:

1. Develop high-fidelity numerical methods to simulate stationary normal shock waves in turbulent flows.
2. Generate a very large database of a stationary normal shock interacting with anisotropic and isotropic turbulence under a wide range of shock and turbulent conditions.
3. Formulate theoretical relations of turbulent shock jumps and compare to available data in the literature.
4. Study the change of shock structure at different levels of turbulence intensity.
5. Analyze the shock compression effects on turbulence amplification at a wide range of turbulent conditions.

II. DIRECT NUMERICAL SIMULATIONS

DNS has been a very useful and powerful tool to study turbulence. It fully resolves the entire range of turbulence scales from integral length scales to Kolmogorov scales, leaving no modeling technique to modify the flows numerically. Even though this physical accuracy comes with a great cost of computation, such challenge has been gradually overcome by the increase of supercomputing resources. In the mean time, present simulations use shock-resolving scheme to capture the shock compression. Similar to DNS, this scheme also imposes no numerical assumption to resolve the scales in the flows. Therefore, This section discusses all the details in the present simulations, including how we generate the turbulence and stabilize the shock.

II.A Model Descriptions

II.A.1 Governing equations

The simulations presented here are based on the compressible Navier-Stokes equations written here as

$$\frac{\partial \rho}{\partial t} + \nabla \cdot (\rho \mathbf{u}) = 0, \quad (\text{II.1})$$

$$\frac{\partial}{\partial t}(\rho \mathbf{u}) + \nabla \cdot (\rho \mathbf{u} \mathbf{u}) = -\nabla p + \nabla \cdot \underline{\boldsymbol{\tau}} + \rho \mathbf{f} + \mathbf{S} \quad (\text{II.2})$$

$$\frac{\partial}{\partial t}(\rho e) + \nabla \cdot (\rho e \mathbf{u}) = -p \nabla \cdot \mathbf{u} + \nabla \cdot (\kappa \nabla T) + \underline{\boldsymbol{\tau}} \cdot \nabla \mathbf{u} + S_e \quad (\text{II.3})$$

where ρ is density, \mathbf{u} is the velocity vector, p is pressure, $\underline{\tau}$ is the stress tensor for a Newtonian fluid given by $\tau_{ij} = \mu(\partial u_i/\partial x_j + \partial u_j/\partial x_i - (2/3)\delta_{ij}\partial u_k/\partial x_k)$, \mathbf{f} is the body force vector that will be used below to generate turbulence, \mathbf{S} is a sponge vector, e is internal energy, κ is thermal conductivity and T is temperature. The viscosity follows a power law with temperature as $\mu = \mu_0(T/T_0)^{0.75}$ (μ_0 and T_0 are reference values) which has been found to be very close to Sutherland's formula (Chapman & Rubesin, 1949), and has been widely adopted in many STI studies (Larsson *et al.*, 2013; Ryu & Livescu, 2014; Huete *et al.*, 2017). The Prandtl number is assumed to be constant at $Pr = 0.72$. Finally, to close the system of equations, an ideal gas is assumed which follows the equation of state $p = \rho RT$ with R being the gas constant of the fluid.

II.A.2 Shock Stabilization and Boundary Conditions

In order to sustain a statistically stationary shock at a prescribed location in the domain it is necessary to impose a relatively high pressure downstream of the shock which is here done using a sponge region (S_1 in figure II.1). In a laminar shock, a pressure jump given by standard Rankine-Hugoniot relations would be sufficient to keep the shock at a given location. This is not the case when the flow is turbulent (Larsson & Lele, 2009). The interaction of turbulent fluctuations with the normal shock produces oscillations of the shock surface and a well-known slow drift of the shock (Lee *et al.*, 1993; Larsson *et al.*, 2013; Ryu & Livescu, 2014) which is due to the difference between the postshock pressure in a laminar and turbulent flow. Since the appropriate pressure jump that needs to be imposed to obtain a stationary shock does in fact depend on the actual solution of the problem, standard STI simulations

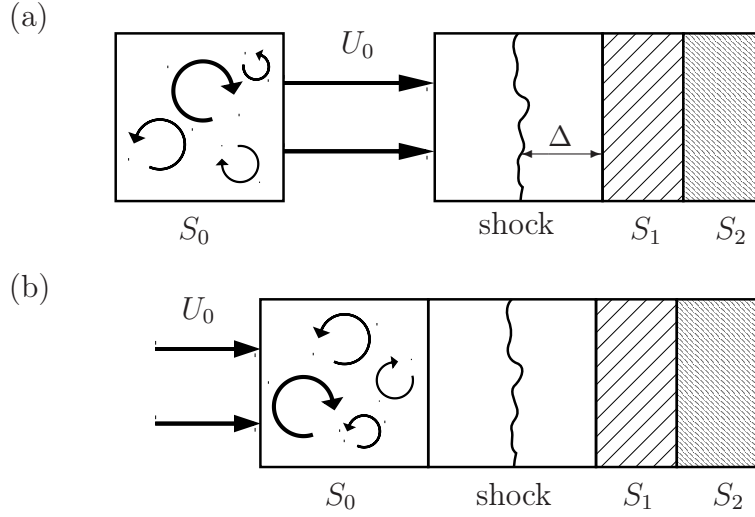


Figure II.1: A schematic of shock interacts with (a) isotropic turbulence and (b) anisotropic turbulence in the computational domains.

adjust the back pressure typically in a trial-and-error fashion to maintain the shock at a desired location. Our analytical results in the following §III, instead, provide the explicit dependence of pressure jumps on characteristics of the upstream turbulence. This is imposed, as previously mentioned, through S_1 .

In addition, care has to be taken to avoid boundary reflections as the flow becomes subsonic downstream of the normal shock. Thus, we use a second sponge (S_2 in figure II.1) between the first sponge (S_1) and the outlet. In this region the flow is smoothly accelerated to supersonic speeds. The main idea is that under such conditions no characteristic can travel upstream from the outlet avoiding, thus, potential effects from outflow boundary conditions. This approach has been used and tested in previous studies (Freund, 1997; Ryu & Livescu, 2014). In both sponge regions S_1

and S_2 we include a body force of the following form:

$$S_q = A \langle q \rangle \frac{(x - x_{s1})^{n_1} (x - x_{s2})^{n_2}}{l_s^{n_1+n_2+1}} (q_{ref} - q) \quad (\text{II.4})$$

where A is a constant, $\langle \cdot \rangle$ represents an average over the sponge region, x_{s1} and x_{s2} are the beginning and the end points of a sponge, l_s is the length of a sponge, n_1 and n_2 are constant exponents, and subscript *ref* stands for the specified value that a variable inside the sponge converge to. This particular form ensures that forces progressively become stronger and weaker as the flow enters and leaves the sponge, respectively. Clearly the strength of the sponge forcing vanishes at its boundaries, that is $S_q = 0$ at $x = x_{s1}$ and $x = x_{s2}$.

In S_1 we enforce a back pressure necessary to keep the shock at a statistically steady location. Since $p = (\gamma - 1)\rho e$, we use $q = \rho e$ in Eq. (II.4) for the energy equation Eq. (II.3) with $(\rho e)_{ref}$ computed such that it corresponds to the desired pressure. The specific value imposed was determined from the analytical expressions derived below which indeed resulted in stationary shocks, giving thus numerical support to the theoretical work presented here. In S_2 the flow is brought to supersonic speeds by accelerating the u_1 components. In this region, thus, we have $q = u_1$. The reference value for velocity is given by the inlet mean flow condition.

There is some freedom in choosing the sponge parameters, A , n_1 and n_2 . However, we found that some combinations were potentially unstable, in particular if S_q changes rapidly in space. On the other hand, if S_q is too weak, variables may not approach the reference value during their residence time in the sponge. From numerical experimentation we found that $(n_1, n_2) = (1, 1)$ in S_1 and $(2, 0)$ in S_2 provide

adequate results.

II.B Turbulence Generation

To study the generality of our theoretical results presented here, in addition to various Reynolds numbers and turbulent Mach numbers, we performed a series of DNS using a spectral forcing scheme but with two different procedures which results in statistically isotropic and anisotropic turbulence, respectively. Both methods, which will be discussed momentarily, produce turbulence with different characteristics which is convected downstream by a superimposed mean velocity U_0 at the domain inlet.

II.B.1 Forcing scheme

The forcing scheme for both approaches described below, is implemented by an additional body force in the momentum equation which is stochastic and applied at large scales. This force is constructed using integrated Ornstein-Uhlenbeck processes with finite-time correlation in Fourier space. In physical space, the forcing can be written as

$$\mathbf{f} = \sum_{|\mathbf{k}| < k_F} \hat{\mathbf{f}}_{\perp}(\mathbf{k}) e^{-i\mathbf{k} \cdot \mathbf{x}} \quad (\text{II.5})$$

where $\hat{\mathbf{f}}_{\perp}(\mathbf{k}) = (\mathbf{I} - \mathbf{k}\mathbf{k}/k^2) \cdot \hat{\mathbf{f}}$ is the projection of the mode at wave number \mathbf{k} onto a plane perpendicular to the wave vector itself. This guarantees that the stirring mechanism that generates turbulence is, by construction, solenoidal. The forcing parameters are chosen to achieve a given R_{λ} and M_t and, at the same time, yield integral length scales which are a fraction of the domain size. Additionally grid spacing should be fine enough to resolve accurately the small scales (discussed in

§II.E). Further details of the forcing and statistics of the resulting turbulence fields are described in Donzis & Jagannathan (2013) and Jagannathan & Donzis (2016).

II.B.2 Isotropic and anisotropic turbulence

Isotropic turbulence (IT). In this procedure a separate simulation of isotropic turbulence in a triply-periodic domain is conducted. Turbulence is sustained by a large scale stochastic forcing to achieve a given R_λ and M_t . Details of these simulations and the numerical procedure can be found in Donzis & Jagannathan (2013) and Jagannathan & Donzis (2016). Once in steady state, the turbulence is convected through the inlet using Taylor hypothesis at a velocity U_0 which corresponds to a mean Mach number, M . The schematic of this procedure is shown in figure II.1(a). A similar procedure has been used before in the literature (e.g. Ryu & Livescu, 2014) though forcing details are somewhat different. Some studies in the literature have used decaying simulations (e.g. Mahesh *et al.*, 1996; Larsson & Lele, 2009) though a potential challenge in this situation is the effects of initial conditions which may not disappear at the time turbulence is assumed to be fully developed. Longer times, on the other hand, would lead to a much weaker turbulence. The approach adopted here does not depend on initial conditions and the Reynolds and Mach numbers are determined by the forcing mechanism in the isotropic simulations.

Spatially developing turbulence (SDT). In this approach, turbulence is generated upstream of the shock as it is convected from the inlet at U_0 . A sketch is shown in figure II.1(b), where we also see that the domain is longer in the streamwise direction than that for the isotropic approach above. Such configuration provides similarities to grid-generated turbulence in wind tunnels where anisotropy in the turbulence

has been consistently observed (Grant & Nisbet, 1957; Mohamed & Larue, 1990) and may resemble more practical situations where turbulence develop spatially as it approaches the shock. The interaction between the fluctuations and the mean flow in the region S_0 , results in unequal production rates in the streamwise and transverse energies in axisymmetric flows (Taylor, 1935). The result is a slightly anisotropic flow with a streamwise component of the velocity variance being larger than transverse components.

II.C Numerical Algorithm

This investigation seeks to fully resolve the wide range of scales in both the shock wave and the turbulence using DNS without imposing any numerical technique. The required resolutions and storage for the studies become crucial with increasing shock strength and turbulence intensities. To capture the motions in time and space, high order schemes are implemented in the simulations, and their details are discussed here.

II.C.1 Temporal derivatives

Turbulence fluctuations evolve rapidly in time and space. The challenge of DNS is the number of grid points involved in spatial discretizations increases drastically with turbulence intensities. As a result, the corresponding memory management for temporal derivatives becomes critical.

The time advancement in the simulations is performed with an explicit third order low-storage Runge-Kutta scheme (Williamson, 1980). Consider a quantity, q ,

in a three-dimensional domain its governing equation can be written as:

$$\frac{\partial q}{\partial t} = f(q) \quad (\text{II.6})$$

where f contains all the other mechanisms besides the transient term in the equation.

Traditionally, the n -th order explicit Runge-Kutta scheme advances with a finite difference equation:

$$q^{(n+1)} = q^{(n)} + \sum_{j=1}^n w_j f_j. \quad (\text{II.7})$$

where n means the n -th time step and w_j is the coefficient of the j -th increment term in the scheme. Such method requires storage, $nN_xN_yN_z$, for each variable where N_x , N_y and N_z are the numbers of grid points in x , y and z direction, respectively. From the formula, we can see that more memory is required with the increasing order. To alleviate such requirement, a different principle adopted in the simulations is to leave the useful information on the register which will receive the contribution $f(x_j)$ instead of starting with a new empty register. Such algorithm is expressed as:

$$q_j = a_j q_j + \Delta t f(x_{j-1}) \quad (\text{II.8a})$$

$$x_j = x_{j-1} + b_j q_j \quad \text{where } j = 1 \cdots n. \quad (\text{II.8b})$$

Successive values of q_j and x_j overwrite the previous ones so that at each increment only $2N_xN_yN_z$ storage is required. A third order scheme implemented in present simulations results in $(a_1, a_2, a_3) = (0, -5/9, 153/128)$ and $(b_1, b_2, b_3) = (1/3, 15/16, 8/15)$.

Compared to traditional Runge-Kutta scheme in a three-dimensional problem,

the storage requirement in this high order scheme for each variable is a constant, $2N_xN_yN_z$. With the increase of temporal derivative order, the simulations can better capture the evolution in time without requesting more memory.

The value of each time step, Δt , is decided by the dominant term between convection and diffusion in Eq. (II.2) with a CFL condition to avoid instability. The formula for deciding Δt is

$$\Delta t = \min \left(\frac{1}{\frac{(u_1+c)_{\max}}{\Delta x} + \frac{(u_2+c)_{\max}}{\Delta y} + \frac{(u_3+c)_{\max}}{\Delta z}}, \frac{\min(\Delta x^2, \Delta y^2, \Delta z^2)}{\max(\nu, \frac{\kappa}{\rho C_p})} \right) \text{CFL} \quad (\text{II.9})$$

where $()_{\max}$ represents the largest value among in the domain, c is speed of sound, Δx , Δy and Δz are the size of grid points in three different directions, ν is kinematic viscosity and C_p is specific heat capacity. With variables change temporally, Δt will be updated correspondingly at each time step.

II.C.2 Spatial derivatives

Typically, the accuracy of a finite difference increases with the length of stencils. However, it is also known that explicit finite differences have difficulties in achieving high orders while remaining stable (Chertock & Abarbanel, 2000). Furthermore, the spectral methods are typically limited to simple domains and simple boundary conditions (Lele, 1992a). As a result, compact schemes were proposed to achieve high accuracy while still maintaining short stencils. The implementation and use of compact schemes for isotropic compressible turbulent simulations have been described in details in Jagannathan & Donzis (2016). For periodic boundary condition in the transverse directions, such sixth order method is also applied in present simulations. However, due to the non-periodic boundary condition in streamwise direction and the

further requirements needed to resolve the shock, we show here a new tenth order implementation and produce grid-independent results in shock-resolving configurations in the following section in II.E.

In the direction of mean flow where non-periodic boundary condition is applied, the formulation of first derivative for interior nodes is given as

$$\beta f'_{i-2} + \alpha f'_{i-1} + f'_i + \alpha f'_{i+1} + \beta f'_{i+2} = a \frac{f_{i+1} - f_{i-1}}{2\Delta x} + b \frac{f_{i+2} - f_{i-2}}{4\Delta x} + c \frac{f_{i+3} - f_{i-3}}{6\Delta x} \quad (\text{II.10})$$

where f'_i represents the finite difference approximation of first derivative at grid point i and α , β , a , b and c are the coefficients derived by matching the Taylor series coefficients of various orders. Expand the terms at the right hand side, we can obtain

$$\begin{aligned} & \sum_0^{\infty} \frac{\delta_{n0} \Delta x^n}{n!} + 2\alpha \sum_{0,2,\dots}^{\infty} \frac{\Delta x^n}{n!} f_i^{(n+1)} + 2\beta \sum_{0,2,\dots}^{\infty} \frac{2^n \Delta x^n}{n!} f_i^{(n+1)} \\ &= \sum_{0,2,\dots}^{\infty} \frac{a + 2^n b + 3^n c}{(n+1)!} \Delta x^n f_i^{(n+1)} \end{aligned} \quad (\text{II.11})$$

which can be simplified to

$$\sum_0^{\infty} \frac{(n+1)(\delta_{n0} + 2\alpha + 2\beta 2^n)}{(n+1)!} f_i^{(n+1)} = \sum_{0,2,\dots}^{\infty} \frac{a + 2^n b + 3^n c}{(n+1)!} \Delta x^n f_i^{(n+1)}. \quad (\text{II.12})$$

The formal order of truncation error is decided by the first unmatched coefficient leading to the constraints

$$\text{second order (n=0): } 1 + 2\alpha + 2\beta = a + b + c$$

$$\text{fourth order (n=2): } 3(2\alpha + 2^3\beta) = a + 2^2b + 3^2c$$

$$\text{sixth order (n=4): } 5(2\alpha + 2^5\beta) = a + 2^4b + 3^4c$$

eighth order (n=6): $7(2\alpha + 2^7\beta) = a + 2^6b + 3^6c$

tenth order (n=8): $9(2\alpha + 2^9\beta) = a + 2^8b + 3^8c$.

The linear system of coefficient can be either be tridiagonal where $\beta = 0$ or pentadiagonal where $\beta \neq 0$. Inside the domain of present studies, pentadiagonal scheme is applied and the tenth order scheme leads to: $\alpha = 1/2$, $\beta = 1/20$, $a = 17/12$, $b = 101/150$ and $c = 1/100$.

For the points on the boundary, the first derivative can be obtained from a forward formulation

$$f'_1 + \alpha_1 f'_2 = \frac{1}{\Delta x} (a_1 f_1 + b_1 f_2 + c_1 f_3 + d_1 f_4) \quad (\text{II.13})$$

where the subscript 1 is at the boundary while subscript 2, 3 and 4 are its neighboring points. Again, by replacing Taylor series for all terms in Eq. (II.13) the equation is expressed as

$$\begin{aligned} \sum_0^{\infty} \frac{\delta_{n0} \Delta x^n}{n!} f_1^{(n+1)} + \alpha_1 \sum_0^{\infty} \frac{\Delta x^n}{n!} f_1^{(n+1)} = & \left[a_1 \sum_{-1}^{\infty} \frac{\delta_{n0} \Delta x^{n-1}}{(n+1)!} f_1^{(n+1)} + b_1 \sum_{-1}^{\infty} \frac{\Delta x^{n-1}}{(n+1)!} f_1^{(n+1)} \right. \\ & + c_1 \sum_{-1}^{\infty} \frac{2^n \Delta x^{n-1}}{(n+1)!} f_1^{(n+1)} \\ & \left. + d_1 \sum_{-1}^{\infty} \frac{3^n \Delta x^{n-1}}{(n+1)!} f_1^{(n+1)} \right]. \end{aligned} \quad (\text{II.14})$$

Further simplification leads to

$$\begin{aligned} \sum_0^{\infty} \left[\frac{\delta_{n0}}{n!} + \frac{\alpha}{n!} - \frac{\delta_{n-1} a_1}{(n+1)!} - \frac{b_1}{(n+1)!} - \frac{2^{n+1} c_1}{(n+1)!} - \frac{3^{n+1} d_1}{(n+1)!} \right] \Delta x^n f_1^{(n+1)} \\ = (a_1 + b_1 + c_1 + d_1) \frac{f_1^{(0)}}{\Delta x}. \end{aligned} \quad (\text{II.15})$$

If the node is at the outlet, a backward formulation is adopted which result in identical equation. Similar to the central formulation, the first unmatched coefficient

determines the order of truncation error and fourth order scheme is applied to the boundary in present simulations

$$\text{second order: } \begin{cases} (\text{n}=-1): a_1 + b_1 + c_1 + d_1 = 0 \\ (\text{n}=0): b_1 + 2c_1 + 3d_1 = 1 + \alpha_1 \\ (\text{n}=1): \frac{1}{2}(b_1 + 4c_1 + 9d_1) = \alpha_1 \end{cases}$$

$$\text{third order (n=2): } \frac{1}{6}(b_1 + 8c_1 + 27d_1) = \frac{\alpha_1}{2}$$

$$\text{fourth order (n=3): } \frac{1}{24}(b_1 + 16c_1 + 81d_1) = \frac{\alpha_1}{6}.$$

By solving the linear equations above, the coefficients of fourth order scheme for the points on the boundaries are $\alpha_1 = 3$, $\beta_1 = 0$, $a_1 = -17/6$, $b_2 = 3/2$, $c_2 = 3/2$ and $d_2 = -1/6$.

The schemes near the boundary nodes are chosen with great care by increasing the truncation order slowly toward tenth order (Poinsot & Lele, 1992). In particular, we use an one-sided fourth order scheme at the boundary, biased central fourth and sixth order schemes at the next two grid points, followed by an eighth order central scheme before applying a tenth order scheme at the rest of all interior points.

An approach to construct approximations that satisfy global conservation constraint should also be considered while choosing the values of coefficients for first derivatives. Consider a conservation law with a form

$$\frac{\partial f}{\partial t} + \frac{\partial F}{\partial x} = 0, \tag{II.16}$$

over a domain $[a, b]$ and $F = F(f)$ with certain initial and boundary conditions.

Upon integration over the entire domain yields

$$\frac{d}{dt} \int_a^b f(x, t) dx = F|_{x=a, t} - F|_{x=b, t}, \quad (\text{II.17})$$

which indicates that the change of total f inside the domain only comes from the flux of f across the boundary. This is a global conservation statement which poses an additional constraint to the coefficients of first derivatives. Consider the system of the linear equations from each grid points with different coefficients be written as

$$\underline{\mathbf{A}} f' = \underline{\mathbf{B}} \frac{df}{dx} \quad (\text{II.18})$$

where $\underline{\mathbf{A}}$ and $\underline{\mathbf{B}}$ are given in a N^2 sparse matrix and N is the number of grid point in streamwise direction. $\underline{\mathbf{B}}$ is therefore given as Eq. (II.19). Each row in the equation shows the coefficients of corresponding equations and the given weighting functions w_1 , w_2 , w_3 and w_4 for global conservation. In order to satisfy the global conservation constraint, it is required that the summation of each column from 2 to $N-1$ of the matrix to be exactly zero. This constraint promises only the boundary nodes have contribution to the fluxes. Node 4 is specifically chosen to be imposed on the conservation restriction, meaning the coefficients for node 4 become dependent

on neighboring coefficients.

$$\underline{\mathbf{B}} = \begin{bmatrix} w_1 a_1 & w_1 b_1 & w_1 c_1 & w_1 d_1 & & & & & \\ -w_2 a_2/2 & 0 & w_2 a_2/2 & 0 & & & & & \\ -w_3 b_3/4 & -w_3 a_3/2 & 0 & w_3 a_3/2 & w_3 b_3/4 & & & & \\ -w_4 c_4/6 & -w_4 b_4/4 & -w_4 a_4/2 & 0 & w_4 a_4/2 & w_4 b_4/4 & w_4 c_4/6 & & \\ & -c/6 & -b/4 & -a/2 & 0 & a/2 & b/4 & c/6 & \\ & & -c/6 & -b/4 & -a/2 & 0 & a/2 & b/4 & c/6 \\ & & & \ddots & \ddots & \ddots & \ddots & \ddots & \\ & & & & & & & & \end{bmatrix} \quad (\text{II.19})$$

By imposing the global conservation condition, it is shown that:

$$\frac{3b + 2c}{3b_4} = \frac{c}{c_4} \quad (\text{II.20})$$

where b_4 and c_4 are coefficients to be determined by b and c which are the coefficients from the tenth order interior scheme. The global conservation constraint finally leads to $\alpha_4 = 633/1268$.

The summary of the coefficients for first derivatives at different grid points along the streamwise direction are presented as follows. For the first five points from the boundaries:

$$f'_1 + \alpha_1 f'_2 = \frac{1}{\Delta x} (a_1 f_1 + b_1 f_2 + c_1 f_3 + d_1 f_4) \quad (\text{II.21})$$

where the coefficients are given by

$$\alpha_1 = 3, a_1 = -\frac{17}{6}, b_1 = \frac{3}{2}, c_1 = \frac{3}{2} \text{ and } d_1 = -\frac{1}{6}.$$

$$\alpha_2 f'_1 + f'_2 + \alpha_2 f'_3 = a_2 \frac{f_3 - f_1}{2\Delta x} \quad (\text{II.22})$$

where the coefficients are related by

$$\alpha_2 = \frac{1}{4} \text{ and } a_2 = \frac{2(\alpha_2 + 2)}{3}.$$

$$\beta_3 f'_1 + \alpha_3 f'_2 + f'_3 + \alpha_3 f'_4 + \beta_3 f'_5 = a_3 \frac{f_4 - f_2}{2\Delta x} \quad (\text{II.23})$$

where α_3 , β_3 and a_3 are given by

$$\alpha_3 = \frac{17}{57}, \beta_3 = \frac{3\alpha_3 - 1}{12} \text{ and } a_3 = \frac{-6\alpha_3 + 16}{9}.$$

$$\beta_4 f'_2 + \alpha_4 f'_3 + f'_4 + \alpha_4 f'_5 + \beta_4 f'_6 = a_4 \frac{f_5 - f_3}{2\Delta x} + b_4 \frac{f_6 - f_2}{4\Delta x} + c_4 \frac{f_7 - f_1}{6\Delta x} \quad (\text{II.24})$$

where α_4 , β_4 , a_4 , b_4 and c_4 are given by

$$\alpha_4 = \frac{633}{1268}, \beta_4 = \frac{8\alpha_4 - 3}{20}, a_4 = \frac{-7\alpha_4 + 12}{6}, b_4 = \frac{568\alpha_4 - 183}{150} \text{ and } c_4 = \frac{9\alpha_4 - 4}{50}.$$

$$\beta f'_{i-2} + \alpha f'_{i-1} + f'_i + \alpha f'_{i+1} + \beta f'_{i+2} = a \frac{f_{i+1} - f_{i-1}}{2\Delta x} + b \frac{f_{i+2} - f_{i-2}}{4\Delta x} + c \frac{f_{i+3} - f_{i-3}}{6\Delta x} \quad (\text{II.25})$$

where α , β , a , b and c are given by

$$\alpha = \frac{1}{2}, \beta = \frac{1}{20}, a = \frac{17}{12}, b = \frac{101}{150} \text{ and } c = \frac{1}{100}.$$

The derivation of second derivatives is analogous to the first derivatives'. The formulation of the second derivative for the interior nodes is presented as

$$\begin{aligned} & \beta f''_{i-2} + \alpha f''_{i-1} + f''_i + \alpha f''_{i+1} + \beta f''_{i+2} \\ &= a \frac{f_{i+1} - 2f_i + f_{i-1}}{\Delta x^2} + b \frac{f_{i+2} - 2f_i + f_{i-2}}{4\Delta x^2} + c \frac{f_{i+3} - 2f_i + f_{i-3}}{9\Delta x^2} \end{aligned} \quad (\text{II.26})$$

where f_i'' represents the finite difference approximation of second derivative at grid point i . Similar to the first derivative, the form being tridiagonal or pentadiagonal depends on the choice of β and present studies also choose pentadiagonal for second derivatives. The relation given above can be expressed in terms of Taylor series expansion:

$$\begin{aligned}
& 2\beta \sum_{0,2,\dots}^{\infty} \frac{2^n \Delta x^n}{n!} f_i^{(n+2)} + 2\alpha \sum_{0,2,\dots}^{\infty} \frac{\Delta x^n}{n!} f_i^{(n+2)} + \sum_{0,2,\dots}^{\infty} \frac{\delta_{n0} \Delta x^n}{n!} f_i^{(n+2)} \\
& = (-2a - \frac{2}{4}b - \frac{2}{9}c) \sum_0^{\infty} \frac{\delta_{0n} \Delta x^{n-2}}{n!} f_i^{(n)} + a \sum_{0,2,\dots}^{\infty} \frac{2 \Delta x^n}{n!} f_i^{(n)} \\
& + \frac{b}{4} \sum_{0,2,\dots}^{\infty} \frac{2 \cdot 2^n \Delta x^{n-2}}{n!} f_i^{(n)} + \frac{c}{9} \sum_{0,2,\dots}^{\infty} \frac{2 \cdot 3^n \Delta x^{n-2}}{n!} f_i^{(n)}.
\end{aligned} \tag{II.27}$$

Again, the first unmatched coefficient determines the order of truncation order,

$$\text{second order (n=0): } a + b + c = 1 + 2\alpha + 2\beta$$

$$\text{fourth order (n=2): } a + 2^2 b + 3^2 c = \frac{4!}{2!} (\alpha + 2^2 \beta)$$

$$\text{sixth order (n=4): } a + 2^4 b + 3^4 c = \frac{6!}{4!} (\alpha + 2^4 \beta)$$

$$\text{eighth order (n=6): } a + 2^6 b + 3^6 c = \frac{8!}{6!} (\alpha + 2^6 \beta)$$

$$\text{tenth order (n=8): } a + 2^8 b + 3^8 c = \frac{10!}{8!} (\alpha + 2^8 \beta).$$

For the points on the boundary, the general form of second derivative approximation is given as

$$f_1'' + \alpha_1 f_2'' = \frac{1}{\Delta x^2} (a_1 f_1 + b_1 f_2 + c_1 f_3 + d_1 f_4 + e_1 f_5) \tag{II.28}$$

Replacing Taylor expansion for all the terms yields

$$\begin{aligned}
\sum_0^{\infty} \frac{\delta_{n0} \Delta x^n}{n!} f_1^{(n+2)} + \alpha_1 \sum_0^{\infty} \frac{\Delta x^n}{n!} f_1^{(n+2)} &= a \sum_{-2}^{\infty} \frac{\delta_{n(-2)} \Delta x^n}{(n+2)!} f_1^{(n+2)} + b \sum_{-2}^{\infty} \frac{\Delta x^n}{(n+2)!} f_1^{(n+2)} \\
&+ c \sum_{-2}^{\infty} \frac{2^n \Delta x^n}{(n+2)!} f_1^{(n+2)} + d \sum_{-2}^{\infty} \frac{3^n \Delta x^n}{(n+2)!} f_1^{(n+2)} \\
&+ e \sum_{-2}^{\infty} \frac{4^n \Delta x^n}{(n+2)!} f_1^{(n+2)}.
\end{aligned} \tag{II.29}$$

The truncation orders given by the first unmatched coefficients are

$$\text{second order} \left\{ \begin{array}{l} (n=-2): a + b + c + d + e = 0 \\ (n=-1): b + 2c + 3d + 4e = 0 \\ (n=0): b + 4c + 9d + 16e = 2(1 + \alpha_1) \\ (n=1): b + 8c + 27d + 64e = 9\alpha_1 \end{array} \right.$$

$$\text{third order (n=2): } b + 16c + 81d + 256e = 16\alpha_1$$

$$\text{fourth order (n=3): } b + 32c + 243d + 1024e + 20\alpha + 160\beta.$$

Similar to the first derivatives, the truncation orders of second derivatives increase slowly from the boundary to the interior points. An one-sided fourth order is implemented at the boundary. Biased central fourth order, sixth order and eighth order are implemented at the following three grid points. For the rest of grid points in the interior, a tenth order scheme is applied.

The summary of coefficients in second derivatives at the first five grid points from the boundaries are presented as follows

$$f_1'' + \alpha_1 f_2'' = \frac{1}{\Delta x^2} (a_1 f_1 + b_1 f_2 + c_1 f_3 + d_1 f_4 + e_1 f_5) \tag{II.30}$$

where the coefficients are given by

$$\begin{aligned}\alpha_1 &= 10, \quad a_1 = \frac{11\alpha_1 + 35}{12}, \quad b_1 = \frac{-5\alpha_1 - 26}{3}, \\ c_1 &= \frac{\alpha_1 + 19}{2}, \quad d_1 = \frac{\alpha_1 - 14}{3} \quad \text{and} \quad e_1 = \frac{-\alpha_1 + 11}{12}. \\ \alpha_2 f_1'' + f_2'' + \alpha_2 f_3'' &= a_2 \frac{f_3 - 2f_2 + f_1}{\Delta x^2}\end{aligned}\tag{II.31}$$

where the coefficients are related by

$$\begin{aligned}\alpha_2 &= \frac{1}{10} \quad \text{and} \quad a_2 = \frac{4(-\alpha_2 + 1)}{3}. \\ \beta_3 f_1'' + \alpha_3 f_2'' + f_3'' + \alpha_3 f_4'' + \beta_3 f_5'' &= a_3 \frac{f_4 - 2f_3 + f_2}{\Delta x^2} + b_3 \frac{f_5 - 2f_3 - f_1}{4\Delta x^2}\end{aligned}\tag{II.32}$$

where α_3 , β_3 and a_3 are given by

$$\begin{aligned}\alpha_3 &= \frac{12}{97}, \quad \beta_3 = -\frac{1}{194} \quad \text{and} \quad a_3 = \frac{-9\alpha_3 - 12\beta_3 + 6}{4}. \\ \beta_4 f_2'' + \alpha_4 f_3'' + f_4'' + \alpha_4 f_5'' + \beta_4 f_6'' &= a_4 \frac{f_5 - 2f_4 + f_3}{\Delta x^2} + b_4 \frac{f_6 - 2f_4 - f_2}{4\Delta x^2}\end{aligned}\tag{II.33}$$

where α_4 , β_4 , a_4 , b_4 and c_4 are given by

$$\begin{aligned}\alpha_4 &= \frac{344}{1179}, \quad \beta_4 = -\frac{38\alpha_4 - 9}{214}, \quad a_4 = \frac{-1191\alpha_4 + 696}{428} \quad \text{and} \quad b_4 = \frac{2454\alpha_4 - 294}{535}. \\ \beta f_{i-2}'' + \alpha f_{i-1}'' + f_i'' + \alpha f_{i+1}'' + \beta f_{i+2}'' &= a \frac{f_{i+1} - 2f_i + f_{i-1}}{\Delta x^2} + b \frac{f_{i+2} - 2f_i - f_{i-2}}{4\Delta x^2} \\ &\quad + c \frac{f_{i+3} - 2f_i - f_{i-3}}{9\Delta x^2}\end{aligned}\tag{II.34}$$

where

$$\alpha = \frac{334}{899}, \beta = \frac{43}{1798}, a = \frac{1065}{1798}, b = \frac{1038}{899} \text{ and } c = \frac{79}{1798}.$$

The implemented schemes have been thoroughly verified. For example, in figure II.2, we compare the grid convergence tests using sixth and tenth order scheme on the interior points. For the sixth order scheme, the truncation orders change from the boundaries to the interior are third order, fourth order, fourth order and sixth order. The comparison of the two schemes focuses on two of the main quantities used in this work that is amplification factor, G , and rms-to-mean dilatation, Θ , at the shock. While the first one is a low order quantity, the latter presents much more challenges and has been used as the most stringent constraint in assessing our numerics. Figure II.2 shows the evolutions of G and Θ with resolutions. In the figure we can see how tenth order schemes approach grid convergence at lower resolution than sixth order schemes for Θ , as expected. The comparison indicates the advantage of higher order scheme over convergence against lower resolution. A more detailed grid independence test will be discussed in the following section §II.E where quantities are normalized by proper characteristic scales.

II.D Averages and Characteristic Locations

Turbulent flows present fluctuations at a wide range of scales and it is thus convenient to decompose the flows into a mean and fluctuations. This is typically done using Reynolds decomposition, that is $f = \langle f \rangle + f'$ where $\langle f \rangle$ is a suitably defined mean and f' is the fluctuating part; clearly $\langle f' \rangle = 0$. In compressible flows, it is often more convenient to use the density-weighted or Favre average (e.g. Gatski & Bonnet, 2009) defined as $\tilde{f} = \langle \rho f \rangle / \langle \rho \rangle$ which leads to significant simplifications in

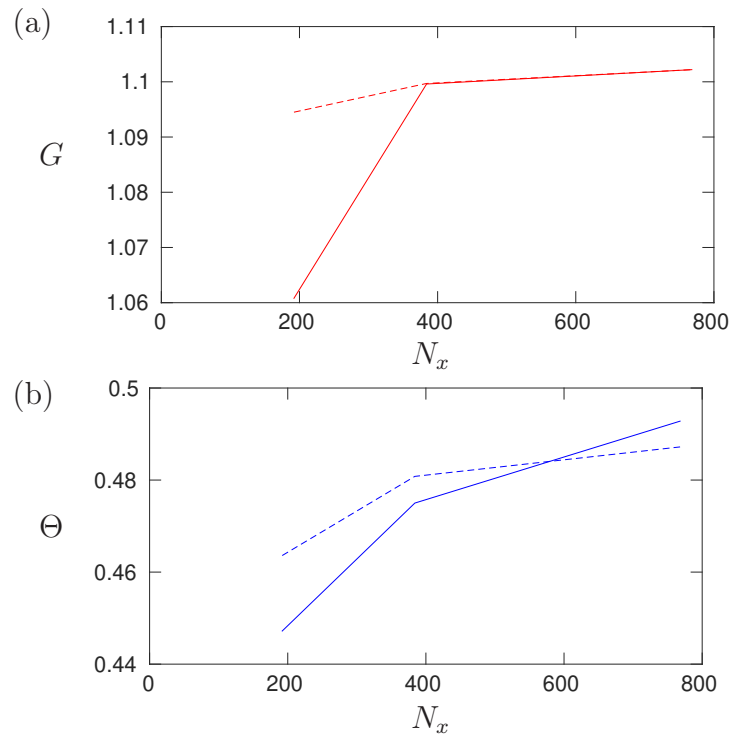


Figure II.2: Grid independence tests with sixth order scheme (solid) and tenth order scheme (dashed) for (a) amplification factors, and (b) rms-to-mean ratio of dilatation.

the governing equations. The fluctuations around the Favre averages are denoted by f'' such that $f = \tilde{f} + f''$ and $\langle \rho f'' \rangle = 0$.

The specific space over which averaging is done depends naturally on the flow of interest. In particular, averages are meaningfully taken over dimensions of homogeneity. For example, experimental measurements of statistically stationary flows commonly average quantities over long periods of time. In isotropic simulations, averages are conducted over the entire volume since the flow is homogeneous in the three spatial directions. In STI, since the streamwise direction, x , is not homogeneous, averages can be taken over the other two homogeneous directions, that is over y - z planes. Furthermore, since the flows presented here are also statistically stationary, one can improve statistical convergence by averaging over time as well. Indeed, unless otherwise noted, angular brackets represent plane and time averages in what follows.

Figure II.3(a) shows a typical distribution of the streamwise Reynolds stress as a function of x/L , the streamwise direction normalized by the dissipation length scale at x_1 where x_1 is defined later in this section. We make a few remarks here to identify specific characteristic locations in the flow and leave more detailed physical discussions relegated to later sections. Turbulence enters the domain from the left, and it undergoes a viscous decay which reduces turbulent stresses. As turbulence reaches the vicinity of the shock, these Reynolds stresses as well as other thermodynamic properties, such as p (figure II.3(b)), begin to increase due to transfers of energy between modes. The local minimum thus formed, has been defined in the literature as the upstream location of the shock and will be denoted here by a subscript 1. Assessing amplification or reduction across the shock can be then performed by

normalizing a quantity of interest by its value at this upstream condition denoted by a subscript 1. Obviously, for any quantity $q(x)$ we have $q(x_1)/q_1 = 1$. Figure II.3(a) shows a typical variation of $R_{11}/R_{11,1} = \widetilde{u_1'' u_1''}/\widetilde{u_1'' u_1''}|_1$ in the streamwise direction.

The non-dimensional parameters that characterize the flow are naturally defined at x_1 . These are the mean Mach number of the incoming flow ($M \equiv \langle u_1 \rangle / \langle c \rangle$) which for a stationary shock is also the so-called shock Mach number, the Taylor Reynolds number ($R_\lambda \equiv \langle \rho \rangle u_{1,rms} \lambda / \langle \mu \rangle$), and the turbulent Mach number ($M_t \equiv |\widetilde{\mathbf{u}_1''}|^{1/2} / \langle c \rangle$).

Inside the shock region, stresses reach a peak at a location where the pressure gradient is largest. Reynolds stresses then decrease and reach a downstream minimum where pressure attain a maximum. This location, identified as 2', indicates the end of the region dominated by shock compression. An expansion wave would follow behind the shock (Larsson & Lele, 2009) where the stress reaches its downstream maximum. This process is dominated by pressure-dilatation exchanges that transfers internal energy to turbulent kinetic energy (Lee *et al.*, 1993). Such transfer results in a local minimum of pressure and other thermodynamic variables which is considered in following sections. The Reynolds stresses increase but eventually viscous dissipation dominates the energy exchanges and turbulence undergoes again a classical viscous decay. The local maximum of $R_{11}/R_{11,1}$ downstream of the shock is denoted here by a subscript 2. We have also verified that the locations of the minimum and maximum for density and temperature do coincide with those of the pressure. Thus, the discussion here focuses on the comparison of Reynolds stresses and pressure.

Though R_{11} and thermodynamic quantities share similar characteristic locations that mark regions dominated by different mechanisms, other turbulent quantities

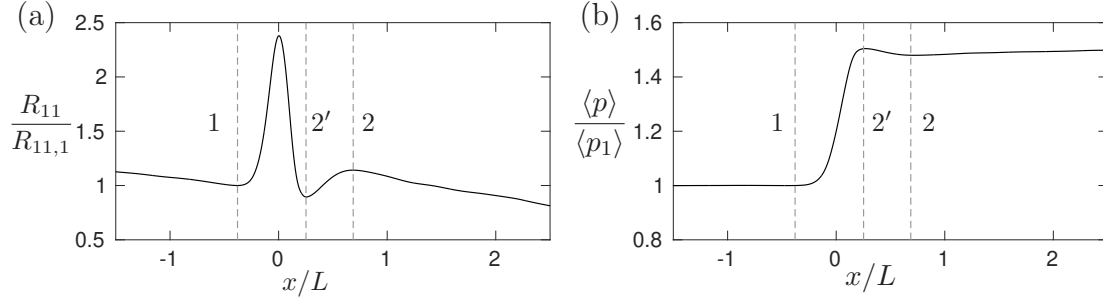


Figure II.3: Typical streamwise distribution of (a) Reynolds stress R_{11} and (b) pressure both normalized by their upstream value at $M = 1.2$, $R_\lambda \approx 25$, and $M_t = 0.21$. Vertical dashed lines at x_1 , $x_{2'}$ and x_2 for reference.

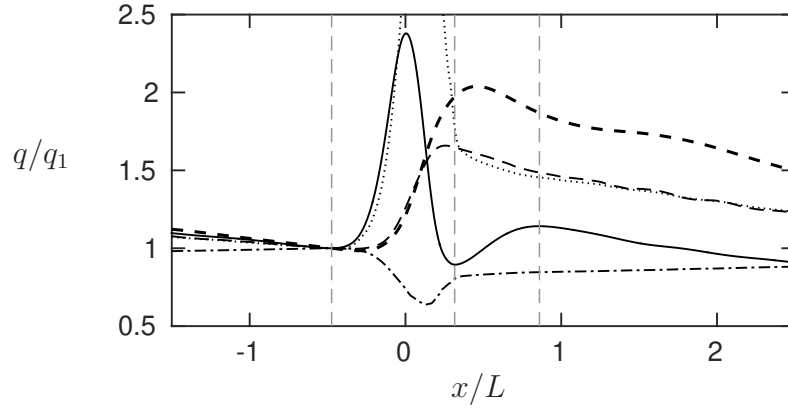


Figure II.4: Normalized distributions of Reynolds stress R_{11} (solid), transverse enstrophy Ω_{22} (dashed), mass flux variance J_{11} (thick dashed), dissipation ϵ (dotted) and Kolmogorov length scale η (dash-dotted) at $M = 1.2$, $R_\lambda \approx 25$ and $M_t = 0.21$. Same vertical dashed lines as in figure II.3.

show very distinct distributions. Beside R'_{11} s, the distributions of transverse enstrophy, $\Omega_{22} = \langle \omega_2 \omega_2 \rangle$, variance of mass flux, $J_{11} = \langle (\rho u_1)^2 \rangle$, viscous dissipation, ϵ , and Kolmogorov length scale, η , are shown in figure II.4. It is clearly shown that viscous decays dominates in the areas away from shock vicinity. The figure also shows that the x_1 of Ω_{22} and J_{11} are located slightly downstream of $x_{1_{R11}}$ while $x_{2'_{\Omega_{22}}}$ and $x_{2'_{J11}}$ are close to $x_{2'_{R11}}$ but still with quantitative difference. On the other hand, good agreements on x_1 and $x_{2'}$ are shown between dissipation, Kolmogorov length scale and R_{11} . One main difference between R_{11} and other quantities is that only R_{11} has a postshock peak at $x_{2'}$. Other quantities all show a monotonic decay after $x_{2'}$. To further understand the distribution in each quantity it requires deeper discussion with corresponding budget which is beyond present investigation.

As seen in figure II.3, the local minimum in Reynolds stresses downstream of the shock ($x_{2'_{R11}}$) coincides with the maximum in pressure ($x_{2'_p}$). However, this has not been systematically assessed. We do precisely that in figure II.5(a&b) where we plot the distance between x_1 to the minimum of the Reynolds stresses downstream of the shock ($x_{2'_{R11}} - x_1$) versus the distance between x_1 and the maximum of the mean pressure downstream of the shock ($x_{2'_p} - x_1$) both normalized by Kolmogorov scales (other normalizations are possible and lead to the same conclusions). If these locations coincide, the data would lie on a straight line with slope of 1 (dashed line in figure II.5). In general we see that for IT simulations the differences between $x_{2'_{R11}}$ and $x_{2'_p}$, if any at all, are very small. Some SDT simulations (stars in the figure), however, are above the line implying that $x_{2'_{R11}}$ is slightly closer to the shock than $x_{2'_p}$, which may point to a subtle but complex dynamic mechanism related to anisotropic Reynolds stresses. While a thorough understanding of this issue is

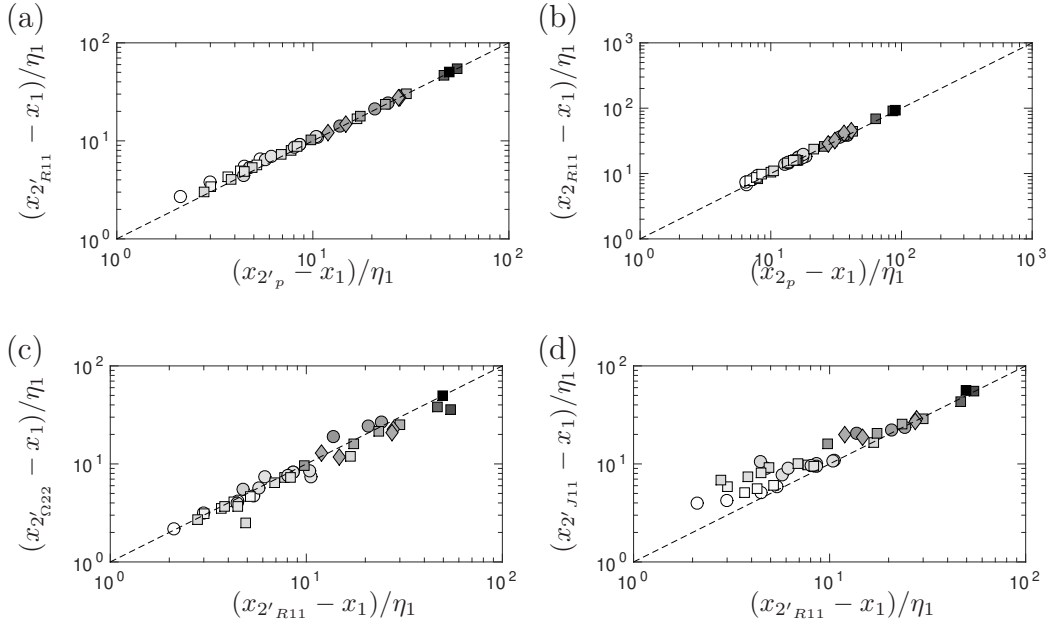


Figure II.5: Location of minimum in Reynolds stresses and maximum of pressure both downstream of the shock (x'_{R11} and x'_{Rp} , respectively) relative to x_1 with $M = 1.1$ (circles), $M = 1.2$ (squares) and $M = 1.4$ (diamonds). Dashed lines with slope for reference. Different tones of grays represent different values of R_λ from 5 (lightest) to 65 (darkest).

relegated for future work, we note here that the effect is small. Similar plots are given in figure II.5(c&d) for Ω_{22} and J_{11} . Though with some scatter, the $x_{2'}$ of Ω_{22} is located consistently close to x'_{R11} . Contrary to Ω_{22} , J_{11} shows a more complicated trend. At $(x'_{R11} - x_1)/\eta_1 \lesssim 10$, x'_{J11} is located further downstream than x'_{R11} . Such trend changes when $(x'_{R11} - x_1)/\eta_1 \gtrsim 10$, and x'_{J11} becomes fairly close to x'_{R11} . Again, studies of different quantities evolving through space require analyses on budgets and is relegated for future work. In any case, to be precise in our calculations and avoid ambiguity, pressure jumps are computed at x'_{Rp} while Reynolds stresses are computed at x'_{R11} . With this understanding we will use, for simplicity in notation, $x_{2'}$ and x_2 for in what follows, respectively.

II.E Resolution and DNS Database

We have generated a large DNS database of STI simulations. In table II.1 we summarize the parameters for the simulations of STI with IT. The incoming turbulence is at turbulent Mach numbers M_t ranging from 0.05 to 0.54 and Reynolds numbers up to 65. These parameters are obtained at location x_1 . The table also includes the ratio of Kolmogorov length scale to grid size $\eta/\Delta x$, and the laminar shock thickness to grid size, $\delta_l/\Delta x$, where (Thompson, 1984) $\delta_l = 2k_1\mu_1/(c_1\rho_1\Delta M)$ with $k_1 = (4/3 + \mu_v/\mu_1 + (\gamma - 1)/\text{Pr})$, and μ_v is the coefficient of bulk viscosity. In our simulations $k_1 \sim O(1)$. We have also included the classification of the regime of the interaction based on Donzis (2012*b*) where we proposed a specific mechanism for hole creation and a semi-analytical prediction of the boundary between regimes. In particular we proposed a transition from wrinkled to broken at $M_t/\Delta M \approx 0.6$ which is consistent with the regime observed at different conditions from DNS in the literature (Larsson *et al.*, 2013; Ryu & Livescu, 2014). In addition, a new regime is also proposed to address unprecedented phenomena with details given in §IV.B.

To ensure grid independence, convergence tests were conducted to study the sensitivity of variables that characterize both effects on the shock and the turbulence to grid resolution. To do so, it is important to assess the effect of resolution on both large and, more critically, small scales. Two quantities that satisfy these requirements and we analyze in detail below are the streamwise Reynolds stress, specifically its amplification factor, and the maximum dilatation at the shock. Contributions to these variables come primarily from large and small scales, respectively. The latter is thus critically sensitive to resolution as it is computed at a location where

grid	M	R_λ	M_t	$\delta_l/\Delta x$	$\langle\delta_t\rangle/\Delta x$	$\eta/\Delta x$	regime
1024x256 ²	1.1	12	0.05	4.89	11.0	8.58	wrinkled
512x128 ²	1.1	10	0.08	4.84	9.40	4.86	broken
512x128 ²	1.1	10	0.14	8.42	17.1	4.96	broken
256x128 ²	1.1	11	0.22	6.90	13.9	2.55	broken
256x128 ²	1.1	11	0.29	10.1	16.3	2.65	broken
256x128 ²	1.1	11	0.34	11.5	17.2	2.82	vanished*
1024x256 ²	1.1	27	0.13	4.85	23.8	4.65	broken
512x128 ²	1.1	24	0.22	4.57	25.8	2.56	broken
512x128 ²	1.1	25	0.30	6.99	29.5	2.68	broken
512x128 ²	1.1	24	0.44	12.83	50.0	3.05	vanished*
2048x512 ²	1.2	12	0.05	4.86	15.6	17.7	wrinkled
1024x256 ²	1.2	11	0.08	4.85	14.5	9.80	wrinkled
512x128 ²	1.2	10	0.14	4.53	12.3	4.94	broken
512x128 ²	1.2	12	0.22	7.42	19.6	5.05	broken
256x128 ²	1.2	13	0.39	5.82	16.6	2.48	broken
2048x512 ²	1.2	27	0.12	4.85	34.4	9.42	broken
1024x256 ²	1.2	24	0.21	4.82	36.4	5.14	broken
1024x256 ²	1.2	23	0.32	7.24	43.2	5.23	broken
512x256 ²	1.2	25	0.44	5.34	49.9	2.82	broken
2048x512 ²	1.2	47	0.34	4.69	84.5	4.61	broken
1536x512 ²	1.2	42	0.42	5.36	84.9	4.10	broken
4096x512 ²	1.2	62	0.28	4.86	129	6.48	broken
2048x512 ²	1.2	65	0.51	5.05	109	3.64	broken
2048x512 ²	1.4	23	0.23	4.82	45.6	9.51	wrinkled
1536x512 ²	1.4	25	0.33	5.45	48.8	7.78	broken
1024x256 ²	1.4	23	0.45	5.58	61.2	5.47	broken
1024x256 ²	1.4	24	0.54	6.32	61.8	5.35	broken

Table II.1: DNS database of isotropic turbulence passing through a shock: number of grid points, mean Mach number (M), turbulent Mach (M_t) and Taylor Reynolds numbers (R_λ), normalized shock thickness and Kolmogorov length scale. The regime correspond to the criterion in (Donzis, 2012b): $M_t/\Delta M$ less than and greater than 0.6 for the wrinkled and broken regimes respectively. Conditions for vanished regimes (marked with *) are computed at the upstream minimum for pressure as that for R_{11} disappears in this regime.

grid	M	R_λ	M_t	R_{11}/R_{22}	$\delta_l/\Delta x$	$\langle\delta_t\rangle/\Delta x$	$\eta/\Delta x$	regime
384x128 ²	1.07	5	0.15	1.24	25.9	25.11	5.86	vanished*
768x128 ²	1.1	4	0.02	1.26	8.55	9.15	13.6	wrinkled
384x128 ²	1.1	5	0.04	1.25	6.98	7.65	6.33	wrinkled
384x128 ²	1.1	5	0.07	1.33	11.7	12.2	6.47	broken
384x128 ²	1.1	5	0.12	1.57	15.8	17.1	6.14	broken
768x128 ²	1.1	13	0.06	1.11	4.88	9.96	5.23	wrinkled
512x128 ²	1.1	12	0.09	1.29	5.77	10.4	4.36	broken
384x128 ²	1.1	13	0.13	1.47	5.94	10.6	3.27	broken
384x128 ²	1.1	10	0.16	1.10	7.30	13.7	3.25	broken
768x128 ²	1.2	7	0.07	1.40	6.95	10.04	9.92	wrinkled
384x128 ²	1.2	5	0.09	1.37	7.37	9.25	6.49	wrinkled
384x128 ²	1.2	5	0.12	1.48	8.20	10.9	6.06	broken
384x128 ²	1.2	5	0.16	1.64	9.37	13.2	5.75	broken
1536x256 ²	1.2	13	0.05	1.44	4.75	11.0	12.9	wrinkled
896x128 ²	1.2	12	0.08	1.23	4.86	10.6	8.34	wrinkled
512x128 ²	1.2	13	0.16	1.48	4.98	12.6	4.38	broken

Table II.2: DNS database of anisotropic turbulence passing through a shock: number of grid points, mean Mach number (M), turbulent Mach (M_t) and Reynolds numbers (R_λ), normalized shock thickness and Kolmogorov length scale, shock regime Donzis (2012*b*). Conditions for vanished regimes (marked with *) are computed at the upstream minimum for pressure as that for R_{11} disappears in this regime.

Sources	M	R_λ	M_t	Method
Lee <i>et al.</i> (1993)	1.05-1.20	12-20	0.0567-0.11	Shock-resolving
Hannappel & Friedrich (1995)	2.0	6.67	0.17	Shock-capturing
Barre <i>et al.</i> (1996)	3.0	15	0.011	Experiment
Lee <i>et al.</i> (1997)	1.5-3.0	15.7-19.7	0.09-0.11	Shock-capturing
Mahesh <i>et al.</i> (1997)	1.3	19.1	0.14	Shock-capturing
Jamme <i>et al.</i> (2002)	1.2-1.5	5-6	0.173	Shock-resolving
Larsson & Lele (2009)	1.3-6.0	40	0.16-0.38	Shock-capturing
Larsson <i>et al.</i> (2013)	1.5	73	0.22	Shock-capturing
Ryu & Livescu (2014)	1.1-2.2	10-45	0.02-0.27	Shock-resolving
Tanaka <i>et al.</i> (2018)	1.1-1.5	18	2.96E-4	Shock-capturing
Boukharfane <i>et al.</i> (2018)	1.7-2.3	21	0.17	Shock-capturing

Table II.3: STI data from other simulations and experiments.

gradients are largest (inside the viscous shock). In fact, this is a very strict resolution criterion but necessary for well-resolved shock-resolving simulations. In figure II.6, we show the typical behavior of the amplification factor of streamwise velocity, $G = R_{11,2}/R_{11,1}$ and $\Theta \equiv (\langle \theta_s^2 \rangle_s / \langle \theta_s \rangle_s^2 - 1)^{1/2}$ where θ_s is the instantaneous dilatation $\partial u_i / \partial x_i$ when its magnitude is largest (that is inside the shock) as the ratio of shock thickness to grid spacing is increased. The conditions are $M = 1.2$, $M_t = 0.21$ and $R_\lambda \approx 25$. We see that beyond $\delta_l / \Delta x \approx 4.5$, changes in these quantities are within 2% and are thus considered grid converged. Similar results have been observed for the other conditions in our database. At the same time, resolution should be fine enough to resolve turbulence. We have found (Jagannathan & Donzis, 2016) that a resolution of $\eta / \Delta x \approx 0.5$ is sufficient in isotropic turbulence to capture even fourth order moments of velocity gradients at the conditions presented here. From tables II.1 and II.2 we can see that resolving the shock wave provides a stricter resolution criterion. Thus simulations with $\delta_l / \Delta x \gtrsim 4.5$ are considered well resolved. In the table we also include $\langle \delta_t \rangle$, the average thickness of the shock when turbulence is present (Donzis, 2012b) which is here computed as $(\langle u_2 \rangle - \langle u_1 \rangle) / (\partial \langle u \rangle / \partial x)_{max}$. As expected and consistent with theoretical predictions (Donzis, 2012b), the difference between δ_l and $\langle \delta_t \rangle$ increases with M_t . We do note that these definitions are estimates based on the maximum gradient at the shock and upon inspection represent only a fraction of the actual spatial extent occupied by the shock. In fact, even for the most stringent condition, at least 20 grid points are located between x_1 and x_2 (see figure II.3). This is generally consistent with Ryu & Livescu (2014) who found that 12 grid points across the shock resulted in grid-converged results. As mentioned above, however, this is for the most stringent cases and, as seen in the tables, most simulations have a larger

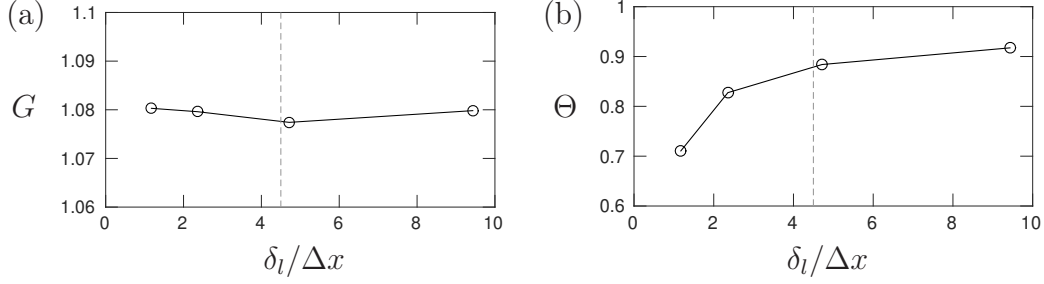


Figure II.6: Grid-independence test with different $\delta_l/\Delta x$ at $M = 1.1$, $M_t = 0.21$ and $R_\lambda \approx 25$ for (a) amplification factor and (b) rms-to-mean dilatation. The dashed line represents $\delta_l/\Delta x = 4.5$.

number of grid points in the shock region.

Upstream of the shock, the flow is supersonic. The hyperbolic nature of the governing equations in this condition results in characteristics that can only propagate downstream. On the other hand, the flow behind the shock is subsonic and characteristics can propagate both upstream and downstream. Thus, non-physical features of the flow downstream of the shock can affect the interaction. To ensure the sponges downstream of the shock have negligible effect on the interaction, we have conducted simulations with varying distance between the shock and the sponges, Δ (see figure II.1). The results are seen in figure II.7 where we show the distribution of $R_{11}/R_{11,1}$ at $M = 1.1$, $M_t = 0.22$ and $R_\lambda \approx 10$ with different values of Δ . Shock drifting effect is observed at $\Delta = 0.5\pi$ for which the location of the shock differs to others. While the differences in this plot seem small, one would like to evaluate the effect on the actual quantities of interest here. Thus, similar to the tests assessing small-scale resolution described above, we assessed the effect of Δ on amplification factors and dilatation at the shock. The results are seen in figure II.8 where we present G and Θ for different values of Δ . We can see that differences in this quan-

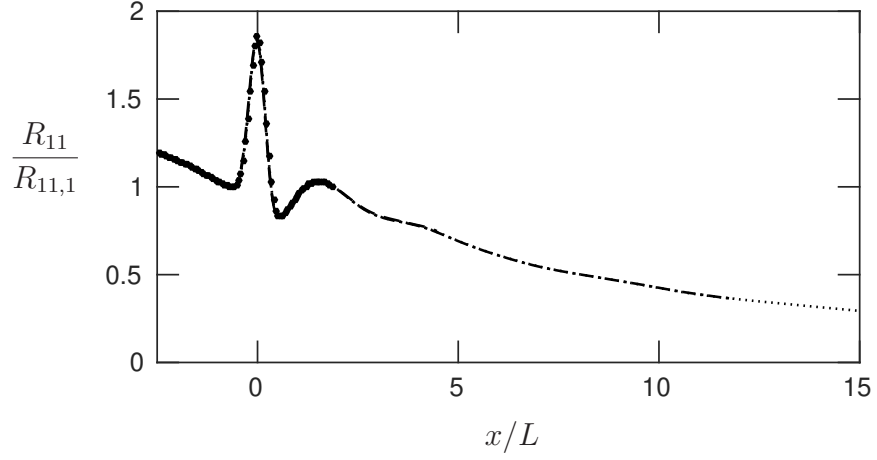


Figure II.7: Distribution of R_{11} at $M = 1.2$, $M_t = 0.23$ and $R_\lambda \approx 10$ with $\Delta = 0.5\pi$ (\bullet), 1.1π (dashed), 2.2π (dash-dotted) and 3.3π (dotted)

tities for $\Delta \gtrsim \pi$ are negligibly small. While data with $\Delta = 0.5\pi$ is also close, as a conservative measure especially at high M_t , we have used $\Delta = \pi$ in all our simulations. For reference, we mention that this distance corresponds to $\Delta \approx 2.2L$ where L is the integral scale of the incoming turbulence.

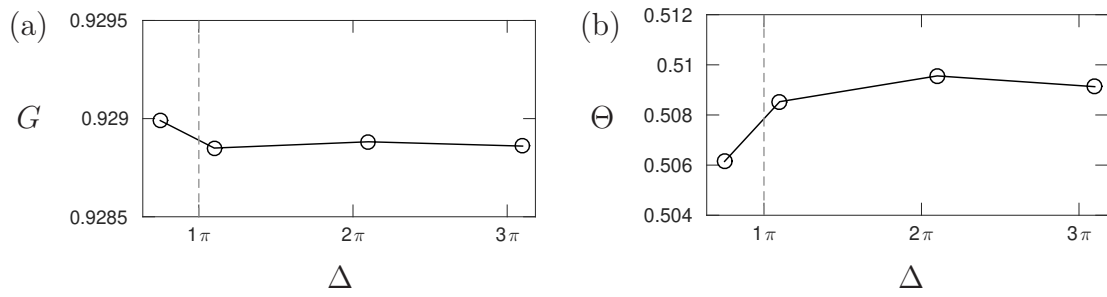


Figure II.8: Test of distance between shock and sponges for (a) G and (b) Θ at $M = 1.2$, $M_t = 0.23$ and $R_\lambda \approx 10$.

III. TURBULENT SHOCK JUMPS OF THERMODYNAMIC VARIABLES

III.A Theoretical Background: Quasi-equilibrium Assumption and Truncated Integrals

Available results in the literature clearly show that characteristics of STI depend critically on, for example, the strength of turbulence (Andreopoulos *et al.*, 2000) which is not captured by LIA. An alternative view has been more recently put forward (Donzis, 2012*b*), in which it was assumed, that the shock, locally, adjusts instantaneously to local flow conditions. This was referred to as the quasi-equilibrium assumption. If conditions are such that QE is satisfied, the shock surface can be treated as a collection of infinitesimal laminar shocks at different conditions. For QE to be valid, the time scale associated with the relaxation of the shock to a new incoming condition should be much shorter than changes in upstream conditions produced by the turbulence. The estimation and comparison of these two time scales is presented next.

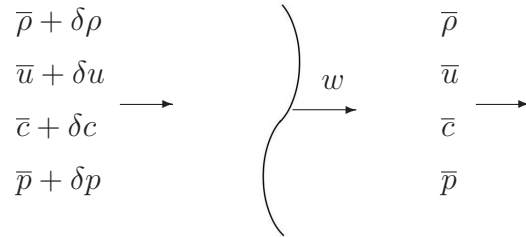


Figure III.1: Perturbations in a flow with a moving wave

Consider a flow field without any perturbation in the beginning as shown at the right hand side of figure III.1. From the left, perturbations travel at a speed w to the right, the conservation of mass at the downstream yields

$$\bar{\rho}\delta u + \delta\rho(\bar{u} - w) = 0. \quad (\text{III.1})$$

According to momentum conservation, we can obtain the pressure perturbation as

$$\delta p = -\rho(\bar{u} - w)\delta u. \quad (\text{III.2})$$

Substituting Eq. (III.1) into Eq. (III.2) to eliminate δu , the speed of the traveling wave is obtained as

$$w = \bar{u} \pm c \quad (\text{III.3})$$

where $c = \sqrt{\delta p / \delta \rho}$. This equation shows that the wave travels at the speed of sound relative to the flow. The plus-minus sign depends on the direction of the wave. If the wave is right-running, the speed would be $u + c$, and the speed would be $u - c$ for left-running waves.

If the flow is isentropic, thermodynamic quantities are related as $p \sim \rho^\gamma \sim T^{\gamma/(\gamma-1)}$. With the speed of sound $c = \sqrt{\gamma RT}$, we can then write

$$\frac{dp}{p} = \gamma \frac{d\rho}{\rho} = \frac{\gamma}{\gamma-1} \frac{dT}{T} = \frac{2\gamma}{\gamma-1} \frac{dc}{c}. \quad (\text{III.4})$$

Using Eq. (III.2) and Eq. (III.4), we can obtain the change of speed of sound with

respect to flow velocity,

$$\frac{\delta c}{\delta u} = \pm \frac{\gamma - 1}{2}. \quad (\text{III.5})$$

Let us consider the velocity slope, $\partial u / \partial x$, to be a measure of wave form and how such quantity changes at a given point of the wave. To obtain the evolution of this velocity derivative, we turn to the Euler equation

$$\frac{\partial u}{\partial t} = -u \frac{\partial u}{\partial x} - \frac{1}{\rho} \frac{\partial p}{\partial x}. \quad (\text{III.6})$$

which, with Eq. (III.4) and Eq. (III.5), can be written as

$$\frac{\partial u}{\partial t} = -(u \pm c) \frac{\partial u}{\partial x}. \quad (\text{III.7})$$

By taking the spatial derivative of Eq. (III.7), the time derivative of velocity gradient is written as

$$\frac{\partial u_x}{\partial t} = \pm \frac{\gamma + 1}{2} u_x^2 - (u \pm c) u_{xx}. \quad (\text{III.8})$$

where for simplicity in notation, subscript represent derivatives (e.g. $u_x = \partial u / \partial x$).

Since u_x depends on both time and space, we can write

$$\frac{du_x}{dt} = \frac{\partial u_x}{\partial t} + \frac{dx}{dt} \frac{\partial u_x}{\partial x} \quad (\text{III.9})$$

where $dx/dt = u \pm c$ is the traveling speed of the wave. Finally, by substituting Eq. (III.8) into Eq. (III.9), we can obtain the velocity derivative in a wave as

$$\frac{du_x}{dt} = \pm \frac{\gamma + 1}{2} u_x^2. \quad (\text{III.10})$$

Now consider a one-dimensional shock wave with a Mach number, M . If the Mach number of the shock wave changes from M at t_1 to $M + m$ at $t_2 = t_1 + \Delta t_s$, we can easily obtain

$$\Delta t_s = \frac{2}{\gamma + 1} [u_x(t_2)^{-1} - u_x(t_1)^{-1}] \quad (\text{III.11})$$

from Eq. (III.10). In general, the maximum negative gradient of velocity is considered the center of the shock. According to Taylor's weak shock theory, the velocity gradient, u_x of the shock at t_1 can be expressed as

$$u_x(t_1) = -\frac{\rho c^2}{2(\gamma + 1)\mu k_1} \left(M - \frac{1}{M}\right)^2, \quad (\text{III.12})$$

Using the same method, we can also obtain the velocity gradient at t_2 as well. Applying Eq. (III.11) at t_1 and t_2 and then substituting into Eq. (III.12) yields

$$\Delta t_s = \frac{4D}{c^2} \left[\left(M - \frac{1}{M}\right)^2 - \left(M + m - \frac{1}{M + m}\right)^2 \right]. \quad (\text{III.13})$$

Eq. (III.13) represents the time for a shock to change from M to $M + m$. With the equation expanded as a Taylor series in m and only the dominant terms included, the time scale can be written as

$$\Delta t_s \approx \frac{4\mu k_1}{\rho c^2} g_1(M) m \quad (\text{III.14})$$

where $g_1(M) = M(M^2 + 1)/(M^2 - 1)^3$. By definition, Mach number fluctuation can be correlated with longitudinal structure function by $m = \sqrt{D_u^L(r)}/c$ where D_u^L refers to a second order longitudinal velocity structure function. In isotropic turbulence,

classical theory shows that the second order structure function are

$$D_u^L(r) = r^2 \left\langle \left(\frac{\partial u_1}{\partial x_1} \right)^2 \right\rangle = \frac{r^2 \epsilon}{15\nu}. \quad (\text{III.15})$$

Finally, the required time for a shock to change from one state to another one would be

$$\Delta t_s \approx \frac{4\mu k_1}{\rho c^3} g_1(M) \sqrt{\frac{r^2 \epsilon}{15\nu}}. \quad (\text{III.16})$$

As the shock condition changes from M to $M + m$, the fluids would move a distance from x to $x + r$ correspondingly. Then the time for turbulent flows to move a distance r would be

$$\Delta t_t = \frac{r}{U} \quad (\text{III.17})$$

where Δt_t represents the time for turbulence to change correspondingly with the shock and U is the mean flow velocity.

As QE dictates that $\Delta t_s \ll \Delta t_t$, we proceed to compare these two quantities. Using the well-known relation $\epsilon = \nu u^2 / 15\lambda^2$, the ratio of the two time scales from the shock and turbulence defined in Donzis (2012*b*) would become

$$\begin{aligned} K_t &\equiv \frac{\Delta t_s}{\Delta t_t} \\ &= \frac{4\mu k_1}{\rho c^3} g_1(M) \sqrt{\frac{r^2 \epsilon}{15\nu}} \frac{U}{r} \\ &= \frac{4k_1}{15} \frac{\mu u}{\rho c^2 \lambda} g_2(M) \end{aligned} \quad (\text{III.18})$$

where $g_2 = g_1(M)M$ and $O(4k_1/15) \sim 1$. A good approximation for g_2 is $1/\Delta M^2$

(Donzis, 2012*a*). Using this result in Eq. (III.18), we can finally get

$$K_t \approx K^2 \tag{III.19}$$

where K was previously discussed in §I.B and it represents the ratio of laminar shock thickness to Kolmogorov length scale. QE is only valid when $K_t \ll 1$. This condition is satisfied by most STI database in the literature, including present studies.

We have showed that QE is justified when $K \ll 1$ which is satisfied for virtually all cases available in the literature. The main analytical advantage of QE is that it provides a framework in which well-known laminar results can be used to analytically compute mean variables in STI. For example, in Donzis (2012*b*) we derived statistics of the dilatation at the shock (Θ) which compared very well with available numerical data in the literature. Furthermore, the analysis yielded a dependence on a new non-dimensional parameter ($M_t/\Delta M$) which was found to provide a much better collapse of the data than what had been proposed before ($M_t^2/(M^2 - 1)$).

In this section we use QE to provide analytical results for thermodynamic jumps across a turbulent shock and generalize previous results on the statistics of the dilatation at the shock. In particular, we are interested in STI when turbulence is strong. In this context, we first introduce a generalization of the analysis (Donzis, 2012*b*) which requires a redefinition of integrals to compute statistical moments across planes parallel to the shock surface.

Consider a laminar shock and a quantity q that depends on the upstream Mach number, M , that is $q = q(M)$. Under QE, one can write q as a function of the local instantaneous Mach number, that is $q = q(M + m)$ where m is the fluctuating Mach

number. In general, the n -th order moment of q is given by the integral

$$\langle q^n \rangle = \int_{-\infty}^{\infty} q^n(M+m) f_m(m) dm \quad (\text{III.20})$$

where $f_m(m)$ is the p.d.f. of m .

However, the actual functional form of $q(M+m)$ may depend on whether the flow is supersonic or subsonic. For example, in locations where the flow is supersonic upstream of the mean location of the shock, the pressure will change according to the Rankine-Hugoniot relations. However, if the flow is subsonic (due to strong negative m fluctuations), then Rankine-Hugoniot relations are invalid. This, as we argued in Donzis (2012*b*) creates holes in the shock surface.

Upstream of the shock (x_1) the instantaneous Mach number is given by $M+m$. For the flow to be supersonic one needs $M+m > 1$ or, in terms of $\Delta M = M-1$, one needs $m > -\Delta M$. Similarly subsonic regions correspond to fluctuations that satisfy $m < -\Delta M$. Thus, we split the integral in Eq. (III.20) as

$$\langle q^n \rangle = \int_{-\Delta M}^{\infty} (q^>)^n f_m(m) dm + \int_{-\infty}^{-\Delta M} (q^<)^n f_m(m) dm. \quad (\text{III.21})$$

where $q^>$ and $q^<$ are the functional form of q in supersonic and subsonic regions, respectively. For short, the supersonic and subsonic integrals will be denoted by $\langle q^n \rangle^>$ and $\langle q^n \rangle^<$, respectively, that is

$$\langle q^n \rangle = \langle q^n \rangle^> + \langle q^n \rangle^<. \quad (\text{III.22})$$

One can, for example, compute moments of the fluctuating Mach number itself, i.e. $q = m$, for which supersonic and subsonic expressions are the same ($q^> = q^<$).

In this case we have:

$$\langle m^0 \rangle^> = \int_{-\Delta M}^{\infty} f_m(m) dm \quad (\text{III.23a})$$

$$\langle m \rangle^> = \int_{-\Delta M}^{\infty} m f_m(m) dm \quad (\text{III.23b})$$

$$\langle m^2 \rangle^> = \int_{-\Delta M}^{\infty} m^2 f_m(m) dm \quad (\text{III.23c})$$

$$\langle m^0 \rangle^< = \int_{-\infty}^{-\Delta M} f_m(m) dm \quad (\text{III.23d})$$

$$\langle m \rangle^< = \int_{-\infty}^{-\Delta M} m f_m(m) dm \quad (\text{III.23e})$$

$$\langle m^2 \rangle^< = \int_{-\infty}^{-\Delta M} m^2 f_m(m) dm. \quad (\text{III.23f})$$

where we also introduce the zeroth-order moment for conciseness in notation in what follows. Obviously, $\langle m^0 \rangle = 1$ and $\langle m \rangle = 0$. Also note that by definition we can write the turbulent Mach number as:

$$M_t = \sqrt{3} \langle m^2 \rangle^{1/2} = \sqrt{3} \left(\int_{-\infty}^{\infty} m^2 f_m(m) dm \right)^{1/2}. \quad (\text{III.24})$$

It has been known for some time that the velocity field in isotropic turbulence is generally well represented by a normal distribution, that is, it obeys Gaussian statistics (Batchelor, 1953; Monin & Yaglom, 1975*b*). This is indeed the case for our data for both IT and SDT as can be seen in figure III.2(a) where we show even moments of the streamwise velocity component from our DNS database. Gaussian values are included as horizontal dashed lines for reference. We can also see a slight sub-Gaussian behavior for very high orders which has indeed been observed in the tails of velocity p.d.f.s before (Noullez *et al.*, 1997; Jimenez, 1998). In any case,

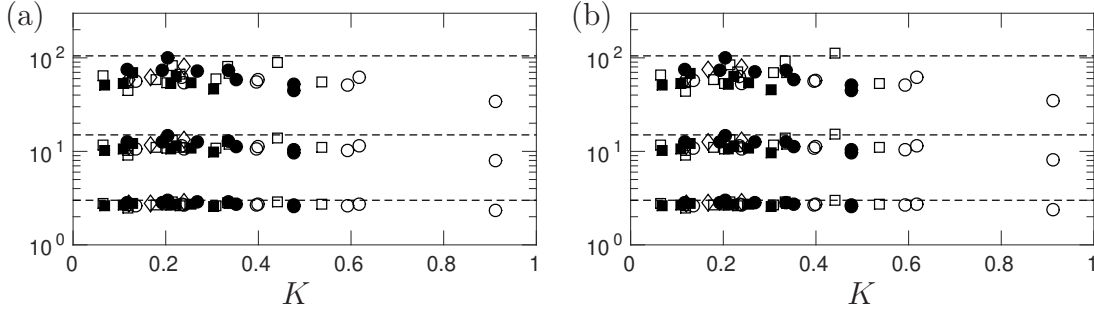


Figure III.2: Even moments of (a) velocity fluctuation $\langle u'^n \rangle / \langle u'^2 \rangle^{n/2}$ and (b) Mach number fluctuation $\langle m^n \rangle / \langle m^2 \rangle^{n/2}$ as function of K at location 1 for all the simulations in tables II.1 and II.2: $M = 1.1$ (circles), $M = 1.2$ (squares), and $M = 1.4$ (diamonds). Open and closed symbols are for IT and SDT simulations. From bottom to top $n = 4, 6$, and 8 . Dashed lines correspond to Gaussian values at 3, 15 and 105, respectively.

our results will rely on at most second order statistics of m for which a Gaussian behavior is an excellent approximation. The same conclusion is also applicable to Mach number fluctuations as shown in figure III.2(b).

For reference, the first few truncated moments of m for a Gaussian distribution are shown in table III.1 where Eq. (III.24) has been used to write results in terms of ΔM and M_t . Note that the second and fifth rows ($\langle m^0 \rangle^>$ and $\langle m^0 \rangle^<$) represent the probability of finding—or fraction of the shock area with—supersonic and subsonic regions, respectively. In fact, in Donzis (2012b) we argued that, consistent with QE, holes in the shocks are caused by locally subsonic conditions. Then $\langle m^0 \rangle^<$ would represent the fraction of the shock with subsonic regions and holes. This analytical form is shown in figure III.3 as a solid line. One can see that the subsonic fraction upstream of the shock is negligible for $M_t/\Delta M \lesssim 0.6$ but grows quickly with $M_t/\Delta M$ beyond that. Thus, one expects to observe holes at $M_t/\Delta M \gtrsim 0.6$ (Donzis, 2012b) in what is now called the *broken* regime. This criterion has indeed been supported

$f_m(m)$	$\frac{1}{M_t} \sqrt{\frac{3}{2\pi}} e^{-\frac{3m^2}{2M_t^2}}$
$\langle m^0 \rangle^>$	$\frac{1}{2} + \frac{1}{2} \operatorname{erf}\left(\sqrt{\frac{3}{2}} \frac{\Delta M}{M_t}\right)$
$\langle m \rangle^>$	$\frac{M_t}{\sqrt{6\pi}} e^{-\frac{3}{2} \frac{\Delta M^2}{M_t^2}}$
$\langle m^2 \rangle^>$	$\frac{M_t^2}{6} - \frac{\Delta M M_t}{\sqrt{6\pi}} e^{-\frac{3}{2} \frac{\Delta M^2}{M_t^2}} + \frac{M_t^2}{6} \operatorname{erf}\left(\sqrt{\frac{3}{2}} \frac{\Delta M}{M_t}\right)$
$\langle m^0 \rangle^<$	$\frac{1}{2} - \frac{1}{2} \operatorname{erf}\left(\sqrt{\frac{3}{2}} \frac{\Delta M}{M_t}\right)$
$\langle m \rangle^<$	$-\frac{M_t}{\sqrt{6\pi}} e^{-\frac{3}{2} \frac{\Delta M^2}{M_t^2}}$
$\langle m^2 \rangle^<$	$\frac{M_t^2}{6} + \frac{\Delta M M_t}{\sqrt{6\pi}} e^{-\frac{3}{2} \frac{\Delta M^2}{M_t^2}} - \frac{M_t^2}{6} \operatorname{erf}\left(\sqrt{\frac{3}{2}} \frac{\Delta M}{M_t}\right)$

Table III.1: Low order moments of m for a Gaussian distribution.

by recent DNS data (Larsson & Lele, 2009). In the figure we also include results from our own DNS taken as the fraction of subsonic regions observed at $x = x_1$. Excellent agreement is observed which supports both the Gaussian assumption for m as well as the criterion $M_t/\Delta M = 0.6$ to delineate the boundary between wrinkled and broken regimes. The last column in tables II.1 and II.2 indicates the regime of the interaction based on this criterion.

III.B Turbulence Shock Jumps of Thermodynamic Quantities

The Rankine-Hugoniot (RH) relations are analytical solutions of the conservation equations that relate upstream and downstream conditions of an one-dimensional steady shock in a laminar flow. These are commonly referred to as jump conditions and are a function of the upstream mean flow Mach number M alone. In turbulent flows, fluctuations upstream of the shock can modify jumps, an effect that is more prominent as the strength of turbulence increases (Larsson *et al.*, 2013). This can be seen in figure III.4 where we plot plane averages of pressure and density along the

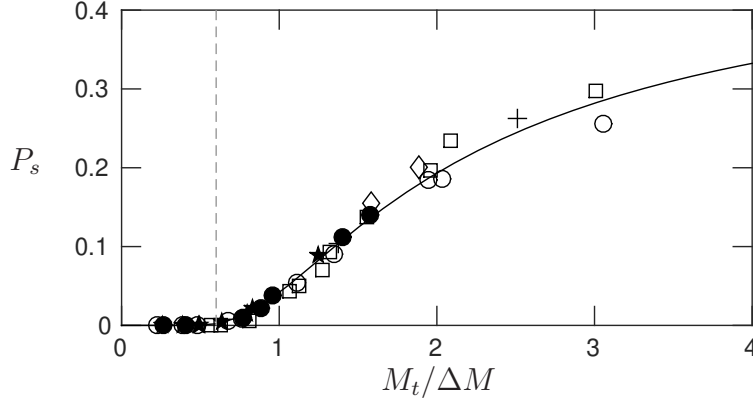


Figure III.3: Probability of subsonic regions upstream of the shock. Solid line: theoretical $P_s = P(m < -\Delta M)$ with Gaussian p.d.f. for m . Symbols for DNS data at $R_\lambda \approx 5$ (stars), $R_\lambda \approx 10$ (circles), $R_\lambda \approx 25$ (squares), $R_\lambda \approx 45$ (diamonds), and $R_\lambda \approx 65$ (plus signs). Open and closed symbols are for IT and SDT simulations, respectively. Gray dashed line at $M_t/\Delta M = 0.6$ for reference.

streamwise direction for different values of M_t . It is clear that as M_t increases the jump weakens compared to the laminar RH jump (horizontal dotted lines) at a fixed $M = 1.2$. More generally, these results demonstrate that thermodynamic jumps across a normal shock depend not only on the mean flow but also on the turbulent fluctuations. This effect cannot be captured by classical theories such as LIA where the only parameter governing the interaction is M . Our objective here is to obtain analytical solutions for shock jumps of thermodynamic variables that can account for the effects of turbulence. The derivations below will rely on the QE assumption.

Consider first the ratio of mean density upstream and downstream of the shock, that is, $\langle \rho_2 \rangle / \langle \rho_1 \rangle$. To compute this ratio we will obtain $\langle \rho_1 \rangle$ and $\langle \rho_2 \rangle$ in turn. We first note that in general the mean density ahead of a shock depends on the levels of fluctuations. A convenient way to account for this is to write the instantaneous

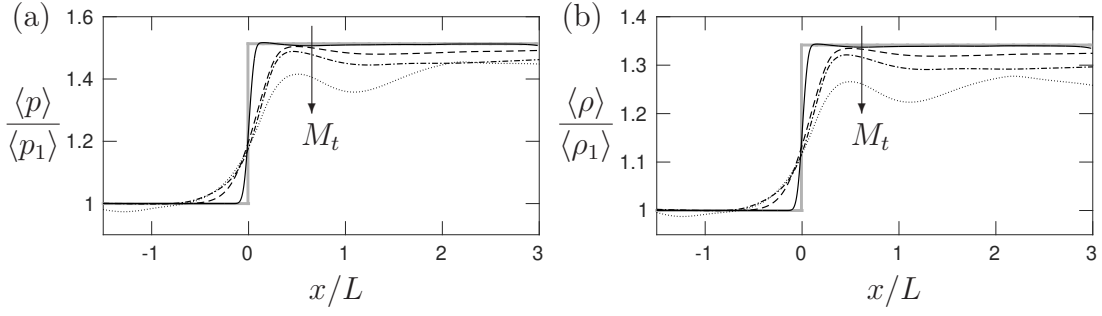


Figure III.4: (a) Pressure and (b) density profile of normal shocks interacting with isotropic turbulence at $M = 1.2$, $R_\lambda \approx 25$ and $M_t = 0.12$ (solid), 0.21 (dashed), 0.32 (dashed-dotted) and 0.44 (dotted). Gray lines correspond to the laminar inviscid limit, namely, RH jumps.

density upstream of the shock in terms of stagnation conditions,

$$\rho_1 = \left[\frac{\gamma - 1}{2} (M + m)^2 + 1 \right]^{-\frac{1}{\gamma-1}} \rho_{01} \quad (\text{III.25})$$

where subscript 0 indicates a stagnation property. Note that Eq. (III.25) is generally valid as stagnation properties can be thought of as a reference state when the flow is brought to rest isentropically even if this does not actually happen. Also note that stagnation properties can be different at different locations and different times. However, if fluctuations are isentropic, then ρ_{01} would be a constant across a plane parallel to the shock (over which averages are taken) independent of local Mach number fluctuations. This is in fact a very reasonable approximation for fluctuations not very far from the mean (Donzis & Jagannathan, 2013). Even if it is not strictly constant, one can also expand the stagnation density in series and if fluctuations are small, one can discard higher order terms and obtain Eq. (III.25) with ρ_{01} being the first term in the expansion. In the derivation that follows we will thus assume ρ_{01} to be a constant.

Expanding Eq. (III.25)) in Taylor series around the mean Mach number yields:

$$\rho_1 = \rho_1|_{m=0} + \left(\frac{\partial \rho_1}{\partial m}\right)_{m=0} m + \frac{1}{2} \left(\frac{\partial^2 \rho_1}{\partial m^2}\right)_{m=0} m^2 + \dots \quad (\text{III.26})$$

The average can then be computed by

$$\langle \rho_1 \rangle = \int_{-\infty}^{\infty} \rho_1 f_m(m) dm. \quad (\text{III.27})$$

Since the integral in this case are over the entire probability space of m , the zeroth-order moment of m would be unity, the first-order moment would be zero and the second-order moment would be $M_t^2/3$ regardless of the specific velocity distribution. Combining Eqs. (III.25), (III.26) and (III.27) and a Gaussian $f_m(m)$ (see table III.1) we can obtain the final form for the mean upstream density:

$$\langle \rho_1 \rangle = \mathbb{M}^{\frac{-1}{\gamma-1}} \rho_{01} + \frac{1}{12} \mathbb{M}^{\frac{-2\gamma+1}{\gamma-1}} [(\gamma+1)M^2 - 2] \rho_{01} M_t^2 \quad (\text{III.28})$$

where, for simplicity in notation, we have defined $\mathbb{M} \equiv (\gamma-1)M^2/2 + 1$. The first term in Eq. (III.28) corresponds to the laminar contribution while the second term corresponds to turbulence effects which depend explicitly on both M and M_t . Clearly, as $M \rightarrow \infty$ or $M_t \rightarrow 0$, the second term vanishes, as expected.

Under the QE assumption, the density immediately downstream of the shock (i.e. location 2') will be given by RH expressions using the local Mach number, that is

$$\rho_{2'}^{>} = \frac{(\gamma+1)(M+m)^2}{(\gamma-1)(M+m)^2 + 2} \rho_1 \quad (\text{III.29})$$

The superscript $>$ has been added to emphasize that shock relations are valid only for supersonic regions. Using Eq. (III.25), the expression becomes:

$$\rho_{2'}^{>} = \left[\frac{(\gamma+1)(M+m)^2}{(\gamma-1)(M+m)^2 + 2} \right] \left[\frac{\gamma-1}{2} (M+m)^2 - 1 \right]^{-\frac{1}{\gamma-1}} \rho_{01}. \quad (\text{III.30})$$

In subsonic regions this expression is clearly invalid and, thus, averages need to be taken using the split form in Eq. (III.22). For subsonic regions, where shock holes appear, one can assume that variables will approximately retain their upstream value considering the shock thickness is relatively small compared to typical turbulence length scales. That is, $\rho_{2'}^< \approx \rho_1$. This assumption is indeed supported by observations of instantaneous density profiles in the broken regime (e.g. Larsson & Lele, 2009). Hence, the average downstream density is given by:

$$\langle \rho_{2'} \rangle = \langle \rho_{2'}^> \rangle + \langle \rho_1 \rangle^< . \quad (\text{III.31})$$

Again, using Taylor series for Eq.(III.30) and substituting into Eq.(III.31) one can integrate the expressions analytically with $f_m(m)$ Gaussian, to obtain

$$\begin{aligned} \langle \rho_{2'} \rangle = & \left[\frac{(\gamma + 1)M^2}{(\gamma - 1)M^2 + 2} \right] \mathbb{M}^{\frac{-1}{\gamma-1}} \rho_{01} \langle m^0 \rangle^> \\ & - \frac{\gamma + 1}{2} M(M^2 - 2) \mathbb{M}^{\frac{-2\gamma+1}{\gamma-1}} \rho_{01} \langle m \rangle^> \\ & + \frac{\gamma + 1}{8} \mathbb{M}^{\frac{-3\gamma+2}{\gamma-1}} [(\gamma + 1)M^4 - (6\gamma + 4)M^2 + 4] \rho_{01} \langle m^2 \rangle^> \\ & + \mathbb{M}^{\frac{-1}{\gamma-1}} \rho_{01} \langle m^0 \rangle^< - M \mathbb{M}^{\frac{-\gamma}{\gamma-1}} \rho_{01} \langle m \rangle^< \\ & + \frac{1}{4} \mathbb{M}^{\frac{-3\gamma+2}{\gamma-1}} [(\gamma + 1)M^2 - 2] \rho_{01} \langle m^2 \rangle^< \end{aligned} \quad (\text{III.32})$$

which, though very complicated, provides an analytical closed form for the mean density downstream of a shock as a function of both M and M_t .

Thus the density jump across a shock in a turbulent flow with mean Mach number M and turbulent mach number M_t can be written as

$$\frac{\langle \rho_{2'} \rangle}{\langle \rho_1 \rangle} = g_\rho(M, M_t) \quad (\text{III.33})$$

where $g_\rho(M, M_t)$ is the ratio of Eq. (III.32) and Eq. (III.25).

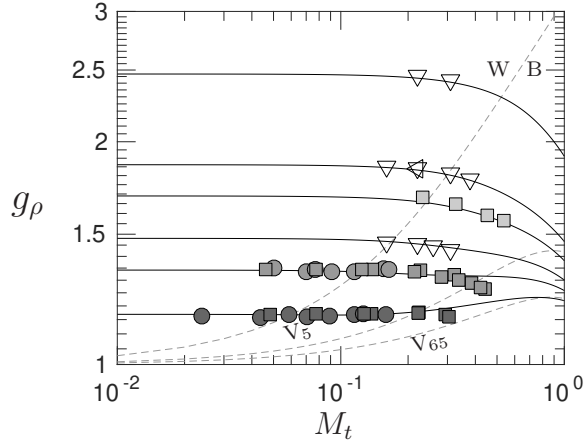


Figure III.5: Mean density jumps from IT (squares) and SDT (circle) simulations at $M = 1.1$ (dark), 1.2 (medium) and 1.4 (light). Other symbols are for Larsson & Lele (2009) (∇), and Larsson *et al.* (2013) (\triangleleft). Solid lines correspond to the analytical solution Eq. (III.33) at $M = 1.1, 1.2, 1.28, 1.4, 1.5$ and 1.87 (bottom to top). Gray dashed line at $M_t/\Delta M = 0.6$ separates the wrinkled (W) and broken (B) regimes. Vanished regime lines at $R_\lambda \approx 5$ (V_5) and $R_\lambda \approx 65$ (V_{65}) also included as gray dashed lines.

In figure III.5 we show $\langle \rho_{2'} \rangle / \langle \rho_1 \rangle$ from DNS data as a function of M_t along with Eq. (III.33). We see very good agreement between DNS data from various sources (symbols) and the theoretical prediction (solid lines). As expected, laminar conditions are recovered as the turbulent Mach number decreases which is seen as solid lines approach their asymptotic RH value at $M_t \rightarrow 0$. It is interesting to note that the effect of turbulent fluctuations depend on the mean Mach number, M . In particular, stronger turbulence effects are observed at higher M . This suggests an interaction between means and fluctuations which is not accounted for in classical theories such as LIA. For relatively high M , an increase in turbulence intensity measured by M_t , results in weakened jumps relative to the laminar situation. Weaker jumps have been observed in simulations before (Larsson *et al.*, 2013) though theoretical predictions

using RDT (Lele, 1992*b*) for example, were argued (Larsson *et al.*, 2013) to remain only qualitatively consistent with the data. The *quantitative* agreement between Eq. (III.33) and data observed in figure III.5, thus, provides support to the adequacy of the QE assumption to capture the two-way coupling which effects changes in mean jumps.

We also see that there is a qualitative change in the effect of turbulence as M decreases. For relatively weak shocks (low M) the theory in fact predicts stronger shock jumps as turbulence intensity increases. Our DNS data do indeed show a consistent, though small, increase with M_t . This low- M conditions may be important in situations around transients crossing sonic conditions such as bodies, vanes, or blades accelerating to supersonic speeds or decelerating to subsonic speeds. At $M \approx 1.2$, jumps appear to be only weakly affected by turbulence with jumps remaining fairly constant with M_t . This transition M , however, is not general and depends on the value of γ . We do note that the conditions under which mean jumps are larger than in a laminar shock at the same M correspond to weak shocks with very intense turbulence, very close to the so-called vanished regime (discussed below and in §IV) which may be challenging to generate reliably and stably in controlled experiments.

In figure III.5 we also show a (dashed) line at constant $M_t/\Delta M = 0.6$ which separates the wrinkled (denoted W in the figure) and broken (denoted B) regimes (Donzis, 2012*b*). Conditions to the left of the WB line correspond to wrinkled interactions where the planar shock retains its structure and is only mildly distorted by the relatively weak incoming turbulent fluctuations. To the right of that line, the interaction is in the broken regime where holes appear across the shock. At even higher turbulent intensities we find (to be discussed more in §III) that turbulence

alters the shock significantly in such a way that Reynolds stresses undergo approximately a classical turbulent decay through the nominal position of the shock and no local extrema at x_1 or x_2 (figure II.3a) forms. In other words, the effect of the shock on the turbulence vanishes. We thus call this the *vanished* regime, which we find emerges for interactions with $K \gtrsim 1.0$, or $M_t/\Delta M \gtrsim R_\lambda^{1/2}$. Lines marking the vanished regime in figure III.5 would then depend on R_λ . For simplicity thus, we include only V lines at the lowest (5) and highest (65) Reynolds numbers in our database with intermediate cases laying between these lines. In the vanished regime, characterized by strong three-dimensional distortion of the shock wave due to very intense turbulence fluctuations, it is not expected that fundamental assumptions behind QE will hold. This may explain the discrepancy seen between theory and DNS data for high- M_t low- M interactions (close to the V lines) in figure III.5.

Following the same procedure described above, one can obtain expressions for $\langle p_1 \rangle$, $\langle p_2 \rangle$, $\langle T_1 \rangle$ and $\langle T_2 \rangle$ as well. Similar to density Eq. (III.25), the expressions for upstream pressure and temperature are given by:

$$p_1 = \left[\frac{\gamma - 1}{2} (M + m)^2 + 1 \right]^{-\frac{\gamma}{\gamma - 1}} p_{01} \quad (\text{III.34a})$$

$$T_1 = \left[\frac{\gamma - 1}{2} (M + m)^2 - 1 \right]^{-1} T_{01}. \quad (\text{III.34b})$$

Under QE, thermodynamic variables downstream of the shock will be given by

RH expressions in supersonic regions:

$$p_{2'}^> = \left[\frac{2\gamma}{\gamma-1}(M+m)^2 - \frac{\gamma-1}{\gamma+1} \right] \left[\frac{\gamma-1}{2}(M+m)^2 \right]^{-\frac{\gamma}{\gamma-1}} p_{01} \quad (\text{III.35a})$$

$$T_{2'}^> = \left[\frac{2\gamma}{\gamma+1}((M+m)^2 - 1) + 1 \right] \left[\frac{(\gamma-1)(M+m)^2 + 2}{(\gamma+1)(M+m)^2} \right] \left[\frac{\gamma-1}{2}(M+m)^2 - 1 \right]^{-1} T_{01} \quad (\text{III.35b})$$

while in subsonic regions we have $p_{2'}^< \approx p_1$ and $T_{2'}^< \approx T_1$.

These four expressions are now expanded around their respective mean as

$$q = q|_{m=0} + \left(\frac{\partial q}{\partial m} \right)_{m=0} m + \frac{1}{2} \left(\frac{\partial^2 q}{\partial m^2} \right)_{m=0} m^2 + \dots \quad (\text{III.36})$$

where $q = p_1, p_{2'}^>, T_1$, or $T_{2'}^>$.

For upstream quantities ($\langle p_1 \rangle$ and $\langle T_1 \rangle$) the averages are computed using complete integrals against the p.d.f. of m . For downstream quantities ($\langle p_{2'} \rangle$ and $\langle T_{2'} \rangle$) one needs to split integrals as in (III.31) to distinguish subsonic from supersonic regions:

$$\langle p_1 \rangle = \int_{-\infty}^{\infty} p_1 f_m(m) dm \quad (\text{III.37a})$$

$$\langle p_{2'} \rangle = \int_{-\Delta M}^{\infty} p_{2'}^> f_m(m) dm + \int_{-\infty}^{-\Delta M} p_1 f_m(m) dm \quad (\text{III.37b})$$

$$\langle T_1 \rangle = \int_{-\infty}^{\infty} T_1 f_m(m) dm \quad (\text{III.37c})$$

$$\langle T_{2'} \rangle = \int_{-\Delta M}^{\infty} T_{2'}^> f_m(m) dm + \int_{-\infty}^{-\Delta M} T_1 f_m(m) dm. \quad (\text{III.37d})$$

Upon integration aided by the forms in Table III.1, the final expressions of mean

pressure and temperature are

$$\langle p_1 \rangle = \mathbb{M}^{\frac{-\gamma}{\gamma-1}} p_{01} + \frac{\gamma}{12} \mathbb{M}^{\frac{-3\gamma+2}{\gamma-1}} [(3\gamma-1)M^2 - 2] p_{01} M_t^2 \quad (\text{III.38a})$$

$$\langle p_{2'} \rangle = \left[\frac{2\gamma}{\gamma+1} M^2 - \frac{\gamma-1}{\gamma+1} \right] \mathbb{M}^{\frac{-\gamma}{\gamma-1}} p_{01} \langle m^0 \rangle^> \quad (\text{III.38b})$$

$$\begin{aligned} & + \frac{\gamma M}{\gamma+1} (-2M^2 + \gamma + 3) \mathbb{M}^{\frac{-2\gamma+1}{\gamma-1}} p_{01} \langle m \rangle^> \\ & + \frac{\gamma}{4(\gamma+1)} \mathbb{M}^{\frac{-3\gamma+2}{\gamma-1}} [(2\gamma+2)M^4 - (3\gamma^2 + 8\gamma + 9)M^2 + (2\gamma+6)] p_{01} \langle m^2 \rangle^> \\ & + \mathbb{M}^{\frac{-\gamma}{\gamma-1}} p_{01} \langle m^0 \rangle^< - \gamma M \mathbb{M}^{\frac{-2\gamma+1}{\gamma-1}} p_{01} \langle m \rangle^< \\ & + \frac{\gamma}{4} \mathbb{M}^{\frac{-3\gamma+2}{\gamma-1}} [(3\gamma-1)M^2 - 2] p_{01} \langle m^2 \rangle^< \end{aligned} \quad (\text{III.38c})$$

$$\langle T_1 \rangle = \mathbb{M}^{-1} T_{01} + \frac{\gamma-1}{12} \mathbb{M} [(3\gamma-3)M^2 - 2] T_{01} M_t^2 \quad (\text{III.38d})$$

$$\begin{aligned} \langle T_{2'} \rangle & = \left[\frac{2\gamma}{\gamma+1} (M^2 - 1) + 1 \right] \left[\frac{(\gamma-1)M^2 + 2}{(\gamma+1)M^2} \right] \mathbb{M}^{-1} T_{01} \langle m^0 \rangle^> \\ & + \frac{4(\gamma-1)}{(\gamma+1)^2 M^3} T_{01} \langle m \rangle^> - \frac{6(\gamma-1)}{(\gamma+1)^2 M^4} T_{01} \langle m^2 \rangle^> \\ & + \mathbb{M}^{-1} T_{01} \langle m^0 \rangle^< - (\gamma-1) M \mathbb{M}^{-2} T_{01} \langle m \rangle^< \\ & + \frac{\gamma-1}{4} \mathbb{M}^{-3} [3(\gamma-1)M^2 - 2] T_{01} \langle m^2 \rangle^<, \end{aligned} \quad (\text{III.38e})$$

where, as in the main text, we have defined $\mathbb{M} = (\gamma-1)M^2/2 + 1$ for convenience.

The final result is simplified as

$$\frac{\langle p_{2'} \rangle}{\langle p_1 \rangle} = g_p(M, M_t) \quad (\text{III.39})$$

$$\frac{\langle T_{2'} \rangle}{\langle T_1 \rangle} = g_T(M, M_t). \quad (\text{III.40})$$

The ratio of the corresponding expressions yield the expressions of thermody-

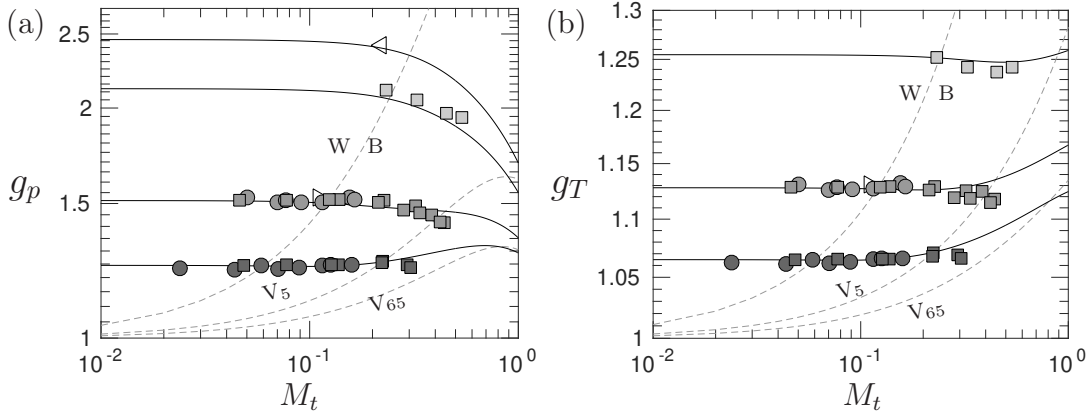


Figure III.6: Mean pressure and temperature jumps from IT (squares) and SDT (circles) simulations, Lee *et al.* (1993) (\triangleright) and Larsson *et al.* (2013) (\triangleleft). Solid lines correspond to the analytical solution (III.38) at $M = 1.1, 1.2, 1.4$, and 1.5 (bottom to top). Gray dashed line at $M_t/\Delta M = 0.6$ separates the wrinkled (W) and broken (B) regimes. Vanished regime lines at $R_\lambda \approx 5$ (V_5) and $R_\lambda \approx 65$ (V_{65}) also included as gray dashed lines.

namic shock jumps denoted in Eq. (III.33), Eq. (III.39) and Eq. (III.40).

The comparison between DNS data and Eq. (III.39) and Eq. (III.40) is shown in figure III.6. Again, good agreements are observed at a range of M_t . While the behavior of pressure is very similar to that of density we see that that of temperature is not. In fact, trends appear inverted: at low M effects are stronger and jumps become larger as M_t increases. At high M , effects are weaker and there is a slight decrease in jumps as M_t increases.

It is interesting that while it has been argued in the literature that stronger turbulence leads to weakened shock jumps (Lele, 1992*a*), the data presented here suggest a more complex interaction. In particular, whether turbulence weakens or strengthens shock jumps depends on the specific combination of M_t , and M . The theoretical results here can, in fact, provide the necessary guidance to understand this

observation. Consider the relative change of the density jump $\langle \rho_2 \rangle / \langle \rho_1 \rangle = g_\rho(M, M_t)$ with respect to the laminar RH jump, $g_\rho^{RH}(M)$:

$$R_\rho(M, M_t) = \frac{g_\rho(M, M_t) - g_\rho^{RH}(M)}{g_\rho^{RH}(M)} \quad (\text{III.41})$$

This function, which with Eq. (III.33) is known analytically, provides direct information of the effect of turbulence on the jumps of mean thermodynamic quantities. This is shown in figure III.7(a) where we can now clearly see that the effect of turbulence on jumps depends on both M and M_t . In general for low M , an increase of turbulence intensity (M_t) leads to stronger shocks ($R_\rho(M, M_t) > 0$) relative to a laminar shock at the same M . However, as M increases $R_\rho(M, M_t)$ changes sign and jumps become weaker. At higher M , $R_\rho(M, M_t)$ decrease monotonically towards zero from below indicating a vanishing turbulence effect as $M \rightarrow \infty$. A similar general behavior is observed for the similarly defined $R_p(M, M_t)$ and $R_T(M, M_t)$ shown in figure III.7.

Two characteristic Mach numbers can now be identified for $R_\rho(M, M_t)$. First, we identify $M_{cr}^\rho(M_t)$ as the critical Mach number at which $R_\rho(M, M_t)$ changes sign. This can be readily found by solving $R_\rho(M, M_t) = 0$ numerically for fixed M_t . The result is shown in figure III.8(a) along with the critical Mach numbers for pressure and temperature. We see that, while qualitatively similar, the critical Mach number is numerically different for ρ , p and T . Conditions below and above the corresponding $M_{cr}(M_t)$ lines represent stronger and weaker shock jumps respectively for the different thermodynamic variables. We can also see that the critical Mach number appears mainly in the broken regime (between the W-B and V_5 lines).

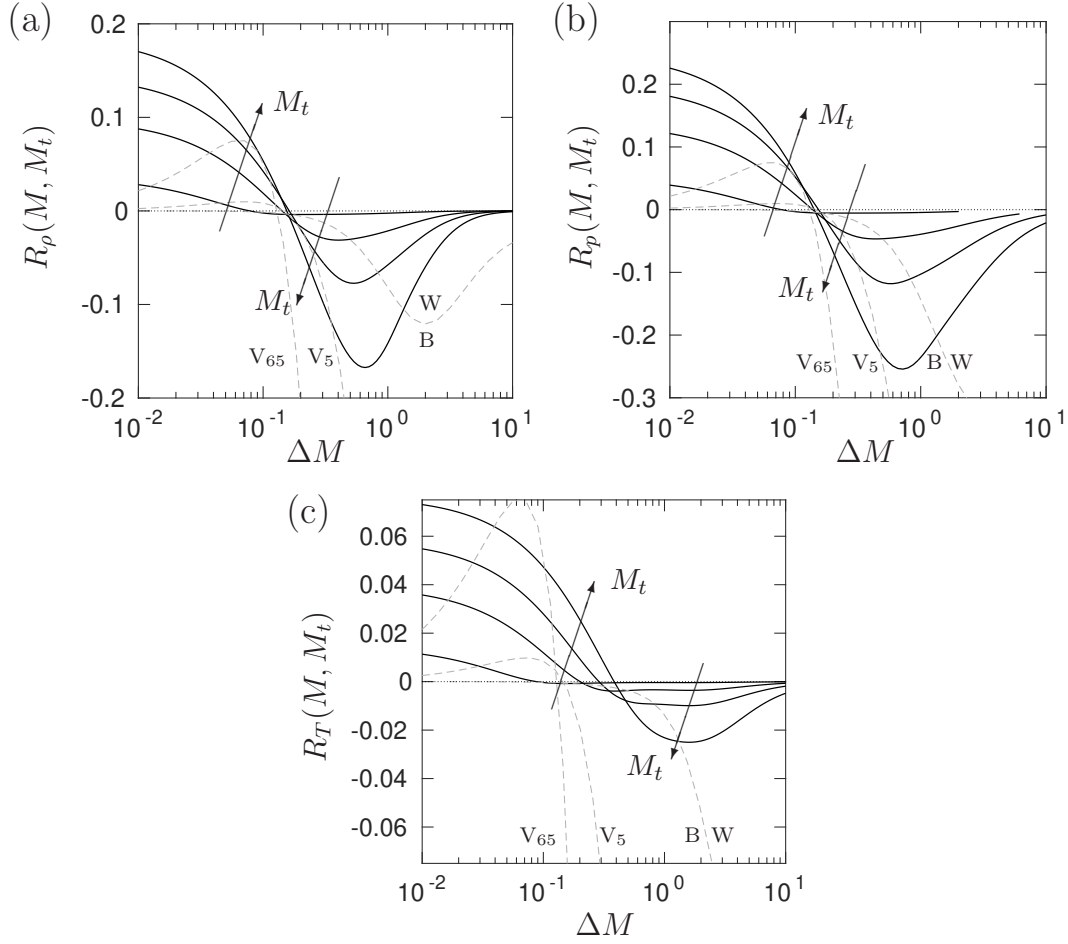


Figure III.7: Relative departures from laminar RH jumps for (a) density $R_\rho(M, M_t)$, (b) pressure $R_p(M, M_t)$, and (c) temperature $R_T(M, M_t)$ at $M_t = 0.1, 0.3, 0.5$, and 0.8 . Gray dashed line at $M_t/\Delta M = 0.6$ separates the wrinkled (W) and broken (B) regimes. Vanished regime lines at $R_\lambda \approx 5$ (V_5) and $R_\lambda \approx 65$ (V_{65}) also included as gray dashed lines.

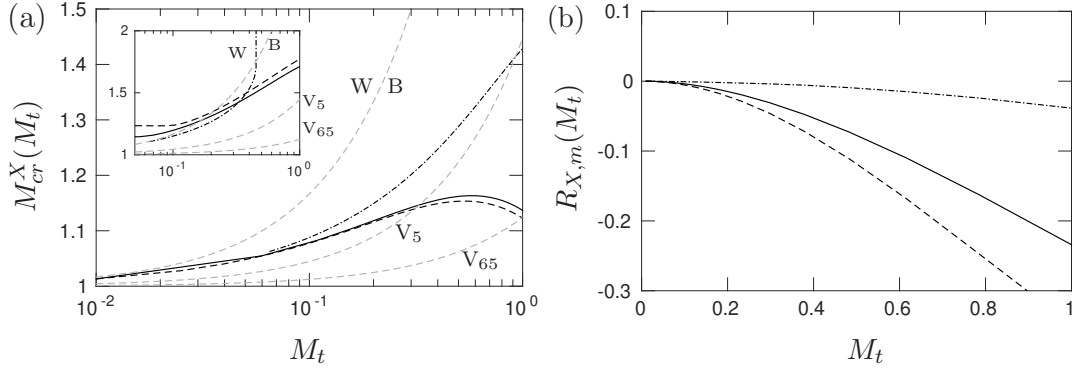


Figure III.8: (a) Critical Mach numbers ($M_{cr}^X(M_t)$) for density ($X = \rho$, solid), pressure ($X = p$, dashed), and temperature ($X = T$, dashed-dotted). Gray dashed line at $M_t/\Delta M = 0.6$ separates the wrinkled (W) and broken (B) regimes. Vanished regime lines at $R_\lambda \approx 5$ (V_5) and $R_\lambda \approx 65$ (V_{65}) also included as gray dashed lines. (b) Maximum weakening of shock jumps due to turbulence measured as the maximum relative departure from RH relations for density ($X = \rho$, solid), pressure ($X = p$, dashed), and temperature ($X = T$, dash-dotted) for a given M_t .

An interesting prediction by the theory is the existence of conditions at which pressure and density jumps are weakened by turbulence ($M > M_{cr}^\rho$ and $M > M_{cr}^p$) while temperature jumps are strengthened ($M < M_{cr}^T$). This is indeed supported by our DNS data at $M_t = 0.39$ and $M = 1.2$ where temperature experiences an increase stronger than RH while pressure and density experience a weaker-than-RH increase across the shock. This is seen in figure III.9(a) where we plot DNS data for this case along with RH jumps for this condition. In figure III.9(b) we show a condition where all thermodynamic variables experience a stronger-than-RH jump due to turbulence.

A second characteristic Mach number is the location of the minimum observed for given M_t in figure III.7. This corresponds to the condition at which the largest turbulent effects are observed, and are denoted by $M_m^\rho(M_t)$, $M_m^p(M_t)$, and $M_m^T(M_t)$ for density, pressure and temperature, respectively. These can be obtained by solving $\partial R_\rho(M, M_t)/\partial M = 0$ and similar equations for density and pressure. The result is

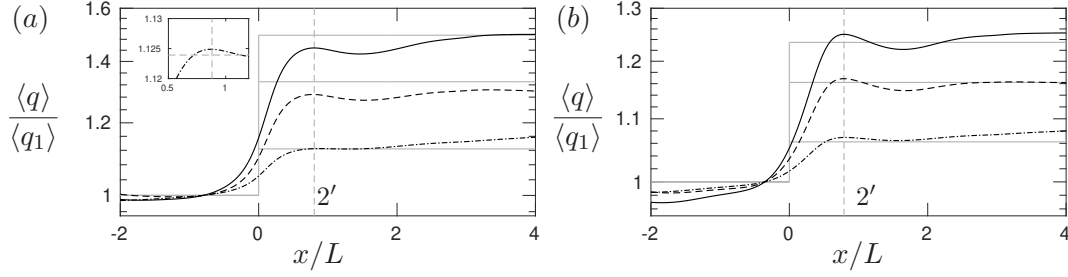


Figure III.9: Variation of normalized pressure (solid, $q = p$), density (dashed, $q = \rho$) and temperature (dash-dotted, $q = T$) across the shock. (a) $(M, M_t, R_\lambda) \approx (1.2, 0.39, 13)$ which corresponds to $M < M_{cr}^T$ and $M > M_{cr}^p, M_{cr}^\rho$. Inset: detailed view of temperature around $x_{2'}$. (b) $(M, M_t, R_\lambda) \approx (1.1, 0.29, 10)$ which corresponds to $M < M_{cr}^T, M_{cr}^p, M_{cr}^\rho$. Grey solid lines represent the laminar inviscid limits. Vertical grey dashed lines indicate the location of $x_{2'}$.

shown in the inset of figure III.8(a). $M_m(M_t)$ also is mainly in the broken regime though the three thermodynamic quantities lie close to each other and to the W-B line. However, for higher M_t we see $M_m^T(M_t)$ grows substantially indicating that the strongest turbulence effect on temperature moves to higher values of M .

The analysis here also suggests that, for a fixed M_t , there is a bound on how much a shock can be weakened by turbulence. This is given by the minimum value of $R_\rho(M, M_t)$ ($R_{\rho,m}$ for short), which occurs at the second characteristic Mach number, that is $R_{\rho,m} \equiv R_\rho(M_m^\rho(M_t), M_t)$. This is shown in figure III.8(b) where we see that pressure jumps can be of the order of 30% weaker at high M_t . Weakening of temperature jumps however, are much smaller, staying below $\sim 5\%$ for the Mach numbers studied here. The Mach number at which this maximum effect is realized can be obtained from figure III.7 or the full analytical expressions.

As a good agreement is obtained by comparing the analytical solutions to the DNS data, we expect that our solutions approach to laminar values at $M_t \rightarrow \infty$. In laminar supersonic flows, density jump is solely dependent on M . With increasing M ,

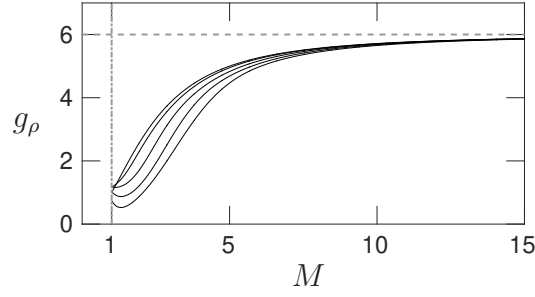


Figure III.10: Theoretical solution of density jump from Eq. (III.33) in terms of M and M_t .

the density jump would saturate and become a constant, $(\gamma+1)/(\gamma-1)$, in hypersonic flows. Though we have shown that turbulence modifies the shock jumps, previous discussion also mentioned that this turbulent effects would gradually disappear with M . This implies that our derived equations would approach to laminar flows in hypersonic condition. Figure III.10 shows the density jumps from Eq. (III.33) in terms of M and M_t . At relatively weak shocks, an evident M_t dependence is observed. But such dependence quickly vanishes when the flows transition from supersonic to hypersonic. Our solution of density jump shows that the jump would saturate at hypersonic limit. This saturation verifies that turbulence effects become negligible at high M and the solution predicts similar laminar results.

Finally, we turn to entropy which is also expected to contain both laminar and turbulent contributions. In general the entropy change as a perfect gas moves from a thermodynamic state A to another one B can be written as $\Delta s = C_p \ln(T_B/T_A) - R \ln(p_B/p_A)$. In a laminar shock, the states A and B correspond to the upstream and downstream locations, respectively. In a turbulent flow, as before, one can use

QE to obtain the mean entropy jump across a shock as:

$$\langle \Delta s \rangle = \langle \Delta s^< \rangle^< + \langle \Delta s^> \rangle^> \quad (\text{III.42})$$

For supersonic regions we have

$$\Delta s^> = C_p(\ln T_{2'} - \ln T_1) - R(\ln p_{2'} - \ln p_1), \quad (\text{III.43})$$

for which the different terms can be computed as before. The logarithm of the instantaneous temperature and pressure in terms of M and m are

$$\ln p_1 = \ln \left(\left[\frac{\gamma-1}{2}(M + \tilde{m})^2 + 1 \right]^{-\frac{\gamma}{\gamma-1}} p_{01} \right) \quad (\text{III.44a})$$

$$\ln p_{2'} = \ln \left(\left[\frac{2\gamma}{\gamma-1}(M + \tilde{m})^2 - \frac{\gamma-1}{\gamma+1} \right] \left[\frac{\gamma-1}{2}(M + \tilde{m})^2 \right]^{-\frac{\gamma}{\gamma-1}} p_{01} \right) \quad (\text{III.44b})$$

$$\ln T_1 = \ln \left(\left[\frac{\gamma-1}{2}(M + m)^2 + 1 \right]^{-1} T_{01} \right) \quad (\text{III.44c})$$

$$\ln T_{2'} = \ln \left(\left[\frac{2\gamma}{\gamma+1}((M + m)^2 - 1) + 1 \right] \left[\frac{(\gamma-1)(M + m)^2 + 2}{(\gamma+1)(M + m)^2} \right] \left[\frac{\gamma-1}{2}(M + \tilde{m})^2 - 1 \right]^{-1} T_{01} \right) \quad (\text{III.44d})$$

which upon expanding in Taylor series and averaging leads to:

$$\langle \ln p_1 \rangle^> = \ln \left(\mathbb{M}^{-\frac{\gamma}{\gamma-1}} \right) + \frac{\gamma}{12} [(\gamma-1) M^2 - 2] \mathbb{M}^{-2} M_t^2 + \ln p_{01} \quad (\text{III.45a})$$

$$\begin{aligned} \langle \ln p_{2'} \rangle^> = & \ln \left(\left[\frac{2\gamma}{\gamma+1} M^2 - \frac{\gamma-1}{\gamma+1} \right] \mathbb{M}^{\frac{-\gamma}{\gamma-1}} \right) \langle m^0 \rangle^> \\ & + \frac{\gamma M (-2M^2 + \gamma + 3)}{2\gamma M^2 - \gamma + 1} \mathbb{M}^{-1} \langle \tilde{m} \rangle^> \\ & + \gamma \left[-\mathbb{M}^{-2} + \frac{\mathbb{M}^{-1}}{2} + \frac{4-4\gamma}{(-2\gamma M^2 + \gamma - 1)^2} - \frac{2}{(2\gamma M^2 - \gamma + 1)} \right] \langle \tilde{m}^2 \rangle^> \\ & + \ln \left(\mathbb{M}^{-\frac{\gamma}{\gamma-1}} \right) \langle \tilde{m}^0 \rangle^< - \gamma M \mathbb{M}^{-1} \langle \tilde{m} \rangle^< \\ & + \frac{\gamma}{12} [(\gamma-1) M^2 - 2] \mathbb{M}^{-2} \langle \tilde{m}^2 \rangle^< + \ln p_{01} \end{aligned} \quad (\text{III.45b})$$

$$\langle \ln T_1 \rangle^> = \ln \left(\mathbb{M}^{-1} \right) + \frac{(\gamma-1) [(\gamma-1) M^2 - 2]}{3 [(\gamma-1) M^2 + 2]} M_t^2 + \ln T_{01} \quad (\text{III.45c})$$

$$\begin{aligned} \langle \ln T_{2'} \rangle^> = & \ln \left(\left[\frac{2\gamma}{\gamma+1} (M^2 - 1) + 1 \right] \left[\frac{(\gamma-1) M^2 + 2}{(\gamma+1) M^2} \right] \mathbb{M}^{-1} \right) \langle m^0 \rangle^> \\ & + \frac{2(\gamma-1)}{2\gamma M^3 - \gamma M + M} \langle \tilde{m} \rangle^> - \frac{(\gamma-1) [\gamma(6M^2 - 1) + 1]}{(2\gamma M^3 - \gamma M + M)^2} \langle \tilde{m}^2 \rangle^> \\ & + \ln \left(\mathbb{M}^{-1} \right) \langle \tilde{m}^0 \rangle^< - \frac{-2(\gamma-1)M}{2 + (\gamma-1)M^2} \langle \tilde{m} \rangle^< \\ & + \frac{(\gamma-1) [(\gamma-1) M^2 - 2]}{2\mathbb{M}^2} \langle \tilde{m}^2 \rangle^< + \ln T_{01}. \end{aligned} \quad (\text{III.45d})$$

Finally, the averaged entropy jump at supersonic regions is obtained from Eq. (III.45),

$$\langle \Delta s \rangle^> = [C_p (\langle \ln T_{2'} \rangle^> - \langle \ln T_1 \rangle^>) - R (\langle \ln p_{2'} \rangle^> - \langle \ln p_1 \rangle^>)] \langle m^0 \rangle^>, \quad (\text{III.46})$$

For subsonic regions where there is no shock, the entropy increase will be solely due to the dissipative nature of turbulence. Obukhov (1949) showed that entropy generation due to turbulent fluctuations is proportional to the temperature variance. Specifically he showed that when the flow decays from a state characterized by a temperature variance $\langle T'^2 \rangle$, the entropy increase when fluctuations have decayed to

zero is $\langle \Delta s \rangle \approx C_p \langle T'^2 \rangle / \langle T \rangle^2$. In the present cases, turbulence will not be completely dissipated as it crosses the shock region and reaches $x_{2'}$. However, it is still expected that the entropy increase will be proportional to the variance of temperature of the incoming flow. Furthermore, this variance can be written in terms of the turbulent Mach number as $\langle T'^2 \rangle / \langle T \rangle^2 \approx (A^2/9)(\gamma - 1)^2 M_t^4$ (Donzis & Jagannathan, 2013). Thus, by taking conditional averages for the subsonic regions one can expect

$$\langle \Delta s^< \rangle^< = \alpha_s C_p (\gamma - 1)^2 M_t^4 \langle m^0 \rangle^<, \quad (\text{III.47})$$

where all prefactors are absorbed in the constant α_s .

Finally, with (III.46) and (III.47) we can obtain the entropy jump across a turbulent shock wave:

$$\frac{\langle \Delta s \rangle}{C_p} = g_s(M, M_t). \quad (\text{III.48})$$

The DNS data of entropy jump across the shock along with the theoretical prediction Eq. (III.48) are shown in figure III.11. The comparison shows a good agreement though there are some scatters in the data. At very low M_t , the change of entropy is due entirely to the well known laminar jumps (Thompson, 1984). As M_t increases, we see a substantial increase in entropy production by both DNS and the theoretical prediction Eq. (III.48).

The theoretical result approaches an asymptotic M_t^4 at high M_t indicating that turbulent entropy generation replaces the shock contribution and becomes the dominant mechanism. Note that the supersonic regions also contains ‘‘turbulence effects’’: this is seen, for example, from the second term in Eq. (III.45c) which vanishes as the

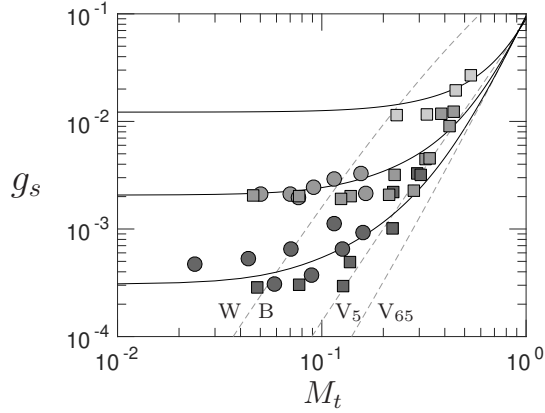


Figure III.11: Mean entropy increase from IT (■) and SDT (●) simulations. Solid lines correspond to the analytical solution (III.48) at $M = 1.1, 1.2, 1.4$, and 1.5 (bottom to top) with $\alpha_s = 1.176$. Gray dashed line at $M_t/\Delta M = 0.6$ separates the wrinkled (W) and broken (B) regimes. Vanished regime lines at $R_\lambda \approx 5$ (V_5) and $R_\lambda \approx 65$ (V_{65}) also included as gray dashed lines.

incoming flow fluctuations weakens ($M_t \rightarrow 0$). However, the asymptotic behavior of these terms is a weaker power law than M_t^4 . Furthermore, the entropy increase through shock holes is independent of the mean Mach number as it only reflects entropy production due to turbulent dissipation. Thus, the observed decreasing gap between curves at different M as M_t increases is also supportive of an increasingly dominant contribution from turbulent decay.

To further verify our solution of Eq. (III.48), we have to assure that entropy jump does not violate the second laws of thermodynamics. Since both shock waves and turbulence are highly dissipative phenomena, the entropy jumps in STI should always be greater than zero. Figure III.12 shows the derived entropy jumps from Eq. (III.48) at wide ranges of M and M_t . Regardless the conditions of the flow, our solution always satisfies the second law of thermodynamics. Figure III.12 also indicates that at low M , the entropy jump can change several orders depends on the

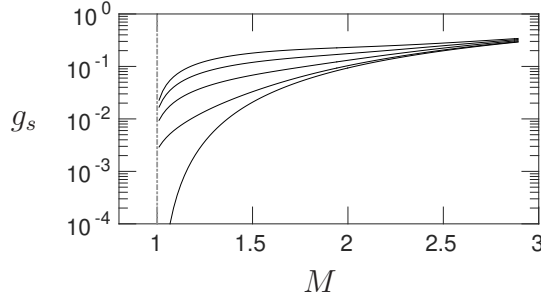


Figure III.12: Theoretical solution of density jump from Eq. (III.33) in terms of M and M_t .

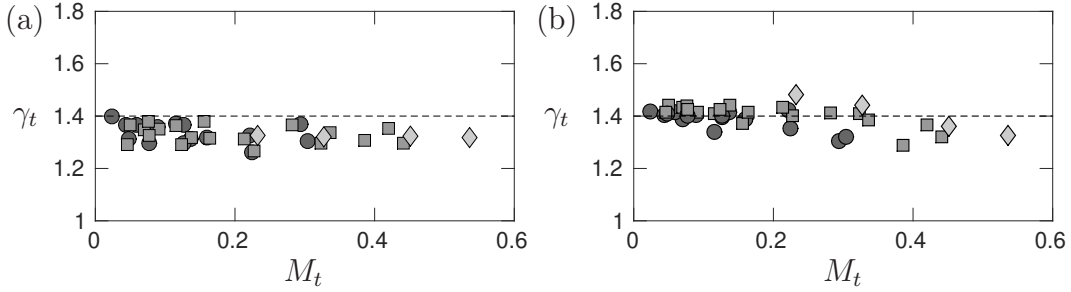


Figure III.13: Polytropic exponents at (a) $x = 1$ and (b) $x = 2'$ from IT (squares) and SDT (circle) simulations at $M = 1.1$ (dark), 1.2 (medium) and 1.4 (light). Solid lines correspond to the isentropic value, 1.4 .

turbulent intensity. However, such dependence disappears at high M .

From the analytical solutions and DNS data, the entropy jumps show no dependence on R_λ . In both supersonic and subsonic formulations of the entropy jump, the flows are assumed isentropic and the effects of irreversible process on entropy is considered negligible. This assumption is verified by examining the relation

$$\frac{p'}{\langle p \rangle} = \gamma_t \frac{\rho'}{\langle \rho \rangle} = \frac{\gamma_t}{\gamma_t - 1} \frac{T'}{\langle T \rangle} \quad (\text{III.49})$$

where γ_t is a polytropic exponent. For a valid isentropic assumption, γ_t would be

equal to $\gamma = 1.4$. Figure III.13 shows that, despite some scatter, the flows upstream and downstream of the shock are very close to isentropic condition. Though there are irreversible dissipations inside the shock, our DNS data suggests that such viscous contribution is small. Thus, we obtain a good agreement between present simulations and theoretical solutions which show no R_λ effects on entropy jump as well as other thermodynamic variables.

III.C Summary

We conclude this section with a few remarks about the generality of the results presented here. First, we note that there seems to be a negligible Reynolds number effect for mean jumps. This may not be completely unexpected since RH jumps can be shown to be the same in viscous or inviscid flows—molecular transport properties (viscosity and thermal conductivity) only determine the structure of the shock (Zeldovich & Raizer, 2002). Thus, the sole dependence on M and M_t in Eq. (III.33)-Eq. (III.40) is indeed a very general form under QE for jumps of mean thermodynamic variables. This is also an important result from the point of view of assumptions behind theoretical models. For example, in LIA, the problem setup is such that the mean properties downstream of the shock are uniquely determined by RH jumps using only mean upstream conditions. Fluctuations are then solved independently superimposed on this mean field. However, as we showed above using DNS data, even mean properties depend on both ΔM and M_t . This effect needs to be incorporated if models are to capture STI with relatively strong turbulence. Second, we note that there is little difference between the jumps observed for isotropic and anisotropic turbulence in IT and SDT simulations, respectively. This suggests that the QE as-

sumption, with its implication of a one-dimensional locally laminar shock governed by the upstream streamwise Mach number, seems to provide an accurate description even at relatively high turbulence intensities (though not perhaps in the vanished regime). Finally, we stress that conclusions here result from calculating quantities at $x_{2'}$ which can be argued to be still unaffected by turbulent mixing downstream of the shock. At x_2 , however, quantities are expected to be affected by turbulence processes and indeed Reynolds number effects have been observed (Andreopoulos *et al.*, 2000; Donzis, 2012*a*). These observations are consistent with separate regions, one where the flow is dominated by “shock effects” ($x < x_{2'}$), and another one where it is dominated by “turbulence effects” ($x > x_2$). The region $x_{2'} < x < x_2$ can then be thought of as a transition region where the fully developed incoming turbulence has been deeply distorted by the shock and is evolving towards its fully developed state, which is achieved at x_2 . Beyond this point a traditional turbulence decay is observed. Thus, while anisotropy may not play a major role in determining mean thermodynamic jumps for $x < x_{2'}$ (as the data above suggests), it will in regions affected ($x_{2'} < x < x_2$) or dominated ($x > x_2$) by turbulence processes (Ryu & Livescu, 2014; Livescu & Ryu, 2016). We stress though that, while our data support this picture, it is unclear to what degree the flow will consist of “pure” regions dominated exclusively by one of these processes. Detailed investigations of this conceptual picture and the relative dominance of different process in each region is worth pursuing, but beyond the objectives here.

IV. SHOCK STRUCTURE

IV.A Scaling of Rms-to-mean Shock Dilatation

The effects of turbulence on shock characteristics have been studied theoretically in the literature (Ribner, 1954*a,b*; Williams & Howe, 1973; Zank *et al.*, 2002; Wouchuk *et al.*, 2009) under different sets of assumptions. Experimental (Hesselink & Sturtevant, 1988) and numerical observations (Lee *et al.*, 1993; Larsson & Lele, 2009), have also observed strong modification of the shock due to turbulence fluctuations. These investigations helped identified two regimes in the interaction which result from different levels of turbulence intensity. These are the so-called wrinkled and the broken regimes respectively. The former corresponds to a interaction in which the shock retains its structure as a sharp gradient over a weakly modified uniform shock plane. The latter corresponds to a strongly modified shock plane with “holes” through which properties may change smoothly or have multiple peaks (Hesselink & Sturtevant, 1988; Lee *et al.*, 1993).

The determination of the regimes has been traditionally done using visual inspection of visualizations from simulations. In Donzis (2012*b*) we proposed a specific mechanism leading to broken shocks based on hole creations due to the appearance of subsonic regions ahead of the shock. This led to the prediction $M_t/\Delta M = 0.6$ as the condition dividing wrinkled and broken regimes (see W-B line in figures III.5 and III.6 and more detailed discussion later on in this section) which has since, been supported by DNS data (Larsson *et al.*, 2013).

A quantitative metric that has been used to characterize inhomogeneities in the

structure of the shock is the rms-to-mean dilatation at the shock (Lee *et al.*, 1993; Larsson & Lele, 2009)

$$\Theta = \left(\frac{\langle \theta_s^2 \rangle_s}{\langle \theta_s \rangle_s^2} - 1 \right)^{1/2} \quad (\text{IV.1})$$

where θ_s is the dilatation at the shock location which is identified as the largest negative value of dilatation along the streamwise direction x for a given location (y, z) . That is $\theta_s(y, z) = \min_x \theta(x, y, z)$. Note that since the location where θ attains its minimum is, in general, different for different locations (y, z) , the averages in Eq. (IV.1) are not over planes at fixed x , but instead over all $\theta_s(y, z)$ —we use the additional subscript s in $\langle \cdot \rangle_s$, to differentiate it from plane averages $\langle \cdot \rangle$. DNS data presented below is also time averaged.

To estimate Θ , $M_t^2/(M^2 - 1)$ was first being used in the discussion by (Lee *et al.*, 1993). As shown in figure IV.1(a), this parameter only captures the trend of Θ qualitatively leaving the data scattered in broken regime. Following Donzis (2012b), one can write the maximum negative dilatation at the shock as $\theta_s \approx [u]/\delta_t$ where $[u]$ is the velocity change across the shock and δ_t the shock thickness which, to leading order, can be written as $(\rho c/\mu)[u](\Delta M + m)$. Using unconditional averages over the entire surface and assuming $[u]$ is, to leading order, not affected by fluctuations, QE leads to $\langle \theta_s \rangle_s \sim (\langle \rho_1 \rangle \langle c_1 \rangle / \langle \mu_1 \rangle) [u] \Delta M$ and $\langle \theta_s^2 \rangle_s \sim (\langle \rho_1 \rangle \langle c_1 \rangle / \langle \mu_1 \rangle)^2 [u]^2 (\Delta M + M_t^2/3)$ which, when used in Eq. (IV.1), leads to:

$$\Theta \approx \frac{1}{\sqrt{3}} \frac{M_t}{\Delta M} . \quad (\text{IV.2})$$

This has been shown to provide good collapse of the existing data (Donzis, 2012b;

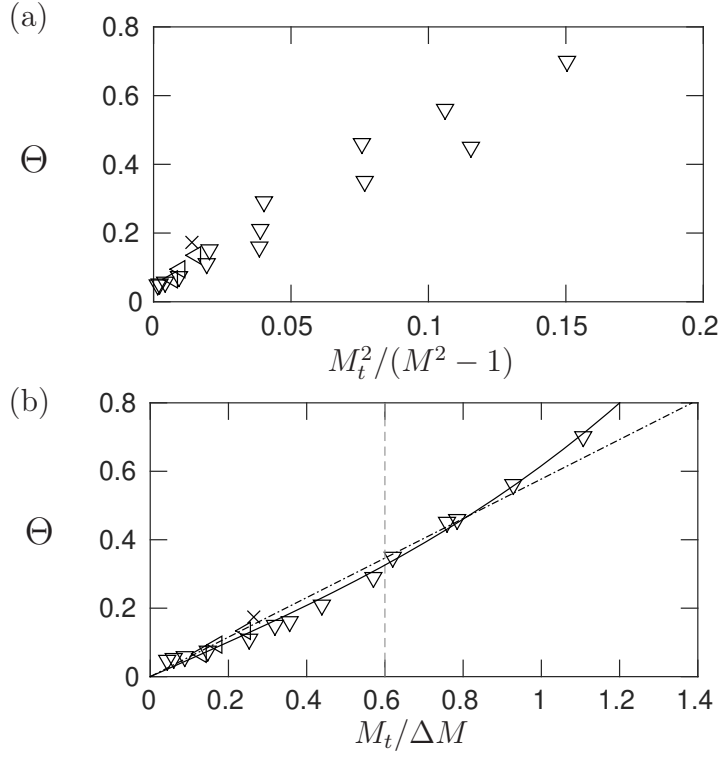


Figure IV.1: Rms-to-mean dilatation at the shock plotted as a function of (a) $M_t/(M^2 - 1)$ and (b) $M_t/\Delta M$. Dash-dotted lines is Eq. (IV.2) and solid lines is best fit with $e_1 = 0.502$ and $e_2 = 0.114$. Vertical gray dashed line at $M_t/\Delta M = 0.6$ for reference. Symbols are: Jamme *et al.* (2002)(\times), Larsson & Lele (2009)(∇) and Boukharfane *et al.* (2018)(\triangleleft). Reprinted from (Donzis, 2012b).

Boukharfane *et al.*, 2018). However, Eq. (IV.2) is expected to provides an accurate description of the interaction only when the incoming turbulence is relatively weak. This is indeed the case as seen in figure IV.1(b), where we show Θ in terms of $M_t/\Delta M$ with the available data in the literature. The dash-dotted line is Eq. (IV.2) while the solid line contains the next order term in the expansion (Donzis, 2012b), that is $\Theta \approx e_1 M_t/\Delta M + e_2 (M_t/\Delta M)^3$ where e_1 and e_2 are fitting constants. There is good agreement between the data and the theory in the wrinkled regime ($M_t/\Delta M \lesssim 0.6$) consistent with previous studies (Donzis, 2012b; Boukharfane *et al.*, 2018).

With much stronger turbulence presented in our simulations, shock structure is discussed with extended range of $M_t/\Delta M$. Figure IV.2 shows the trend of Θ with present DNS data along with other existing data. In wrinkled regime, the data agrees with the theories in Donzis (2012b) very well. As $M_t/\Delta M$ increases, however, departures are apparent with two interesting features. First we see that, in spite of significant scatter, Θ seems to approach an asymptotic state at high $M_t/\Delta M$ with a value dependent on the Reynolds number. We call this value Θ_∞ . Second, DNS data departs from the QE prediction at higher $M_t/\Delta M$ when R_λ is higher. This effect does not appear to be due to the increase of holes in the shock since figure III.3 shows that the fraction of subsonic regions does not depend on R_λ . A potential explanation for this effect, then, is that at low Reynolds numbers, the stronger viscous effects can enhance transverse diffusion of momentum which would make the 1D local behavior assumption, and thus QE, less applicable. However, these observations require more data at a range of parameters to quantify the departures from the QE prediction and assess the origin of the change in value of $M_t/\Delta M$ with R_λ at which QE predictions deteriorate.

IV.B A New Regime: Vanished Shocks

Before we discuss the asymptotic value Θ_∞ , it is instructive to see the structure of the flow, in particular dilatation, as it crosses the shock. In figure IV.3 we show, for three different cases, plane-averaged dilatation along the streamwise direction (dark line) with a set of instantaneous dilatation profiles at some arbitrary locations (light gray lines). In part (a) of the figure we see a wrinkled case (though close to broken limit) with a very strong mean dilatation comprised of similar instantaneous

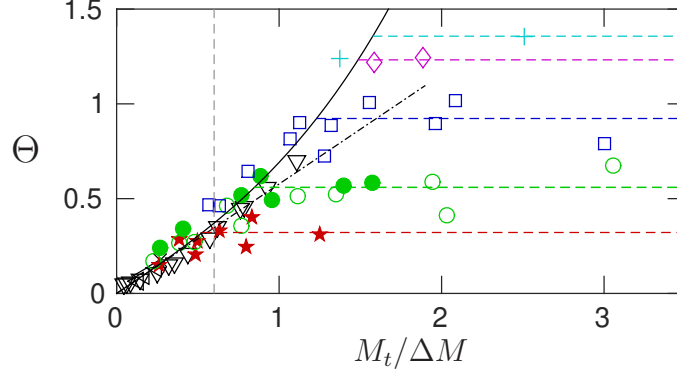


Figure IV.2: Rms-to-mean dilatation at the shock for $R_\lambda \approx 5$ (red stars), $R_\lambda \approx 10$ (green circles), $R_\lambda \approx 25$ (blue squares), $R_\lambda \approx 45$ (magenta diamonds), $R_\lambda \approx 65$ (cyan plusses). Open and closed symbols are for IT and SDT simulations, respectively. Dash-dotted line is Eq. (IV.2) and solid line is best fit with $e_1 = 0.577$ and $e_2 = 0.114$. Vertical gray dashed line at $M_t/\Delta M = 0.6$ for reference. Horizontal dashed lines: average of DNS data at high $M_t/\Delta M$ for $R_\lambda \approx 5, 10, 25, 45$ and 65 from bottom to top. Other symbols: Jamme *et al.* (2002)(\times), Larsson & Lele (2009)(∇) and Boukharfane *et al.* (2018)(\triangleleft).

profiles. At higher $M_t/\Delta M$ in the broken regime (part b) we also see a strong peak of mean dilatation at the shock, though the peak is spatially broader, consistent, as mentioned in previous sections, with theoretical predictions (Donzis, 2012b). Individual dilatation profiles, however, display a wider range of behaviors: some have the same qualitative peak while others present multiple peaks or a very broad smooth variation (Lee *et al.*, 1993; Larsson & Lele, 2009). At even higher values of $M_t/\Delta M$ (part c) individual profiles show very large fluctuations upstream and downstream of the shock comparable to the mean (dark line). It is interesting to note that while fluctuations in this case are of the same order as the mean, the latter still shows the same peak as, though much broader than, in the wrinkled regime.

Broad dilatations with multiple peaks distinguish broken shocks from wrinkled shocks. But a broken shock is still identifiable from a dominant peak standing out

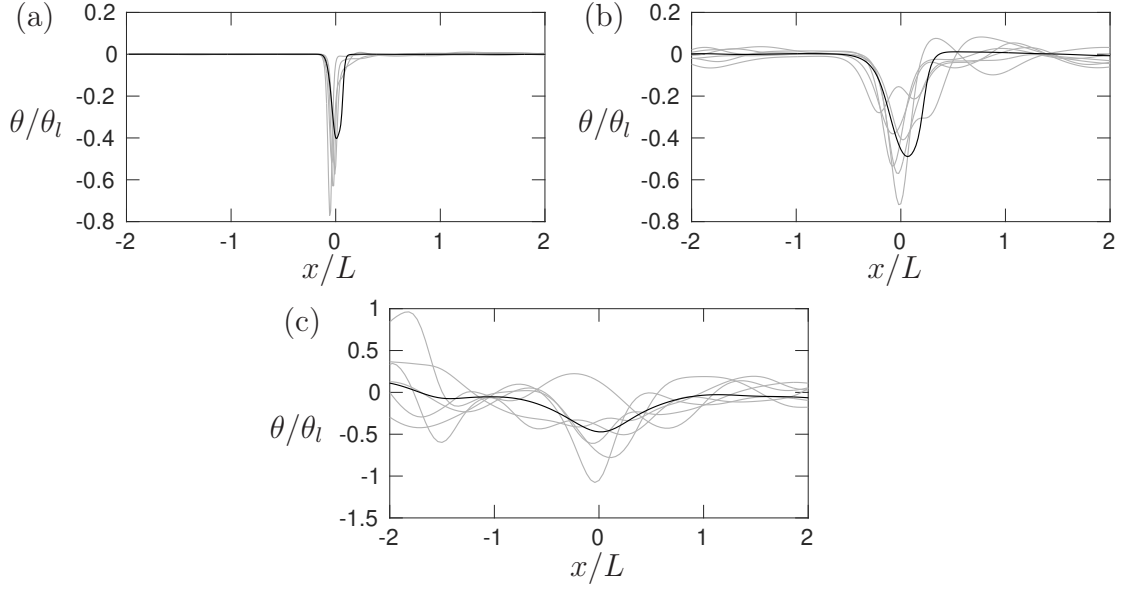


Figure IV.3: Instantaneous dilatation normalized by laminar condition (θ_l) along streamwise direction at different transverse locations (grey) and their mean (black) at $M = 1.1$, $R_\lambda \approx 10$ and (a) $M_t = 0.05$ (wrinkled), (b) $M_t = 0.14$ (broken) and (c) $M_t = 0.34$ (vanished).

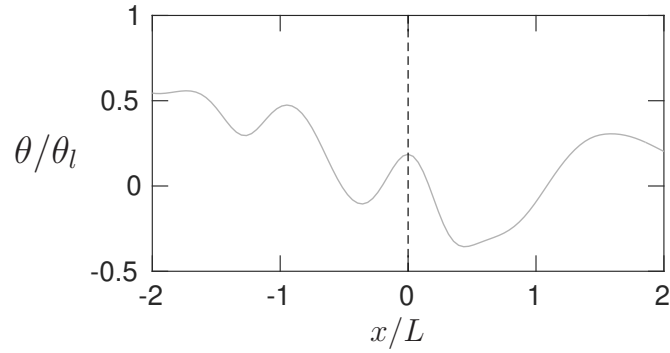


Figure IV.4: One instantaneous dilatation normalized by laminar condition (θ_l) at $M = 1.1$, $R_\lambda \approx 10$, $M_t = 0.34$. The dashed line is the location of the shock from $\min(\partial u / \partial x)$.

from others. At much higher $M_t/\Delta M$, such as shown in figure IV.3(c), several similar peaks are observed in dilatations which results in a challenge of pinpointing the location of shock. Since a shock wave is a phenomenon with very small length scale, accurate measurement of shock location is crucial to analyze its characteristics. A method is implemented in present simulations to obtain minimum dilatation inside the shock. In the beginning, we obtain the location of minimum streamwise velocity gradient at each line along the mean flow direction. This location is considered the shock location which is the dashed line in figure IV.4. As shown in the figure, there are two peaks along a dilatation line and neither of them are fairly close to the shock. To proceed, we choose the dilatation peak closest to the shock as θ_s and apply the same method to θ_s^2 . Overall, this method successfully captures the local dilatations and shows consistent $M_t/\Delta M$ dependence with little scatter. We note that the mislocation between streamwise velocity gradient and dilatation peak in figure IV.4 implies a strong transverse motions which is beyond this work.

Typical distributions of Reynolds stresses and mean pressure are shown in figure IV.5 at similar conditions. In part (a) we see that, consistent with observations in the literature, the downstream peak of R_{11} at x_2 decreases with M_t . As M_t increases further, we observe both the peaks upstream and downstream of the shock (x_1 and x_2 , respectively) vanish. We term this, then, the *vanished* regime. Clearly in this regime, it is not possible to compute amplification factors since no upstream and downstream locations can be identified unambiguously. In fact, Reynolds stresses undergo a classical turbulent decay. It is interesting that mean quantities such as mean pressure (part c) or mean velocity retain the typical qualitative behavior of a shock. While these mean gradients may lead to production by mean shear in the

Reynolds stress budget, because of the short residence time within the shock region, they cannot, on average, counteract the viscous decay.

Furthermore, since in the vanished regime R_{11} experiences a monotonic decay across the nominal shock and no x_1 location can be identified, it is also not possible to determine R_λ , M_t , or ΔM upstream of the shock as in wrinkled or broken cases. Alternatively, one can estimate the conditions for the appearance of the vanished regime by assessing the limit at which local extrema vanishes for R_{11} . For example, for $R_\lambda \approx 5$, 10 and 25, we find that the vanished regime appears at $M_t/\Delta M \approx 2.14$, 3.4 and 4.4, respectively. In these three cases, K is found to be very close to 1.0. This is, in fact, not unexpected. As we show below, the amplification factor for R_{11} shows a universal behavior with K for relatively high K . In particular, it decreases with K and reach values around 0.8 at $K \approx 1$. Beyond this value of K no local extrema are observed and amplification factors cannot be obtained.

A plausible explanation for the emergence of the vanished regime is that dissipative effects are stronger than production mechanisms. If transport terms as well as pressure effects in the budget equation for R_{11} are not taken into account, the condition for shocks in the vanished regime would be $\epsilon/\mathcal{P} \gtrsim 1$. We have indeed verified that vanished shocks are observed if and only if $\epsilon/\mathcal{P} \geq 1.5$. This supports the idea that a larger dissipation than required for equilibrium is responsible for the disappearance of the local extrema for R_{11} .

It is naturally of interest to determine whether this condition is met from the governing parameters. Using classical scaling relations we can estimate the dissipation at the shock as $\epsilon \sim \nu R_{11}/\lambda^2$ and production as $\mathcal{P} \sim R_{11}[u]/\delta$. This ratio can

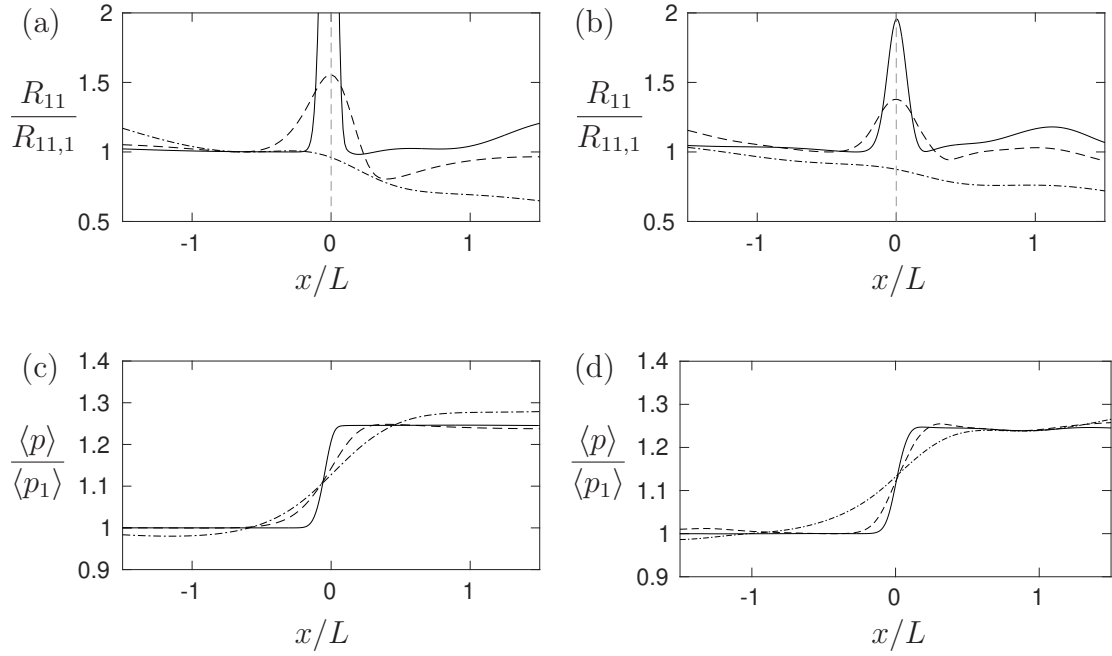


Figure IV.5: Distributions of R_{11} at $M = 1.1$, (a) $R_\lambda \approx 10$ and $M_t = 0.05$ (solid), $M_t = 0.14$ (dashed) and $M_t = 0.34$ (dash-dotted) and (b) $R_\lambda \approx 25$ and $M_t = 0.22$ (solid), $M_t = 0.3$ (dashed) and $M_t = 0.44$ (dash-dotted). Distribution of p at, (c) $R_\lambda \approx 10$ and $M_t = 0.05$ (solid), $M_t = 0.14$ (dashed) and $M_t = 0.34$ (dash-dotted), and (d) $R_\lambda \approx 25$ and $M_t = 0.14$ (solid), $M_t = 0.22$ (dashed) and $M_t = 0.44$ (dash-dotted). The vertical dashed lines are the shock location based on $\min(\partial\langle u \rangle / \partial x)$.

be, after some manipulation be written as

$$\left. \frac{\epsilon}{\mathcal{P}} \right|_{shock} \sim \left. \frac{M_t}{R_\lambda^{3/2}} \right|_{shock} \left. \frac{KM}{M^2 - 1} \right|_{x_1}. \quad (\text{IV.3})$$

which contains both upstream conditions as well as those inside the shock. While preliminary results suggest that this expression can indeed predict the ratio approximately, more work is needed to relate all the quantities involved to upstream conditions exclusively. This is part of future work.

IV.C Rms-to-mean Dilatation Beyond Wrinkled Shocks

We now move back to the asymptotic value Θ_∞ . As $M_t/\Delta M$ increases, increasingly large areas of the shock are subsonic and present holes. However, it is unclear what the value of θ_s is across holes. Furthermore, as turbulence becomes more intense, the flow will experience stronger locally three-dimensional effects which will favor strong mixing in all directions and thus weaken the applicability of QE. According to the definition of Θ one searches for the largest negative dilatation around the location of the shock along x for a given (y, z) location. When turbulence is strong, however, while the mean dilatation $\langle \theta \rangle$ still shows a typical behavior (negligible values far from the shock and a negative peak at the shock), the behavior at different (y, z) locations is very different. This is clear as one compares the three panels in figure IV.3. In the limit of very intense turbulence, one would expect Θ to be essentially dominated by turbulence statistics.

Thus, we will estimate the asymptotic behavior of Θ as one in which turbulence dominates the averages. In this case we can use known scaling laws for velocity gradients. However, Θ is based on the average of the *minimum* dilatation close to

the average location of the shock. Note that while the mean dilatation in isotropic turbulence is zero, the average of minimum dilatation across an arbitrary plane is not. Thus, here we make the additional assumption that these values are, to first approximation, proportional to the average magnitude of those gradients. Moments of velocity gradients are known to scale as power laws with the Reynolds number (Monin & Yaglom, 1975b) which can be written as $\langle |\partial u / \partial x|^n \rangle = C_n (u_{1,rms}/L)^n R_\lambda^{2\rho_n}$ where C_n are flow-dependent constants and ρ_n are the so-called scaling exponents. While these power laws have been historically believed to hold only for high Reynolds numbers, recent work suggests that their applicability extends to rather low Reynolds numbers (Schumacher *et al.*, 2007, 2014; Yakhot & Donzis, 2017) and thus expected to apply, at least approximately, to our present conditions. We then estimate Θ_∞ , when turbulence dominates, as

$$\Theta_\infty \approx \left(\frac{\langle |\partial u / \partial x|^2 \rangle}{\langle |\partial u / \partial x| \rangle^2} - 1 \right)^{1/2} \approx c_1 \left(c_2 R_\lambda^{2(b_2 - 2b_1)} - 1 \right)^{1/2}, \quad (\text{IV.4})$$

where all order-unity prefactors have been absorbed in the constants c_1 and c_2 . The exponents have been studied extensively and are relatively well known (e.g., Schumacher *et al.*, 2007; Yakhot & Donzis, 2018) with values $b_2 = 1$ and $b_1 = 0.46$.

In figure IV.6 we show Θ_∞ from DNS along with Eq. (IV.4) with $c_1 = 1.756$ and $c_2 = 0.8217$ obtained as best-fit coefficient indeed of order-unity. The good agreement between theory and DNS data supports the idea of Θ being dominated by turbulence rather than the shock at those conditions. At the same time from figure III.3 we see that even for $M_t/\Delta M \approx 3$ the subsonic regions are only about 30% of the total shock area. Thus, the dominance of turbulence appears to stem

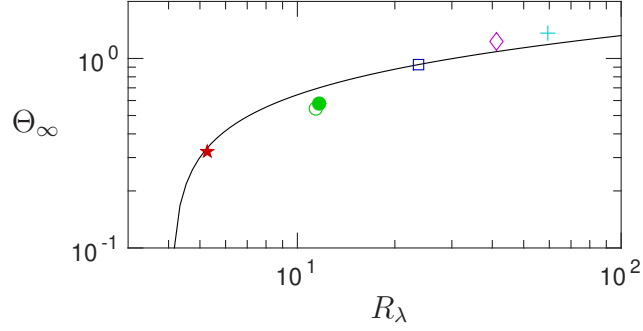


Figure IV.6: Asymptotic value of Θ as a function of R_λ . Different symbols represent the average of DNS data at a fixed R_λ in the asymptotic state (see text). Symbols as in figure IV.2. Solid line is Eq. (IV.4) with $c_1 = 1.756$ and $c_2 = 0.8217$.

from strong turbulent mixing across and after the weak shock.

IV.D Truncated Integrals on Dilatation

With the successful implementation of truncated integrals on turbulent shock jumps, one would expect that the same method also applies to shock structure. If truncated integrals using classical theories from turbulence and shock waves can capture Θ , we can present Θ as a function of flow conditions. Such function can reveal the mechanisms that dominate the shock waves transitioning between different regimes. However, several attempts trying to repeat the same implementation from shock jumps have failed to provide accurate prediction of Θ beyond wrinkled regime. The failure comes from the discrepancies between the DNS data and the solutions at high $M_t/\Delta M$. Here, we will show the main two methods that we have tried before.

Similar to the steps of deriving turbulent shock jumps, the dilatation on the shock front comprises two parts, supersonic and subsonic flows. In the supersonic regions,

Taylor's weak shock theory indicates that

$$\theta_s^> \sim k_1[u] \frac{\rho^c}{\mu} (\Delta M + m). \quad (\text{IV.5})$$

For the subsonic regions, though the exact function of the θ at subsonic regions is unclear, we assume it is linearly correlated to the first moment in the supersonic regions as

$$\theta^< = \alpha_\theta \langle \theta_s \rangle^> \quad (\text{IV.6})$$

by a coefficient α_θ where $\langle \theta_s \rangle^>$ is the averaged first moment of dilatation in the supersonic regions. By combining Eq. (IV.5) and Eq. (IV.6) and taking integral against the p.d.f. of m , the first moment of dilatation is given by

$$\begin{aligned} \langle \theta_s \rangle_s &= \int_{-\Delta M}^{\infty} k_1[u] \frac{\rho^c}{\mu} (\Delta M + m) f_m(m) dm + \alpha_\theta \langle \theta_s \rangle_s^> \int_{-\infty}^{-\Delta M} f_m(m) dm \\ &= k_1[u] \left(\frac{\rho^c}{\mu} \right) (\Delta M \langle m^0 \rangle^> + \langle m \rangle^>) (1 + \alpha_{\theta_s} \langle m^0 \rangle^<). \end{aligned} \quad (\text{IV.7})$$

Similar to the first moment, the second moment of dilatation can be given as

$$\begin{aligned} \langle \theta_s^2 \rangle_s &= \int_{-\Delta M}^{\infty} (k_1[u] \frac{\rho^c}{\mu})^2 (\Delta M + m)^2 f_m(m) dm + \beta_\theta \langle \theta_s \rangle_s^> \int_{-\infty}^{-\Delta M} f_m(m) dm \\ &= (k_1[u] \frac{\rho^c}{\mu})^2 (\Delta M^2 \langle m^0 \rangle^> + 2\Delta M \langle m \rangle^> + \langle m^2 \rangle^>) (1 + \beta_\theta \langle m^0 \rangle^<). \end{aligned} \quad (\text{IV.8})$$

By substituting Eq. (IV.7) and Eq. (IV.8) into Eq. (IV.1), we can obtain

$$\Theta = \left[\frac{(\Delta M^2 \langle m^0 \rangle^> + 2\Delta M \langle m \rangle^> + \langle m^2 \rangle^>) (1 + \beta_\theta \langle m^0 \rangle^<)}{(\Delta M \langle m^0 \rangle^> + \langle m \rangle^>)^2 (1 + \alpha_{\theta_s} \langle m^0 \rangle^<)^2} - 1 \right]^{\frac{1}{2}}. \quad (\text{IV.9})$$

Though the equation of rms-to-mean dilatation becomes much more complicated with truncated integrals, Eq. (IV.9) shows that Θ is still a function of $M_t/\Delta M$.

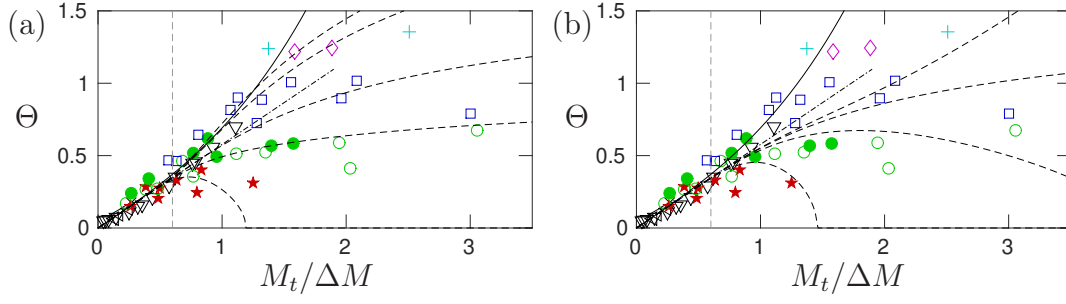


Figure IV.7: Rms-to-mean dilatation at the shock with (a) linear correlation between and the supersonic and subsonic regions with $\alpha_\theta = (2.5, 0.6, 0.05, 0.01, 0)$ and $\beta_\theta = (0.01, 0.025, 0.5, 3, 4)$ and (b) dissipative anomaly for the subsonic regions with $\alpha_\theta = (5, 2, 0.05, 0)$ and $\beta_\theta = (0.01, 0.1, 1.5, 10000)$. Same colors and symbols as in figure IV.2.

Since viscous effects modifies the dilatation profile, the R_λ dependence discussed previously should reflect on the values of α_θ and β_θ . Figure IV.7(a) shows the prediction of Eq. (IV.9) with different α_θ and β_θ . Though Eq. (IV.9) captures Θ at low $M_t/\Delta M$, large quantitative difference appears when the shock becomes broken. In addition, the asymptotic states from DNS data are not predicted by Eq. (IV.9). Instead, the theoretical solutions from linear correlation suggests the values of rms-to-mean dilatation would continue growing with $M_t/\Delta M$. The discrepancies between the analytical prediction and the simulations implies that when a shock becomes broken there exists a strong non-linear effect between supersonic and subsonic regions. Therefore, a simple linear correlation between the dilatations at supersonic and subsonic regions cannot accurately predict Θ .

An alternative for the linear correlation is dissipative anomaly. Dissipative anomaly suggests that dissipation, ϵ , would eventually be independent of R_λ at very high R_λ and proportional to time derivative of turbulent kinetic energy, \mathcal{K} . Figure IV.8 shows the estimate of R_λ dependence compared to DNS data at x_1 (Donzis *et al.*, 2005).

The R_λ scaling is accurately predicted over a wide range of conditions with little scatter of SDT cases. Such good agreement suggests that dissipative anomaly may be a good approach to study the change of dilatation. If QE is valid, we can assume that $d\mathcal{K}/dt \approx du_1'^2/dt$, which is equal to $u_1'^3/L_{11}$ where \mathcal{K} is the turbulent kinetic energy and L_{11} is the longitudinal integral length scale. On the other hand, in isotropic turbulence a good approximation for instantaneous dissipation is $\epsilon = 15\nu\theta_s^2$. Therefore, we can obtain an expression for the second order moment in subsonic regions as

$$\theta^{2<} = f R_L \frac{u'^2}{L^2} \quad (\text{IV.10})$$

where f is a function from dissipative anomaly (Donzis *et al.*, 2005) and R_L is the Reynolds number at dissipation scale. To obtain a similar form like $\langle\theta_s\rangle_s$, the second order moment is rearranged as

$$\theta^{2<} = f \left[k_1[u] \left(\frac{\rho c}{\mu} \right) \right]^2 \frac{R_L}{k_1^2[u]^2} \frac{\mu^2 u^2}{\rho^2 c^2 L^2}. \quad (\text{IV.11})$$

For a weak laminar shock, velocity change can be approximated as $[u] \approx c\Delta M$ (Thompson, 1984). Also, by turbulence scaling we have $R_L \approx R_\lambda^2$. Finally, the second order moment of dilatation at the holes is expressed as

$$\theta^{2<} = f \left[k_1[u] \left(\frac{\rho c}{\mu} \right) \right]^2 \frac{M_t^4}{k_1^2 R_\lambda^2 \Delta M^2}. \quad (\text{IV.12})$$

Again, using truncated integrals to include both the weak shock theory and dissipa-

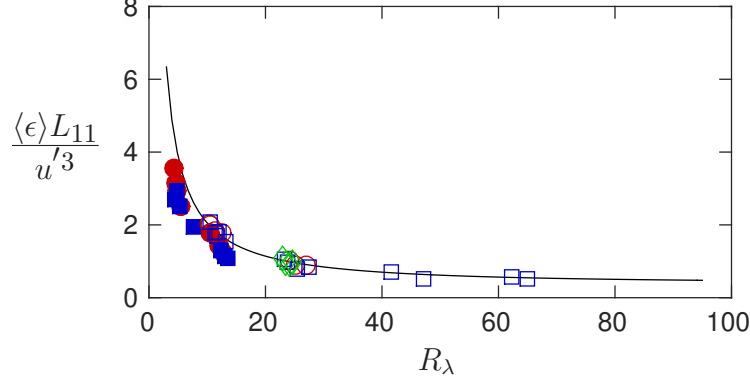


Figure IV.8: Normalized dissipation rate from Donzis *et al.* (2005) (solid) and present simulations at x_1 . Red circles correspond to $M = 1.1$, blue squares to $M = 1.2$ and green diamonds to $M = 1.4$. Open and closed symbols are for IT and SDT simulations, respectively.

tive anomaly, the first and the second moment of dilatation are expressed as

$$\begin{aligned} \langle \theta_s \rangle_s &= \left[k_1 [u] \frac{\rho c}{\mu} \right] \left[\int_{-\Delta M}^{\infty} (\Delta M + m) f_m(m) dm + \alpha_\theta f^{\frac{1}{2}} \frac{M_t^2}{k_1 R_\lambda \Delta M} \int_{-\infty}^{-\Delta M} f_m(m) dm \right] \\ &= \left[k_1 [u] \frac{\rho c}{\mu} \right] \left[\Delta M \langle m^0 \rangle^> + \langle m^0 \rangle^> + \alpha_\theta f^{\frac{1}{2}} \frac{M_t^2}{k_1 R_\lambda \Delta M} \langle m^0 \rangle^< \right] \end{aligned} \quad (\text{IV.13})$$

and

$$\begin{aligned} \langle \theta_s^2 \rangle_s &= \left[k_1 [u] \frac{\rho c}{\mu} \right]^2 \left[\int_{-\Delta M}^{\infty} (\Delta M + m)^2 f_m(m) dm + \beta_\theta f \frac{M_t^4}{k_1^2 R_\lambda^2 \Delta M^2} \int_{-\infty}^{-\Delta M} f_m(m) dm \right] \\ &= \left[k_1 [u] \frac{\rho c}{\mu} \right]^2 \left[\Delta M^2 \langle m^0 \rangle^> + 2\Delta M \langle m \rangle^> + \langle m^2 \rangle^> + \beta_\theta f \frac{M_t^4}{k_1^2 R_\lambda^2 \Delta M^2} \langle m^0 \rangle^< \right] \end{aligned} \quad (\text{IV.14})$$

where α_θ and β_θ are coefficients for best fitting of DNS data.

By substituting Eq. (IV.13) and Eq. (IV.14) into Eq. (IV.1), we can obtain rms-to-mean dilatation from weak shock theory and dissipative anomaly as

$$\Theta = \left[\frac{\Delta M^2 \langle m^0 \rangle^> + 2\Delta M \langle m \rangle^> + \langle m^2 \rangle^> + \beta_\theta f \frac{M_t^4}{k_1^2 R_\lambda^2 \Delta M^2} \langle m^0 \rangle^<}{\left(\Delta M \langle m^0 \rangle^> + \langle m^0 \rangle^> + \alpha_\theta f^{\frac{1}{2}} \frac{M_t^2}{k_1 R_\lambda \Delta M} \langle m^0 \rangle^< \right)^2} - 1 \right]^{\frac{1}{2}}. \quad (\text{IV.15})$$

One main difference between the form from dissipative anomaly and the linear correlation is that Θ obtained from dissipative anomaly shows a dependence on R_λ . This seems to imply that dissipative anomaly can better capture the trend of dilatation in subsonic regions. However, figure IV.7(b) still shows a big discrepancy between Eq. (IV.15) and DNS data beyond wrinkled regime regardless the values of α_θ and β_θ .

The use of dissipative anomaly on predicting Θ relies on a classical theory of dissipation, $\epsilon = 15\nu\theta_s$. This equation only works for isotropic turbulence. Anisotropic turbulence should result in a different coefficient whose value depends on the level of anisotropy. In the following section §V.A, we will show that turbulence inside the shock is significantly anisotropic. Under such circumstances, the accuracy of predicting dilatation is compromised. In addition, dissipation given in classical theory is obtained from the averaged velocity gradient rather than the average of maximum gradients which is what has been applied in Θ . Such little difference may lead to a considerable difference. To accurately capture the trend of Θ , one needs to pinpoint the local shock dilatation rather than obtain the dilatation from an averaged manner. Our studies clearly show that this concern in averaging methods cannot be fixed by changing the coefficients, α_θ and β_θ . Further investigation is required to obtain a proper expression of dilatation in subsonic regions.

IV.E Summary

A very good agreement between DNS data and weak shock theory is obtained from the rms-to-mean dilatation in wrinkled regime. For broken shocks, Θ tends to approaches to a asymptotic state that is dependent on R_λ . These asymptotic states

are successfully captured by classical results of velocity gradients. Gaussian distribution of Mach number fluctuations suggest that the probability of holes on shock is subjected to Mach numbers only. The observed dependence on R_λ at asymptotic states indicates a strong transverse diffusion in the shock. Wrinkled and broken regimes are the two traditional categories for shock waves in turbulent flows. In broken regime, smooth distribution of dilatation with multiple peaks distinguishes the shocks from wrinkled regime. But local shock wave is still easily identifiable from one dominant peak stands out from others. With increasing $M_t/\Delta M$, it becomes difficult to identify the shock when multiple similar peaks appears in dilatation profiles. Accompany with this is a monotonic decay in R_{11} across the shock without any peaks in its evolution. These unprecedented phenomena are proposed as vanished shock. Such behaviors in dilatation and R_{11} are observed universally at $K \approx 1$ which is the condition attributed to the criterion of vanished regime. Further investigations are required to understand the mechanisms resulting in vanished shocks.

V. TURBULENCE AMPLIFICATION

As we have shown, turbulent flows can significantly affect jumps in thermodynamic variables as well as statistical features of the shock structure. Simultaneously, the occurrence of a shock also affects the characteristics of turbulent flows. As the flow passes through a stationary shock, the shock compression triggers turbulent production which further leads to complicated developments of pressure work, viscous dissipation and turbulent transport. In general, most turbulent quantities are increased after the mean flow leaves the shock, except length scales. This turbulence amplification has become a major topic in STI.

A good understanding of turbulence amplification provides essential information of the postshock flows. In a supersonic or hypersonic flight, a shock wave is generated at the front of an airfoil, followed by a boundary layer along the wing. A good example is given in Figure V.1 in which a wave rider is presented in a hypersonic flow tested inside a wind tunnel. As shown in the figure, there are two evident Mach lines far away from the wave rider with boundary layers developed very close to the surface. Though many boundary layer theories provide accurate predictions of the flows, these theories do not applied to the leading edge in general. To further improve the performance of airfoils, one need know the flow conditions of the leading edge. This depends on the studies of how turbulence is modified by the shock. Detailed discussion of the amplification factors is given here.

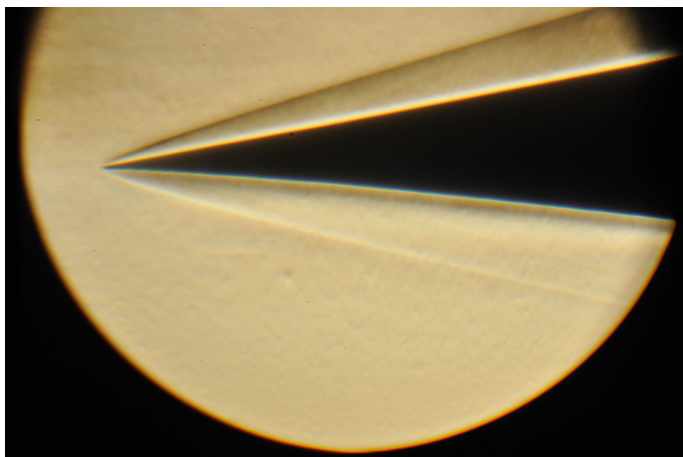


Figure V.1: A wave rider in hypersonic flight with $M = 6$. Visible Mach lines and boundary layers are shown. Courtesy of Prof. Bowersox.

V.A Reynolds Stresses

Velocity fluctuations are very straightforward indicators of turbulent conditions. How Reynolds stresses are modified as the flow passes through a shock has been widely studied (Ribner, 1954*b*; Agui *et al.*, 2005). In particular, it has been found that velocity fluctuations are amplified across the shock.

The distributions of R_{11} with different M_t are shown in Figure V.2(a). As discussed in §II.D, a monotonic viscous decay is observed upstream of x_1 and downstream of x_2 . These two regions are dominated by turbulence processes. The figure also shows that different M_t result in different peaks suggesting a dependence on turbulent conditions. As discussed in §IV, shock holes appear as we increase M_t for fixed M . The occurrence of holes results in a classical turbulent decay as the flow passes through shock region. In this case, the local turbulence loses energy to internal energy without being amplified. Therefore, increasing turbulent intensity leads

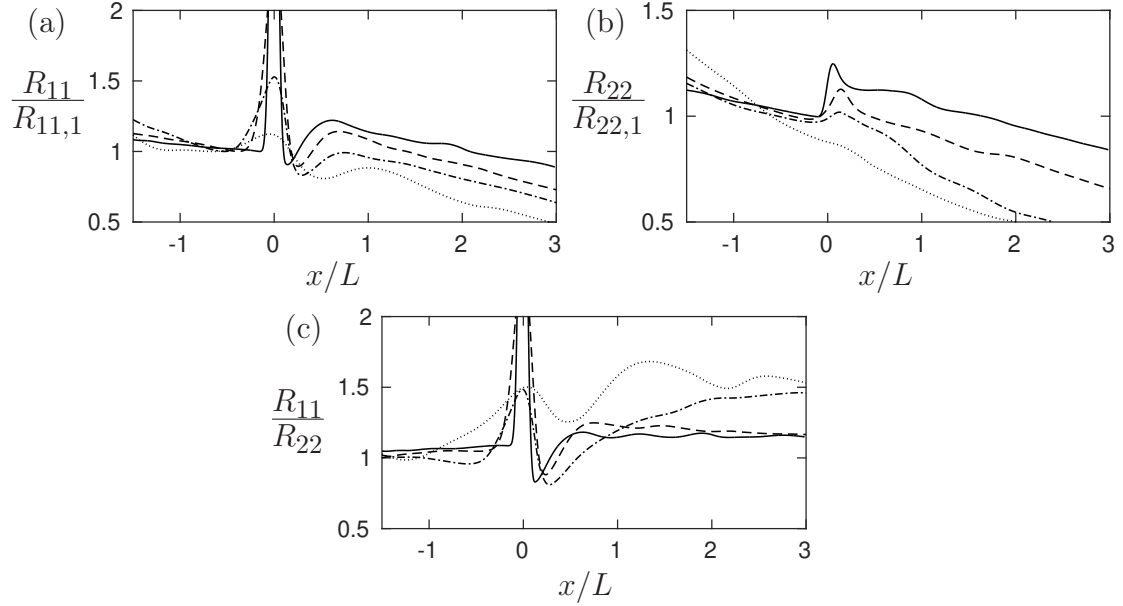


Figure V.2: Normalized distribution of (a) R_{11} , (b) R_{22} and (c) R_{11}/R_{22} with $M = 1.2$, $R_\lambda \approx 25$ and $M_t = 0.12$ (solid), 0.21 (dashed), 0.32 (dash-dotted) and 0.44 (dotted).

to smaller turbulent amplification and possibly attenuation. Figure V.2(b) shows the R_{22} distributions under the same conditions. Relative to R_{11} , R_{22} has a much smaller peak inside the shock and the postshock peak disappears. For a plane shock wave normal to the streamwise direction, the turbulent production only contributes to the streamwise stress. The transverse components would later receive the energy through energy redistribution. As the amplification of R_{11} decreases with M_t , the energy that R_{22} receives also decreases. To further understand how energy is transferred between components, we present anisotropy distributions in figure V.2(c) via the ratio of R_{11} and R_{22} . The figure shows that the flow is isotropic before the shock but becomes highly anisotropic after shock compression. Such anisotropy persists in the postshock evolution and the flow does not return to isotropy for the length of the

simulation domain. Similar postshock anisotropy has also been reported by other investigations (Larsson & Lele, 2009; Larsson *et al.*, 2013; Ryu & Livescu, 2014) with similar values, 1.2 – 1.5. Larsson *et al.* (2013) shows that the postshock anisotropy from DNS is significantly higher than from LIA. This implies that the generation of anisotropic turbulence comes from non-linear processes. Overall, amplification of Reynolds stresses is most evident in the streamwise component due to shock compression. Therefore, the discussion that follows of amplification factors will focus on the change of R_{11} .

A useful quantity to characterize the changes of velocity fluctuations is the so-called amplification factor, $G \equiv R_{11,2}/R_{11,1}$ where subscript 1 and 2 stand for upstream and downstream of the shock as defined previously. Note that in the inviscid laminar case flow variables remain constant downstream of the shock. Therefore, downstream values can be measured in principle anywhere downstream of the shock. In turbulent flows, however, this is not the case due to energy exchanges of both inviscid and viscous nature. Thus, comparison between DNS data and inviscid theories such as LIA requires the identification of a specific location downstream of the shock. It is common to take x_2 (figure II.3a) as this location (Donzis 2012*a* and references therein; Ryu & Livescu 2014; Boukharfane *et al.* 2018). The main rationale behind selecting this location is that, as discussed in §II.D, the flow undergoes a viscous decay beyond that location at which inviscid assumptions are less justified. Locations upstream from this point may be only weakly affected by viscous effects. Here we will follow this convention and use x_2 . We note, however, that other methods have also been examined (e.g. Larsson & Lele, 2009, where Reynolds stresses were extrapolated to the average shock location).

Substantial work has been devoted to test LIA (Lee *et al.*, 1993; Mahesh *et al.*, 1997; Lee *et al.*, 1997; Agui *et al.*, 2005; Larsson & Lele, 2009; Larsson *et al.*, 2013; Ryu & Livescu, 2014; Quadros *et al.*, 2016a). A general observation from all these studies is that LIA becomes more applicable as the flow parameters approach the appropriate conditions, that is when the shock can be approximated as a discontinuity and when the incoming flow is at low M_t and high R_λ . However, when data available in the literature is examined collectively, it is clear that there are both turbulent Mach number as well as Reynolds number effects (Andreopoulos *et al.*, 2000; Donzis, 2012a). To account for this, in Donzis (2012a) we proposed an alternative parameter to characterize the interaction (K) defined as the ratio of the shock thickness to the Kolmogorov length scales, $K \equiv \delta_l/\eta$ where δ_l is the laminar shock thickness at the mean Mach number, M . As K decreases, the shock becomes increasingly smaller relative to turbulence scales. One would, then, expect the interaction to approach the conditions in which LIA is applicable, that is when the shock is a discontinuity interacting with very weak turbulence (low M_t and high R_λ). Indeed, recent well-resolved simulations (Ryu & Livescu, 2014) support this limiting expectation. Our interest here, however, is in the case of finite M_t and R_λ where both parameters play a role. Using classical scaling arguments, one can also write $K = M_t/R_\lambda^{1/2}\Delta M$ (Donzis, 2012a), an expression that was also used in other contexts to assess resolution in DNS (Moin & Mahesh, 1998).

Figure V.3 shows the amplification factor G for all the DNS database presented here (in color) along with all amplification factors available in the literature. In part (a) of the figure, we show G as a function of ΔM , the only parameter that controls the interaction within the LIA theory. (Details on LIA are provided in the Appendix

§A.) Wide differences are seen between the LIA prediction (solid line) and data. As pointed out before (Donzis, 2012*a*) these departures are systematic in R_λ and M_t but disappear when data are plotted against K . This is shown in figure V.3(b) from which we see a high degree of collapse of the new and earlier data onto a single curve at high K which is well represented by a power law of the form $G \approx 0.75K^{-1/4}$ proposed in Donzis (2012*a*). As pointed out above, as $K \rightarrow 0$, one expects to recover conditions in which LIA applies. Ryu & Livescu (2014), using well-resolved DNS data, indeed observed this trend. Thus, data suggest a universal behavior of amplification factors K , with a Mach-number-dependent asymptotic state as $K \rightarrow 0$. At high K , the amplification factor is seen to go below unity, a possibility suggested before (Donzis, 2012*a*), which represent turbulence attenuation as it crosses the shock. Beyond $K \approx 1.0$, amplification factors cannot be defined as the extrema at x_1 and x_2 vanish, marking the beginning of the vanished regime.

This transition between scaling laws based on different non-dimensional groups in particular limits is indeed observed in diverse physical phenomena from equations of states near the critical point (Widom, 1965) to flows in rough pipes (Goldenfeld, 2006). In the latter, Goldenfeld studied the transition from the well-known power-law dependence of the friction coefficient on the Reynolds number to a Reynolds-number-independent scaling law on the ratio of roughness to pipe diameter. In such cases, the dependence on two parameters can be cast in terms of a reduced parameter under which data are observed to collapse into a single universal curve. The data in figure V.3(b) is very suggestive of such a behavior with a transition from K to M as $K \rightarrow 0$. Thus we start by considering the general relation $G = f_1(K, \Delta M)$ for some unknown function f_1 and its observed limiting behavior. At high values of K we

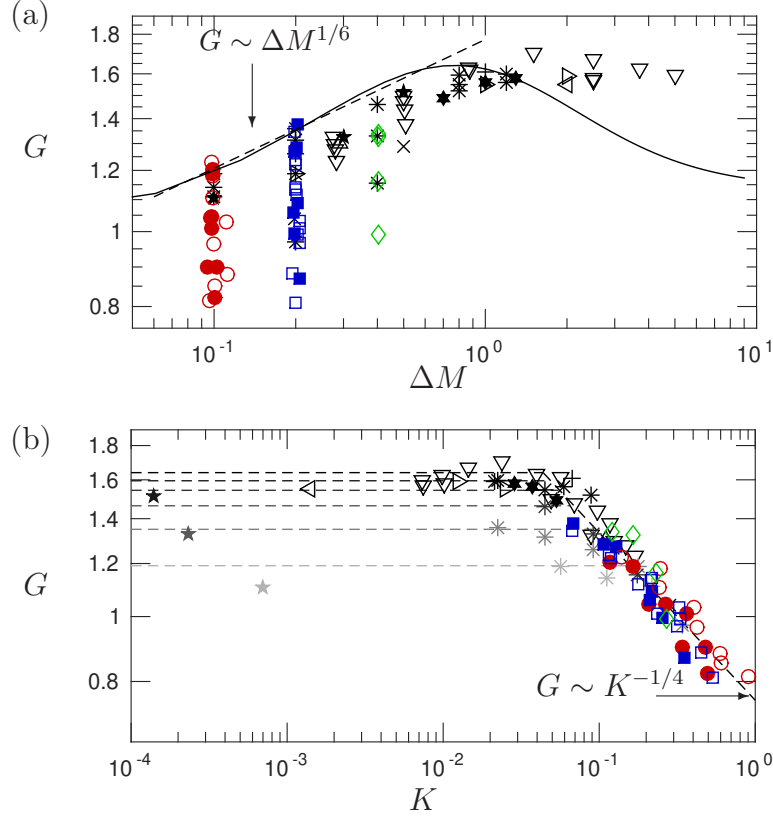


Figure V.3: (a) Collection of amplification factors of streamwise velocity as a function of ΔM along with LIA prediction (Ribner, 1954b). (b) Same data as a function of $K = M_t/(R_\lambda^{1/2} \Delta M)$. Horizontal dashed lines: LIA prediction for $M = 1.1, 1.2, 1.3, 1.4, 1.5$ and 1.8 from bottom to top. In both figures red circles correspond to $M = 1.1$, blue squares to $M = 1.2$ and green diamonds to $M = 1.4$. Open and closed symbols are for IT and SDT simulations, respectively. Other symbols: Lee *et al.* (1993, 1997) (\triangleright), Hannappel & Friedrich (1995) ($+$), Barre *et al.* (1996) (\triangleleft), Mahesh *et al.* (1997) (\triangle), Jamme *et al.* (2002) (\times), Larsson & Lele (2009) and Larsson *et al.* (2013) (∇), Ryu & Livescu (2014) ($*$, grey levels for $M = 1.1$, $M = 1.2$ and $M = 1.4$ from light to dark), Boukharfane *et al.* (2018) (\star) and Tanaka *et al.* (2018) (\blackstar , grey levels for $M = 1.1$, $M = 1.3$ and $M = 1.5$ from light to dark).

observe a $K^{-1/4}$ scaling; at low values of K , G tends to LIA. Note that this imposes significant constraints in the functional form for f_1 . For simplicity in the analysis we consider the behavior for $M \lesssim 2$ where the LIA solution can be approximated as a power law of the form $\Delta M^{1/6}$ as shown in figure V.3(a) with a dashed line. Following Widom (1965), we now propose the following scaling relation:

$$G = K^{-1/4} f_2(K^\alpha \Delta M), \quad (\text{V.1})$$

where α is an exponent to be determined by specific limits. Note that this is essentially a case of incomplete similarity also justified from renormalization group theory (Barenblatt, 2003) in which universality is revealed only under a suitable combination of the original governing non-dimensional parameters, though this combination cannot be obtained on dimensional grounds alone. However, consistency with the $\Delta M^{1/6}$ asymptotic behavior requires that $f_2(x) \sim x^{1/6}$ as $x \rightarrow 0$ and, simultaneously, the K dependency must disappear. It is easy to see that G will become independent of K in that limit if $\alpha = 3/2$. The final result is then

$$G = K^{-1/4} f_2(K^{3/2} \Delta M). \quad (\text{V.2})$$

The implication of the scaling proposed in (V.2) is that while the phenomenon depends on the two parameters K and ΔM at two different limiting conditions, a collapse on a universal curve will emerge if one plots $G/K^{-1/4}$ as a function of $K^{2/3} \Delta M$. This is indeed the case as seen in figure V.4 where we show data at $M < 2$, the condition at which the scaling argument applies. We can see that, for example, the

data from Ryu & Livescu (2014) which departs from K scaling at different ΔM (figure V.3b) collapse onto the line with a slope of $1/6$. This low K behavior is readily understood by recalling that $f_2(x) \sim x^{1/6}$ at small x which corresponds to $G \sim \Delta M^{1/6}$. At high K , $G \sim K^{-1/4}$ which under the normalization in the plot is seen as a horizontal line. Given the number and variety of data sources and flow conditions collected here combined with the lack of systematic trends with Reynolds, turbulent and mean Mach numbers individually, the collapse of the data is deemed very satisfactory. This is especially so when one compares with figure V.3(a).

The transition from K -scaling to M -scaling, reminiscent of critical phenomena as noted above, allows us also to determine the combination of parameters at which it occurs. From figure V.4, we observe that this transition happens at $K^{3/2}\Delta M \approx 0.0055$. Explicitly, we can then write

$$K_{tr} \approx \frac{0.03}{\Delta M^{2/3}}. \quad (\text{V.3})$$

which is found to be consistent with the data in figure V.3(b), especially those of Ryu & Livescu (2014) which clearly show the transition. We also point out that (V.3) provides a precise meaning to the distinction between low- K and high- K interactions, a classification that was put forth only in qualitative terms (Donzis, 2012a): amplification factors at $K < K_{tr}$ could be well represented by LIA; amplification factors at $K > K_{tr}$ scale as $G \approx 0.75K^{-1/4}$. From figure V.4 we see that the majority of the data in the literature with $M < 2$ correspond to high- K interactions.

We close this section by noting that the amplification factor shows no systematic difference between the two types of mechanisms used to generate turbulence here,

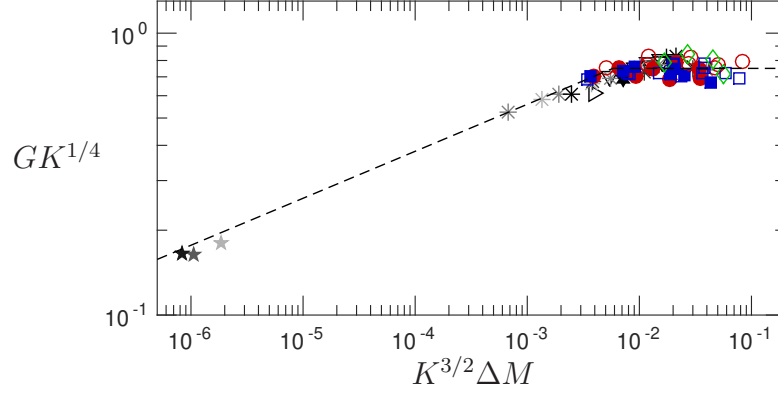


Figure V.4: Universality of amplification factor based on the scaling of (V.2) for data with $M < 2$. Same colors and symbols as in figure V.3.

namely, IT and SDT as described in §II.B. Since the former is statistically isotropic while the latter is not with longitudinal stresses R_{11} up to 64% larger than transverse stresses R_{22} (table II.2), data suggest that amplification of turbulence in the streamwise direction may be dominated by one-dimensional processes in that direction. This is consistent with the discussion in §III.B in which it was argued that the dynamics in the region upstream of x_2' is mainly determined by shock effects in QE. Fully developed turbulence, on the other hand, is attained only at x_2 beyond which well-known return-to-isotropy processes (not accounted for in LIA) are expected to operate at relatively long time scales (Larsson & Lele, 2009; Larsson *et al.*, 2013; Ryu & Livescu, 2014; Livescu & Ryu, 2016). In light of these observations, it may not be entirely surprising the virtually undetectable dependence of G on anisotropy in the incoming turbulence.

V.B Enstrophy

In shock-turbulence interactions, the shock virtually modifies all turbulent properties in the flow. For example, there has been interest in understanding changes

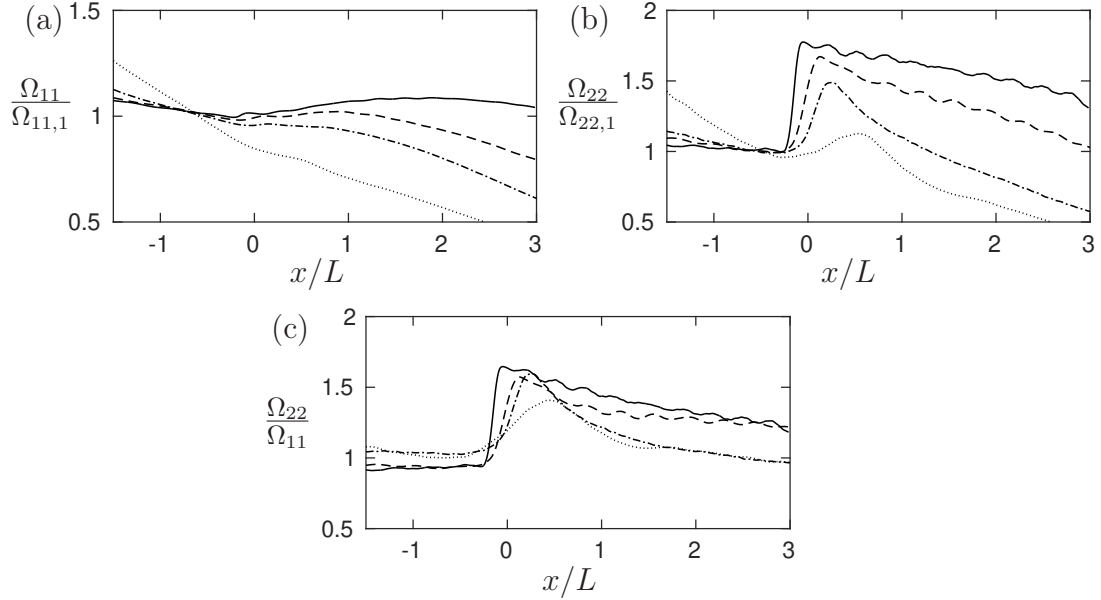


Figure V.5: Normalized distribution of (a) Ω_{11} , (b) Ω_{22} and (c) Ω_{22}/Ω_{11} with $M = 1.2$, $R_\lambda \approx 25$ and $M_t = 0.12$ (solid), 0.21 (dashed), 0.32 (dash-dotted) and 0.44 (dotted).

in vorticity statistics as a result of such interaction (Truesdell, 1952; Andreopoulos *et al.*, 2000). As turbulence goes through a shock, the compression imposed on the Reynolds stresses modifies other turbulent properties accordingly. However, as presented in figure II.4, Ω_{22} shows a totally different distribution from R_{11} indicating there exist different mechanisms that dominate vorticity. As a result, the amplification of enstrophy will be obtained from different locations, $x_{1\Omega_{22}}$ and $x_{2'\Omega_{22}}$, rather than the traditional ones.

The distributions of Ω_{11} and Ω_{22} are given in figure V.5 with different M_t . We can see from part (a) that the streamwise vorticity is barely amplified by the shock. Ω_{22} , on the other hand, shows evident amplifications from shock compression, and such amplification decreases with M_t . Compared to R_{11} , postshock vorticity experiences

a monotonic decay (without a peak). The pressure effects on rII postshock peaks are negligible in Ω_{22} . Another feature in enstrophy is that the postshock evolutions return to isotropy in the far field. So far, the dominant mechanism in enstrophy is still a topic of debate, the theoretical work (Truesdell, 1952) suggested that the baroclinic effect contributes the most, another one (Lee *et al.*, 1993) proposed that vorticity-compression dominates, and Sinha (2012) concluded that both baroclinic effect and vorticity-compression are important. Further investigations with detailed budget studies are needed for understanding the evolution of enstrophy, especially the phenomenon of far-field isotropy. Since Ω_{22} is much more amplified than Ω_{11} , further discussion would focus on the transverse components.

Similar to R_{11} , many efforts are made to understand the amplification of Ω_{22} through LIA. However, the LIA prediction of Ω_{22} has not been systematically compared to DNS data in the literature. In figure V.6(a), we present the amplification of Ω_{22} across the shock from present simulations as well as other data available in the literature, and compare them to LIA (Details on LIA results for enstrophy can be found in Appendix §A.) The figure shows that LIA only captures the trend of trend in the data with low turbulence intensities. At higher intensities, the amplification of Ω_{22} decreases and cannot be accurately quantified by M . As previously discussed, K scaling has successfully characterized the trend of R_{11} under strong turbulence at which discrepancy appear between LIA and DNS. Such method is also applied to Ω_{22} , the amplification is presented against K in figure V.6(b). The figure shows a power law of $G_{\Omega_{22}}$ at high K , specifically $G_{\Omega_{22}} \approx 0.75K^{-0.75}$. Compared to the power law of R_{11} , the exponent coefficient of $G_{\Omega_{22}}$ is larger indicating that Ω_{22} is more sensitive to the interactions. At low K by which shock wave dominates, the

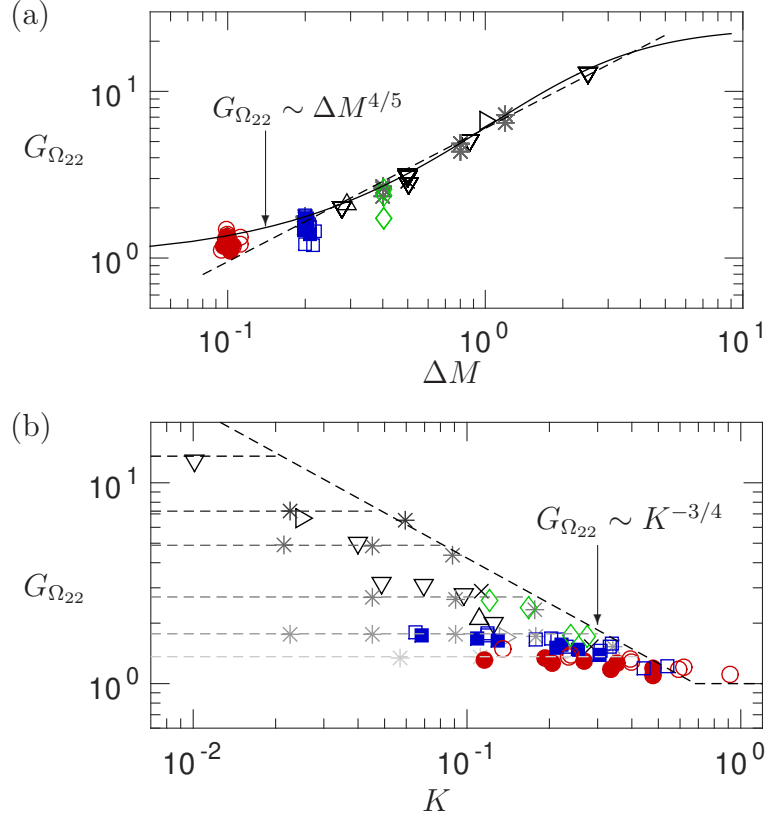


Figure V.6: (a) Collection of amplification factors of transverse vorticity as a function of ΔM along with LIA prediction (Ribner, 1954b). (b) Same data as a function of $K = M_t/(R_\lambda^{1/2}\Delta M)$. Horizontal dashed lines: LIA prediction for $M = 1.1, 1.2, 1.4, 1.8, 2.2$ and 3.5 from bottom to top. Same colors and symbols as in figure V.3.

change of enstrophy shows a clear M dependence which is predicted by LIA. The horizontal dashed lines in figure V.6(a) are the estimates from LIA (Wouchuk *et al.*, 2009) which seem to be the asymptotic states for $G_{\Omega_{22}}$ as $M \rightarrow 0$.

In figure figure V.6, $G_{\Omega_{22}}$ shows a transition of two scaling laws, M and K , just like R_{11} . Similar work is carried out to obtain an universal scaling. Thus, we start by again considering $G_{\Omega_{22}} = f_3(K, \Delta M)$ with an unknown function f_3 . At high K we observe $G_{\Omega_{22}} \sim K^{-0.75}$ while $G_{\Omega_{22}}$ approaches to LIA at low K . As shown in figure V.6(a), an good approoximation of LIA is found, $G_{\Omega_{22}} \sim \Delta M^{4/5}$, at a range of $1.2 \lesssim M \lesssim 3.5$. Therefore, the analysis of universal scaling focuses on the DNS data within this range. By repeating the same method in §V.A, we can obtain an universal scaling for $G_{\Omega_{22}}$ as

$$G_{\Omega_{22}} = K^{-3/4} f_4(K^{15/16} \Delta M) \quad (\text{V.4})$$

where f_4 is an unknown function of $K^{15/16} \Delta M$.

Eq. (V.4) suggests an universal scaling between $G_{\Omega_{22}} K^{3/4}$ and $K^{15/16} \Delta M$. Such scaling law is presented in figure V.7. A very good collapse of $G_{\Omega_{22}}$ is obtained through the new scaling at a wide range of K . The transition of $G_{\Omega_{22}}$ from K -scaling to M -scaling allows us to identify the change of dominant mechanism. From figure V.7, such transition occurs at $K^{15/16} \Delta M \approx 0.07$, and therefore, transitional K is given as

$$K_{\Omega, tr} \approx \frac{0.0586}{\Delta M^{15/16}}. \quad (\text{V.5})$$

The transitional condition proposed here is consistent with the data in figure V.6(b).

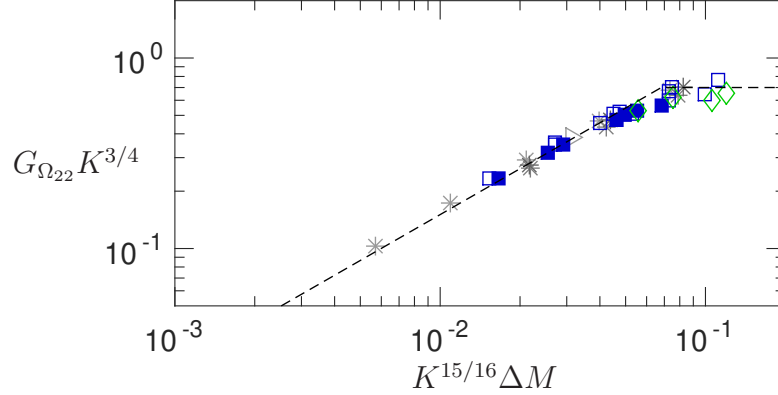


Figure V.7: Universality of amplification of transverse enstrophy based on the scaling of (V.4) for data with $M > 1.1$. Same colors and symbols as in figure V.3.

For $K < K_{\Omega, tr}$, the trend of $G_{\Omega_{22}}$ can be well-captured by LIA while $G_{\Omega_{22}} \sim K^{-3/4}$ at $K > K_{\Omega, tr}$.

In this section, we have compared $G_{\Omega_{22}}$ from DNS and LIA. A systematic trend of R_λ and M_t are observed just as those in R_{11} . K -scaling is shown to characterize $G_{\Omega_{22}}$ at high K . By combining M -scaling and K -scaling, an universal scaling is proposed and capture the transition. Similar to R_{11} , the effects of anisotropy in turbulence on the amplification are negligible.

V.C Kolmogorov Length Scale and Viscous Dissipation

Energy cascade in turbulence are dictated by viscous dissipation from the large eddies down to the smallest eddies. During the process of cascade, large eddies break down to smaller ones and lose energy to temperature. Classical turbulence theory has indicated that the smallest eddies are described by the Kolmogorov length scale at which most dissipation takes place. Increasing turbulence intensity would intensify the dissipation and the flow, in response, would further develop much smaller eddies. Just like the shock thickness indicates a clear condition of the shock, Kolmogorov

scales tell us essential information of energy spectrum and the overall conditions of the turbulence. Since shock thickness is generally smaller than turbulent length scales, the two-way coupling between the shock and the turbulence should begins at the small eddies at which the eddies' scales are close to δ_l . By studying the change of Kolmogorov length scale and dissipation in STI, we can better understand how turbulence evolves through the shock and how energy transfer changes during the interactions. In §II.D, Figure II.4 has shown that x_{1_η} and x_{1_ϵ} agree well with the conventional x_1 . So do x_{2_η} and x_{2_ϵ} agree well with x_2 . Therefore, in this section we will continue using the conventional locations, x_1 and x_2 , in the discussions of η and ϵ .

Figure V.8 shows the distributions of Kolmogorov length scale at different M_t . Due to viscous decay at the upstream, the values of η increase toward x_1 . Inside the shock, the shock compression transfers energy into turbulence resulting in significant reduction of η . After turbulence leaves the shock at x_2 the flows are once again subjected to dissipation, and thus, postshock η immediately increases. A clear trend of M_t is observed in the distributions, higher M_t leads to smaller peak inside the shock. The reasonable explanation for this is shock waves are weakened by turbulence, and thus, weaker shocks lead to smaller turbulent production.

Contrary to η , the distributions of ϵ show exactly opposite trend in figure V.9. Viscous decay causes the decrease of ϵ while shock compression results in a peak inside the shock. Higher the M_t smaller the peak is due to weakened shock by the turbulence. Compared to the values of the peak in η , much stronger peaks are observed in ϵ . This comes from the scaling law that $\epsilon \sim \mu\omega^2$ while $\eta \sim \omega^{1/2}$.

Some attempts were made to quantify the amplification of η and ϵ in the litera-

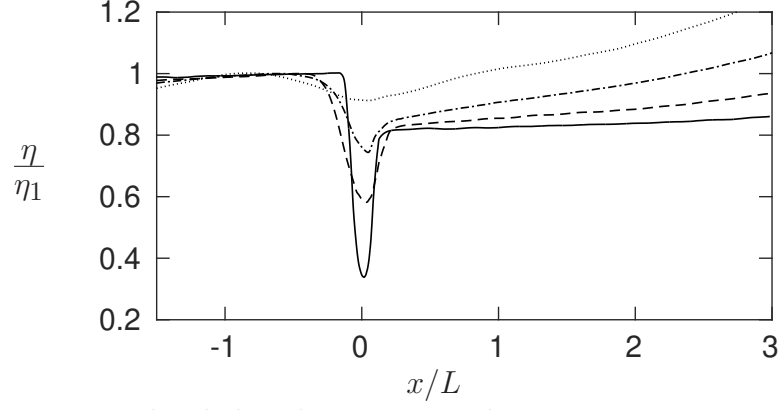


Figure V.8: Normalized distributions η with $M = 1.2$, $R_\lambda \approx 25$ and $M_t = 0.12$ (solid), 0.21 (dashed), 0.32 (dash-dotted) and 0.44 (dotted).

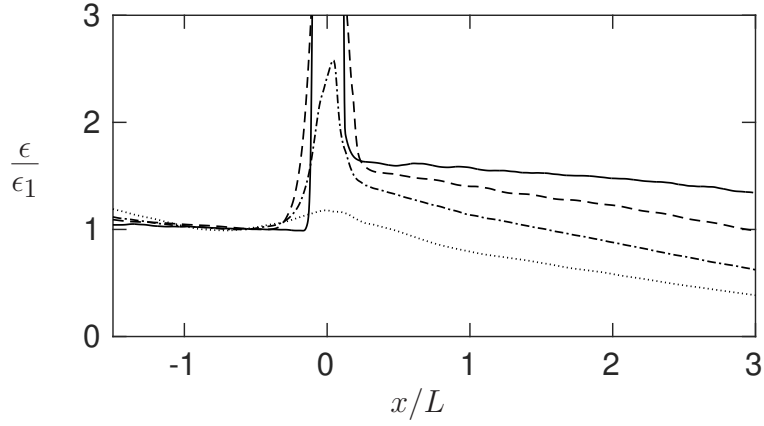


Figure V.9: Normalized distribution ϵ with $M = 1.2$, $R_\lambda \approx 25$ and $M_t = 0.12$ (solid), 0.21 (dashed), 0.32 (dash-dotted) and 0.44 (dotted).

ture. Larsson & Lele (2009) and Larsson *et al.* (2013) proposed that the change of η is a function of M based on RH relations and RDT. But the observed discrepancies between DNS data and the theory suggest a systematic trend of other mechanisms that the amplification depends on. In Sinha (2012); Vemula & Sinha (2017), the amplification of ϵ was discussed. A clear discrepancy was also observed between DNS data and LIA. Though new turbulence models proposed in the Vemula & Sinha (2017) improve the estimate, the discussions only focused on the trend of M without exploring the change of turbulent states. Overall, there still lacks a good method to quantify the amplification of Kolmogorov length scale and viscous dissipation in the literature. Since K has successfully characterized R_{11} and Ω_{22} , same method is repeated in the hope of a good scaling. However, there exists some scatter when G_η and G_ϵ are plotted against K . Compared to R_{11} and Ω_{22} , η and ϵ are quantities in small scales while both Reynolds stresses and vorticities are intermediate scales. Such difference may suggest the conditions on which K is applicable. Further investigations are required to capture the scaling for Kolmogorov length scale and dissipation.

V.D Mass Flux Variance

Flow compressibility is associated with the density changes which in general can be characterized by the mean Mach number. In a turbulent flow, thus, we expect the local mass flux, $(\rho u_1)^2$, to present fluctuations due to fluctuations in both density and velocity. When such a turbulent flow approaches a stationary shock wave, fluctuations in mass flux are expected to be affected in vicinity of the shock. Such variation of mass flux in return indicates the effects of compressibility generated by both the turbulence and the shock.

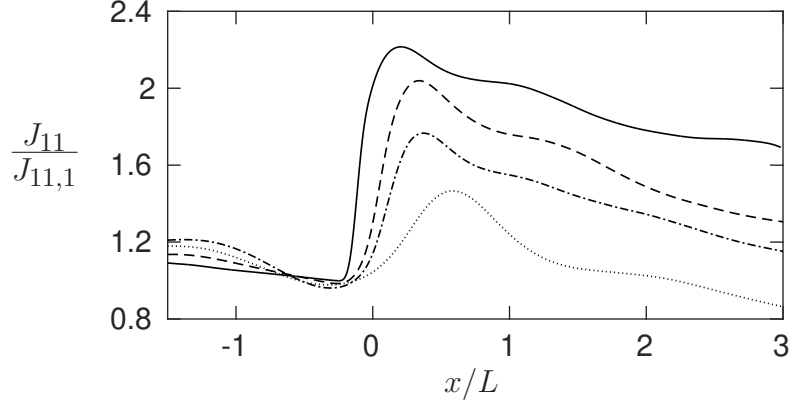


Figure V.10: Normalized distributions of J_{11} with $M = 1.2$, $R_\lambda \approx 25$ and $M_t = 0.12$ (solid), 0.21 (dashed), 0.32 (dash-dotted) and 0.44 (dotted).

Figure V.10 shows the normalized distributions of J_{11} at different M_t . We can clearly see that the variation of mass flux share a very similar distribution with the transverse components of enstrophy. Such similarity also exists in transverse components mass flux which are not shown here. After a monotonic decay in the upstream, J_{11} is amplified by shock compression, followed by another monotonic decay in postshock evolution. The postshock peak observed in R_{11} does not exist in both Ω_{22} and J_{11} . A close look of the figure reveals that the amplification of J_{11} is much higher than R_{11} and Ω_{22} . Such strong amplification implies different mechanisms dominate the evolution that have not been discussed before.

The amplification of J_{11} are measured from $x_{1J_{11}}$ and $x_{2'J_{11}}$ which are the local minimum and maximum. Figure V.11 shows the amplification across the shock. Similar to R_{11} and Ω_{22} , a very good collapse is obtained by plotting J_{11} against K . A scaling law of $G_{J_{11}} \approx 0.77K^{-3/4}$ is observed at high K . With decreasing K , J_{11} from different M seem to approach to different asymptotic values as $K \rightarrow 0$. These asymptotes suggest a M -scaling. However, the variation of mass flux has never been

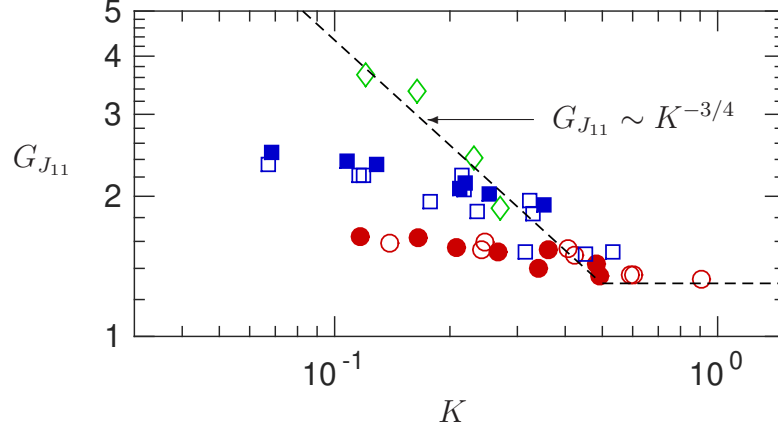


Figure V.11: Amplification factors of J_{11} with $M = 1.2$, $R_\lambda \approx 25$ and $M_t = 0.12$ (solid), 0.21 (dashed), 0.32 (dash-dotted) and 0.44 (dotted).

discussed in STI and there is no related works in LIA. Based on such circumstances, an universal scaling for J_{11} is currently unavailable and the transition between M -scaling and K -scaling is pending for further investigations. The distributions of J_{11} and Ω_{22} are very similar, one difference between the two is there seems to exist another asymptotic state of J_{11} at high K as shown in figure V.11. Though shock compression would eventually be surpassed by turbulent motions at high K and the amplification under this condition would be dominated by viscosity. Such conditions requires deeper discussion on the evolution of J_{11} and dominant budgets.

Flow statistics provided by experiments are important to verify the numerical results. However, unlike simulations, accurate measurements are usually restricted to limited variables, such as J_{11} . In STI, accurate measurements relies on pinpointing the quantities of interest along the streamwise direction, which is very difficult due to small shock thickness. Such strict requirement makes experimental data very limited. In light of this situation, the following discussion intends to further experimental

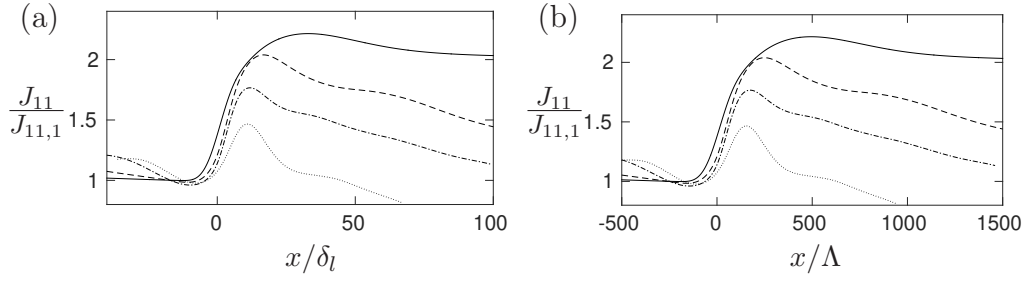


Figure V.12: Distributions of J_{11} normalized by (a) laminar shock thickness and (b) mean free path with $M = 1.2$, $R_\lambda \approx 25$ and $M_t = 0.12$ (solid), 0.21 (dashed), 0.32 (dash-dotted) and 0.44 (dotted).

measurements.

Considering the fluctuations in turbulence, it is difficult to measure the related length scales. However, other scales, such as laminar shock thickness and mean free path, pose less challenge since their values only depend on the mean flows. Laminar shock thickness is given as $\delta_l = 2k_1\mu/(\rho c\Delta M)$ while mean free path is $\Lambda = 2/3k_1\mu/(\rho c)$, which can also be written as $\Lambda = \Delta M\delta_l/3$ (Thompson, 1984). Figure V.12 shows the J_{11} with normalization of laminar shock thickness and mean free path. In part (a), the figure shows that turbulence has made the shock thicker more than tenfold. The location of $x_{2'_{J11}}$ in which downstream maximum is measured is ten to thirty times of δ_l away from the shock. Such turbulent thickening is also observed in part (b) with normalization of mean free path. The figure shows that the turbulent shock can be five hundred times of a mean free path, and $x_{2'_{J11}}$ is two hundreds to five hundreds downstream of mean free path from the shock. In figure V.13, we present the the distance from x_1 to $x_{2'_{J11}}$. In general, we see that $x_{2'_{J11}}$ is further downstream than $x_{2'_{R11}}$ regardless of the turbulence conditions. Since δ_l and Λ are both quantities that depends on the mean flow conditions, the systematic

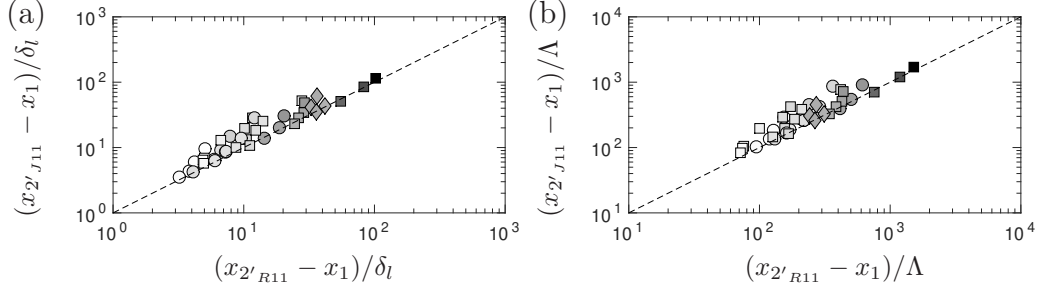


Figure V.13: Location of maximum J_{11} downstream of the shock ($x_{2'J11}$) relative to x_1 normalized by (a) laminar shock thickness and (b) mean free path with $M = 1.1$ (circles), $M = 1.2$ (squares) and $M = 1.4$ (daimonds). Dashed lines with slope for reference. Different tones of grays represent different values of R_λ .

change of $x_{2'J11}$ cannot be accurately estimated as we can see there is some scatter of the data. Attempts of presenting the distance with $M_t/\Delta M$ and K are made but a consistent trend has not been obtained. Further investigations are encouraged.

V.E Thermodynamic Quantities

An important feature of compressible turbulence comes from the fluctuations in thermodynamic variables. Such fluctuations play a crucial role in energy transfer, flow compressibility, thermal equilibrium, among other things. From the derivation of turbulent shock jumps in §III.B, we have shown that the nonlinearity in thermodynamic variables can significantly modify the stationary state of the flow. Thus, a discussion of thermodynamic fluctuations are given here.

Traditionally, thermodynamic fluctuations are normalized by their corresponding ensemble averages (Lee *et al.*, 1993; Donzis & Jagannathan, 2013). Since isentropic relations are satisfied in general as discussed in §III.B, the conventional normalizations of different variables are correlated by the ploytropic exponent as shown in Eq. (III.49). Present studies propose a normalization by upstream fluctuations as

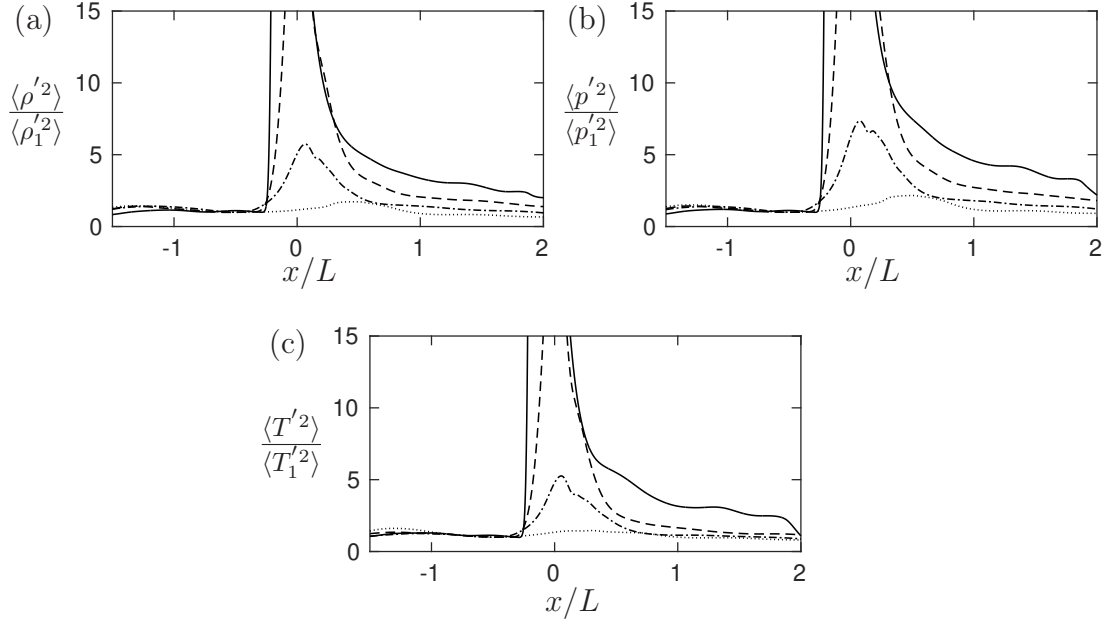


Figure V.14: Normalized distributions of (a) $\langle \rho'^2 \rangle$, (b) $\langle p'^2 \rangle$ and (c) $\langle T'^2 \rangle$ with $M = 1.2$, $R_\lambda \approx 25$ and $M_t = 0.12$ (solid), 0.21 (dashed), 0.32 (dash-dotted) and 0.44 (dotted).

shown in Figure V.14. The presented distributions are density, pressure and temperature, respectively. A detailed comparison reveals that different thermodynamic fluctuations share very similar distributions. Such similarity was also reported in the corresponding p.d.f. and skewness by Donzis & Jagannathan (2013). These phenomena suggest a very strong correlation between the three variables. It also implies that if a thermodynamic state is given, the following change of the state can be estimated by just one variable. Though there are different mechanisms involved in each variable, there may exist mutual terms that dominates the evolutions. Finally, We note here that a good scaling of thermodynamic amplification was not obtained by K from present simulations. Further studies of the corresponding budgets are required for deeper discussion.

V.F Summary

Turbulence amplification due to shock compression is studied by analyzing the quantities of interest across the shock. A clear K -scaling is found in many variables, such as Reynolds stresses, enstrophy and the mass fluxes at strong turbulence. Meanwhile, M -scaling is observed as $K \rightarrow 0$ from LIA. In light of the two scaling laws, an universal scaling is proposed along with a transitional K that distinguish the two laws. The observed K dependence shows a dominant role of Reynolds number. However, a good collapse by K -scaling was not found in the amplification of Kolmogorov length scale, viscous dissipation and thermodynamic variables. Since both Kolmogorov length scale and dissipation are quantities in small eddies very different from Reynolds stresses for example. Such difference in scales implies different mechanisms are involved that play a role in the processes.

VI. CONCLUSIONS AND FUTURE WORK

VI.A Conclusions

The presence of shock waves is a distinguishing feature of supersonic/hypersonic flows. Understanding the processes in which turbulence interacts with a shock is fundamentally important to engineering application of compressible turbulence. The main challenge of studying this topic comes from the two-way coupling between the shock and turbulence which occurs at a wide range of scales in time and space. In this work, the studies focus on the canonical interaction of turbulent flows and a stationary normal shock. An inhouse compressible turbulence code is developed with high-fidelity method for simulating a shock in a numerical domain. To understand the generality of STI, both isotropic and anisotropic turbulence were simulated by different methods. A large STI database with one of the highest resolutions in the literature is built with a wide range of R_λ ($5 - 65$) and M_t ($0.02 - 0.54$), along with various values of M ($1.1 - 1.4$) to thoroughly study the systematic change in the shock and turbulence.

Theoretical work applying to turbulent shocks is formulated assuming quasi-equilibrium. Under such an assumption, the shock responds instantaneously to local changes in upstream conditions due to turbulent fluctuations. The shock can, therefore, be quantified based on laminar theories and the statistical description of turbulence. When turbulent fluctuations are strong enough, the flow can become subsonic and significant changes are expected in the local behavior at the shock location. Different formula are adopted to characterize the flows in supersonic and

subsonic regions. Finally, the solutions of turbulent shock jumps are expressed in terms of M and M_t compared to RH jumps which depend solely on M . Our simulations and other data in the literature agree well with the theoretical predictions and we argued that while R_λ does not appear in the final expressions, this may indeed be justified from the analysis of the governing equations in the one-dimensional limit. The effect of anisotropy in the incoming turbulence also appears to be negligible on mean jumps, again supporting the basic tenets behind QE. The analytical results apply well both in the wrinkled and broken regimes due to the different treatments of supersonic and subsonic regions ahead of the shock. This is accounted for by recognizing that the relation between downstream and upstream variables depends on whether the flow is supersonic or subsonic locally: RH conditions only apply to the former. Interestingly, though, departures from RH jumps of mean variables are seen even in the wrinkled regime due to the non-linear functional form of RH jumps which, when averaged, result in values different than RH jumps using mean properties ahead of the shock. Note that this effect is missing when linearized RH jumps are used in theories such as LIA. Furthermore, in the latter, mean properties are considered known boundary conditions to the problem at the mean Mach number M . Our results, consistent with other DNS in the literature, do not support this assumption which may be, in part, responsible for LIA being unable to capture the observed behavior beyond weak fluctuations. This change in mean properties has also relevance for practical applications where shock stabilization in a turbulent environment is critical such as flows in supersonic nozzles or in scramjet engines. It can also provide guidance in designing stationary STI experiments and simulations as an incorrect back pressure will lead to drifting shocks.

The theoretical results based on QE were further found to provide quantitative predictive capabilities. For example, we found that turbulence can weaken (as argued before in the literature) but can also strengthen the shock jumps depending on a critical Mach number M_{cr} defined here which in turns depend on the intensity of turbulent fluctuations through M_t . For $M < M_{cr}$, jumps are stronger than in laminar flows at the same M ; for $M > M_{cr}$ jumps are weaker. Furthermore, we found that density, pressure and temperature present different critical Mach numbers giving raise to conditions in which temperature jumps are larger than RH while density and pressure jumps are weaker than RH. These predictions have indeed been verified with our DNS data here. Entropy, on the other hand, shows a distinct feature of monotonic increase without critical Mach number. Such change is found dominated mostly by turbulence intensities in agreement with weak shock theory.

Thus we conclude that collectively the data support QE as a good approximation which leads to analytical results for density, pressure, temperature and entropy, consistent with the available data. In fact, it is interesting to observe how well it performs even with highly broken shocks where three-dimensional effects could play a role. We also note that QE is not expected to be accurate for variables at locations beyond $x_{2'}$ where turbulent—as opposed to shock—processes dominate the dynamics. It is also unclear whether derivations under QE are applicable to, e.g., variances of thermodynamic quantities. This is part of ongoing efforts.

While shock jumps are modified by turbulence, the structure of the shock is also changed accordingly. This is quantified by studying the rms-to-mean dilatation on the shock. Present simulations showed a dependence of $M_t/\Delta M$ of dilatation in wrinkled regime consistent with the theory proposed previously. Departures of DNS

data from the theory were seen for $M_t/\Delta M \gtrsim 0.6$ where stronger turbulent effects create increasingly large areas with holes. At much higher $M_t/\Delta M$, an asymptotic value of Θ was observed which depends on R_λ . This was explained by the fact that at high turbulence intensities, transverse diffusion becomes important to which dilatation is subjected to. Thus classical results on turbulence gradients were used to obtain Θ_∞ as $M_t/\Delta M \rightarrow \infty$ which exhibits quantitative agreement with DNS data. Traditionally, the category for shock structure depends on visual inspection. In wrinkled regime, each local dilatation line shows a clear sharp peak resulting from the shock. Such peaks become smooth in broken regime but still prominent compared to other minor peaks generated from the turbulence. As turbulent intensity continues increasing, the interactions would eventually be dominated by turbulent motions. Under this circumstances, the dilatation no long shows a dominant shock peak. Rather, multiple similar peaks appear in dilatation. In the meanwhile, Reynolds stresses show pure viscous decay across the shock. Vanished shock is proposed for these phenomena which happen at $K \approx 1$.

Finally, we presented results on turbulence amplification due to the shock. The amplification in STI was widely studied by focusing on various variables of turbulence, hydrodynamics and thermodynamics. The previously proposed parameter K ($= \delta_l/\eta$) was used on this quantitative assessment. A large collection of results in the literature, and our simulations was presented. The new simulations in this studies covered a wide range of parameters and extended the results in the literature to interactions at much higher K . The amplification factor that measures the change of streamwise Reynolds stress across a shock was shown to be characterized by K when the turbulence is strong. The factor decreases with K as shock compression dimin-

ishes by turbulent motions. At limiting cases $K \rightarrow 0$, the factor shows a M -scaling. Such dependence on two parameters in two different limits was suggested to resemble Widom scaling in critical phenomena. In the present context, its application leads to universality of the form $GK^{1/4} = f_2(K^{3/2}\Delta M)$ which indeed collapses all the data with no systematic trend observed against any other governing parameter. This led to a transition criterion ($K_{tr} \approx 0.03/\Delta M^{2/3}$) between low- K and high- K interactions which separates interactions on which LIA applies and when $G \sim K^{-1/4}$ applies, respectively. Similar phenomena were found in the amplification of transverse enstrophy where the amplifications are captured by K and M at different conditions. A universal scaling is proposed thereafter with the form $G_{\Omega_{22}}K^{3/4} = f_4(K^{15/16}\Delta M)$. Although the amplification of streamwise mass flux also shows a K -scaling at high turbulence intensities, the lack of discussion in LIA has hindered deeper discussion of a universal scaling. Similar K -scaling was not found in the amplifications of Kolmogorov length scale, viscous dissipation and thermodynamic variables. Compared to Reynolds stresses and enstrophy, both Kolmogorov length scale and dissipation are much smaller quantities. Such differences in scales implies different processes are involved in each variable. The thermodynamic fluctuations normalized by upstream values showed extremely similar distributions which has never been reported. The resemblance implies that the changes of thermodynamic variables are highly correlated, and the interactions are in thermodynamic equilibrium in general. The surprising results warrant further investigations for this topic.

VI.B Future Work

In this section, we proposed possible research topics that can be extended from the present studies.

- Analytical solutions have successfully estimated the thermodynamic jumps in turbulent shock waves. With accurate estimation, one must understand the dominant mechanisms by which the turbulent jumps are dominated. The non-monotonic trends in some quantities implies complex processes involved. In addition, different variables show transition from greater-than-RH jumps to weaker jumps at different conditions. These trends imply very complicated dependence on shock waves and turbulence at different regimes. It is encouraged to explore the mechanisms that dominate the shock jumps.
- The change of shock structure has been captured by Mach numbers in wrinkled regime. For the dilatation in broken shocks, the asymptotic states are captured by Reynolds number at very strong turbulence. Meanwhile, the transition between the two regimes depends on both the shock waves and turbulence and has not been captured yet. The systematic trend of dilatation in broken regime is still unclear because of insufficient understanding of velocity dilatation in turbulence. Further investigations on the velocity derivatives in turbulence are required to understand the local dilatation that turbulence dominates. That gives us a comprehensive understanding of the processes in subsonic regions.
- The theoretical work in present studies relies heavily on QE. With increasing turbulence intensities, QE would be eventually invalid. Its validity is actually challenged by few cases in present simulations in which discrepancies are ob-

served between the data and the proposed predictions. Plausible explanation for the discrepancies is that transverse dissipation becomes evident and interactions between the infinitesimal laminar shocks occur subjected to viscosity. Such effects of transverse diffusion was actually seen in the dilatation that DNS data depart earlier from the presented theory with lower Reynolds number. To further describe the turbulent shock beyond the conditions on which QE is inapplicable, a good description of shock-shock interactions is inevitable.

- Systematic trends of amplifications across the shock in various quantities on R_λ and M_t are discussed. Good prediction of Reynolds stresses, enstrophy and mass fluxes are obtained by K . However, quantities in small scales and thermodynamic fluctuations show different trends that are still elusive. Further efforts are needed to conclusively establish scaling laws for Kolmogorov length scale, viscous dissipation and thermodynamic variables.

REFERENCES

- AGUI, J. H., BRIASSULIS, G. & ANDREOPOULOS, Y. 2005 Studies of interactions of a propagating shock wave with decaying grid turbulence: velocity and vorticity fields. *J. Fluid Mech.* **524**, 143–195.
- ANDREOPOULOS, Y., AGUI, J. H. & BRIASSULIS, G. 2000 Shock wave-turbulence interactions. *Annu. Rev. Fluid Mech.* **32**, 309–345.
- BARENBLATT, G. I. 2003 *Scaling*. Cambridge: Cambridge Univ. Press.
- BARRE, S., ALEM, D. & BONNET, J. P. 1996 Experimental study of a normal shock/homogeneous turbulence interaction. *AIAA J.* **34**, 968–974.
- BATCHELOR, G. K. 1953 *The Theory of Homogeneous Turbulence*. Cambridge University Press.
- BOUKHARFANE, R., BOUALI, Z. & MURA, A. 2018 Evolution of scalar and velocity dynamics in planar shock-turbulence interaction. *Shock Waves* .
- CHAPMAN, D. R. & RUBESIN, M. W. 1949 Temperature and velocity profiles in the compressible laminar boundary layer with arbitrary distribution of surface temperature. *Journal of the Aeronautical Sciences* **16** (9), 547–565.
- CHEN, C. H. & DONZIS, D. A. 2018 Shock-turbulence interactions at high turbulence intensities. *J. Fluid Mech.* p. under review.
- CHERTOCH, A. E. & ABARBANEL, S. S. 2000 Strict stability of high-order compact implicit finite-difference schemes: the role of boundary conditions for hyperbolic pdes. *J. Comp. Phys.* **160**, 42–66.
- DONZIS, D. A. 2012a Amplification factors in shock-turbulence interactions: effect

- of shock thickness. *Phys. Fluids* **24**, 011705.
- DONZIS, D. A. 2012*b* Shock structure in shock-turbulence interactions. *Phys. Fluids* **24**, 126101.
- DONZIS, D. A. & JAGANNATHAN, S. 2013 Fluctuations of thermodynamic variables in stationary compressible turbulence. *J. Fluid Mech.* **733**, 221–244.
- DONZIS, D. A., SREENIVASAN, K. R. & YEUNG, P. K. 2005 Scalar dissipation rate and dissipative anomaly in isotropic turbulence. *J. Fluid Mech.* **532**, 199–216.
- FREUND, J. B. 1997 Proposed inflow/outflow boundary condition for direct computation of aerodynamic sound the vorticity jump across a shock in a non-uniform flow. *AIAA* **35** (4), –384.
- GATSKI, T. B. & BONNET, J-P. 2009 *Compressibility, turbulence and high speed flow*. Elsevier.
- GOLDENFELD, N. 2006 Roughness-induced critical phenomena in a turbulent flow. *Phys. Rev. Lett.* **96** (044503).
- GRANT, H. L. & NISBET, I. C. T. 1957 The inhomogeneity of grid turbulence. *J. Fluid Mech.* **2** (3), 263–272.
- HANNAPPEL, R. & FRIEDRICH, R. 1995 Direct numerical-simulation of a Mach-2 shock interacting with isotropic turbulence. *Appl. Sci. Res.* **54**, 205–221.
- HESSELINK, L. & STURTEVANT, B. 1988 Propagation of weak shocks through a random medium. *J. Fluid Mech.* **196**, 513–553.
- HONKAN, A. & ANDREOPOULOS, J. 1992 Rapid compression of grid-generated turbulence by a moving shock-wave. *Phys. Fluids* **4** (11), 2562–2572.
- HUETE, CÉSAR, JIN, TAI, MARTÍNEZ-RUIZ, DANIEL & LUO, KUN 2017 Interaction of a planar reacting shock wave with an isotropic turbulent vorticity field. *Phys.*

- Rev. E* **96**, 053104.
- INOKUMA, K., WATANABE, T., NAGATA, K., SASOH, A. & SAKAI, Y. 2017 Finite response time of shock wave modulation by turbulence. *Phy. Fluids* **29** (5), 051701.
- JACQUIN, L., CAMBON, C. & BLIN, E. 1993 Turbulence amplification by a shock wave and rapid distortion theory. *Phy. Fluids* **3**, 2539.
- JAGANNATHAN, S. & DONZIS, D. A. 2016 Reynolds and mach number scaling in solenoidally-forced compressible turbulence using high-resolution direct numerical simulations. *J. Fluid Mech.* **789**, 669–707.
- JAMME, S., CAZALBOU, J.-B., TORRES, F. & CHASSAING, P. 2002 Direct numerical simulation of the interaction between a shock wave and various types of isotropic turbulence. *Flow, Turb. Comb.* **68**, 227–268.
- JIMENEZ, J. 1998 Turbulent velocity fluctuations need not be Gaussian. *J. Fluid Mech.* **376**, 139–147.
- JOHNSEN, E., LARSSON, J., BHAGATWALA, A. V., CABOT, W. H., MOIN, P., OLSON, B. J., RAWAT, P. S., SHANKAR, S. K., SJÖGREEN, B., YEE, H. C., ZHONG, X. & LELE, S. K. 2010 Assessment of high-resolution methods for numerical simulations of compressible turbulence with shock waves. *J. Comp. Phys.* **229**, 1213–1237.
- KEVLAHAN, N. K.-R. 1997 The vorticity jump across a shock in a non-uniform flow. *J. Fluid Mech.* **341**, 371–384.
- KITAMURA, T., NAGATA, K., SAKAI, Y. & ITO, Y. 2016 Rapid distortion theory analysis on the interaction between homogeneous turbulence and a planar shock wave. *J. Fluid Mech.* **802**, 108–146.
- KOVASZNAVY, L. S. G. 1953 Turbulence in supersonic flow. *J. Aeronaut. Sci.* **20** (10),

657–674.

- LARSSON, J., BERMEJO-MORENO, I. & LELE, S. K. 2013 Reynolds- and Mach-number effects in canonical shock-turbulence interaction. *J. Fluid Mech.* **717**, 293–321.
- LARSSON, J. & LELE, S. K. 2009 Direct numerical simulation of canonical shock/turbulence interaction. *Phys. of Fluids* **21**, 126101.
- LEE, S., LELE, S. K. & MOIN, P. 1993 Direct numerical simulation of isotropic turbulence interacting with a weak shock wave. *J. Fluid Mech.* **251**, 533–562.
- LEE, S., LELE, S. K. & MOIN, P. 1997 Interaction of isotropic turbulence with shock waves: effect of shock strength. *J. Fluid Mech.* **340**, 225–247.
- LELE, S. K. 1992*a* Compact finite-difference schemes with spectral-like resolution. *J. Comp. Phys.* **103**, 16–42.
- LELE, S. K. 1992*b* Shock-jump relations in a turbulent flow. *Phys. Fluids* **4** (12), 2900–2905.
- LIVESCU, D. & RYU, J. 2016 Vorticity dynamics after the shock–turbulence interaction. *Shock Waves* **26** (3), 241–251.
- MAHESH, K., LEE, S., LELE, S. K. & MOIN, P. 1995 Interaction of an isotropic field of acoustic waves with a shock wave. *J. Fluid Mech.* **300**, 383–407.
- MAHESH, K., LELE, S. K. & MOIN, P. 1997 The influence of entropy fluctuations on the interaction of turbulence with a shock wave. *J. Fluid Mech.* **334**, 353–379.
- MAHESH, K., MOIN, P. & LELE, S. K. 1996 The interaction of a shock wave with a turbulent shear flow. *Tech. Rep.*. Stanford.
- MOHAMED, M. S. & LARUE, J. C. 1990 The decay power law in grid-generated turbulence. *J. Fluid Mech.* **219**, 195–214.

- MOIN, P. & MAHESH, K. 1998 Direct numerical simulation: A tool in turbulence research. *Annu. Rev. Fluid Mech.* **30**, 539–578.
- MONIN, A. S. & YAGLOM, A. M. 1975*a* *Statistical Fluid Mechanics, Vol I*. MIT Press.
- MONIN, A. S. & YAGLOM, A. M. 1975*b* *Statistical Fluid Mechanics, Vol. II*. MIT Press.
- MOORE, F. K. 1954 Unsteady oblique interaction of a shock wave with a plane disturbance. *Tech. Rep.*. NACA Report 1165.
- NOULLEZ, A., FRISCH, U., WALLACE, G., LEMPert, W. & MILES, R.B. 1997 Transverse velocity increments in turbulent flow using the relief technique. *J. Fluid Mech.* **339**, 287–307.
- Obukhov, A. M. 1949 The structure of the temperature field in a turbulent flow. *Izv. Akad. Nauk. SSSR* **13**, 58–69.
- POINSOT, T. J. & LELE, S. K. 1992 Boundary conditions for direct simulations of compressible viscous flows. *J. Comp. Phys.* **101**, 104–129.
- POPE, S. B. 2000 *Turbulent Flows*. Cambridge University Press.
- QUADROS, R., SINHA, K. & LARSSON, J. 2016*a* Kovasznay mode decomposition of velocity-temperature correlation in canonical shock-turbulence interaction. *Flow Turbulence Combust* **97**, 787–810.
- QUADROS, R., SINHA, K. & LARSSON, J. 2016*b* Turbulence energy flux generated by shock/homogeneous-turbulence interaction. *J. Fluid Mech.* **796**, 113–157.
- RIBNER, H. S. 1954*a* Convection of a pattern of vorticity through a shock wave. *NACA TR-1164* .
- RIBNER, H. S. 1954*b* Shock-turbulence interaction and the generation of noise.

NACA TR-1233 .

- RYU, J. & LIVESCU, D. 2014 Turbulence structure behind the shock in canonical shock-vortical turbulence interaction. *J. Fluid Mech.* **756**.
- SAGAUT, P. & CAMBON, C. 2008 *Homogeneous Turbulence Dynamics*. Cambridge: Cambridge University Press.
- SCHUMACHER, J., SCHEEL, J. D., KRASNOV, D., DONZIS, D. A., YAKHOT, V. & SREENIVASAN, K. R. 2014 Small-scale universality in fluid turbulence. *Proc. Natl. Acad. Sci.* **111** (30), 10961–10965.
- SCHUMACHER, J., SREENIVASAN, K. R. & YAKHOT, V. 2007 Asymptotic exponents from low-Reynolds-number flows. *New. J. Phys.* **9**, 89.
- SINHA, KRISHNENDU 2012 Evolution of enstrophy in shock/homogeneous turbulence interaction. *J. Fluid Mech.* **707**, 74–110.
- TANAKA, K., WATANABE, T., NAGATA, K., SASOH, A., SAKAI, Y. & HAYASE, T. 2018 Amplification and attenuation of shock wave strength caused by homogeneous isotropic turbulence. *Phy. Fluids* **30** (3), 035105.
- TAYLOR, G. I. 1935 Turbulence in a contracting stream. *Z. Angew. Math. Mech.* **15**, 91–96.
- THOMPSON, P. A. 1984 *Compressible Fluid Dynamics*. New York: McGraw Hill.
- TRUEDELLE, C. 1952 On curved shocks in steady plane flow of an ideal fluid. *J. Aeronaut. Sci.* **19** (12), 826–828.
- VELIKOVICH, A. L., HUETE, C. & WOUCHUK, J. G. 2012 Effect of shock-generated turbulence on the hugoniot jump conditions. *Phys. Rev. E* **85**, 016301.
- VEMULA, JAGADISH BABU & SINHA, KRISHNENDU 2017 Reynolds stress models applied to canonical shock-turbulence interaction. *Journal of Turbulence* **18** (7),

653–687.

WIDOM, B. 1965 Equation of state in the neighborhood of the critical point. *J.*

Chem. Phys. **43** (11), 3898–3905.

WILLIAMS, J. E. FFOWCS & HOWE, M. S. 1973 On the possibility of turbulent thickening of weak shock waves. *J. Fluid Mech.* **58** (3), 461–480.

WILLIAMSON, J. H. 1980 Low-storage Runge-Kutta schemes. *J. Comp. Phys.* **35**, 48 – 56.

WOUCHUK, J. G., DE LIRA, C. H. R. & VELIKOVICH, A. L. 2009 Analytical linear theory for the interaction of a planar shock wave with an isotropic turbulent vorticity field. *Phys. Rev. E* **79**, 066315.

YAKHOT, V. & DONZIS, D. A. 2017 Emergence of multiscaling in a random-force stirred fluid. *Phys. Rev. Lett.* **119**, 044501.

YAKHOT, V. & DONZIS, D. A. 2018 Anomalous exponents in strong turbulence. *Phys. D* p. under review.

ZANK, G. P., ZHOU, Y., MATTHAEUS, W. H. & RICE, W. K. M. 2002 The interaction of turbulence with shock waves: A basic model. *Phys. Fluids* **14**, 3766–3774.

ZELDOVICH, Y. B. & RAIZER, Y. P. 2002 *Physics of Shock Waves and High-Temperature Hydrodynamic Phenomena*. Dover Publications, Inc., Mineola, New York, USA.

APPENDIX A

EXPLICIT SOLUTIONS OF LIA

A breakthrough in the theoretical study of STI was LIA (Ribner, 1954*a,b*; Moore, 1954) in which it is assumed an inviscid flow, and linear superposition of perturbations. LIA was found accurate at moderately low Mach number and weak turbulence (Lee *et al.*, 1993; Larsson & Lele, 2009; Ryu & Livescu, 2014). With increasing turbulent fluctuations, discrepancy between LIA and DNS data appears. Nevertheless, LIA provides analytical predictions in STI that can indeed account for e.g. turbulence amplification. The rest of the section focuses on the amplification of other quantities that can be derived within LIA. For more details about LIA, readers are referred to Wouchuk *et al.* (2009) in which explicit expressions of turbulence amplification are provided.

In figure A.1 we show the general setup. Upstream of the shock turbulence is assumed to be incompressible. The normal shock travels through the domain

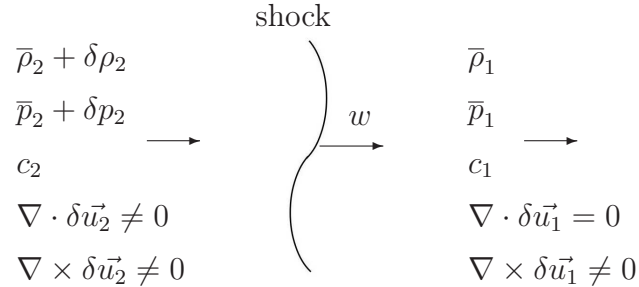


Figure A.1: A normal shock wave travels from the left to the right at a speed w . The flow at the upstream is assumed incompressible while the downstream consists of solenoidal and dilatational motions.

at a speed w , and interacts with the upstream turbulence creating a downstream turbulence with different characteristics. The subscript 1 refers to the quantities upstream of the shock, subscript 2 refers to the quantities downstream of the shock, and δ means perturbations. Before interacting with the shock, the upstream fields consist of rotational motions only. As the shock passes through the domain, it modifies the original velocities and generates dilatational motions. Without proof, the amplification factor can be expressed as

$$\begin{aligned}
G &= \frac{\delta u_{2x}^2}{\delta u_{1x}^2} \\
&= A_{3D}^{rot}(M) + A_{3D}^{ac}(M) \\
&= A_{3D}^l(M) + A_{3D}^s(M) + A_{3D}^{ac}(M)
\end{aligned} \tag{A.1}$$

where the subscript $_{3D}$ indicates the upcoming flow is three-dimensional, superscript rot and ac stand for solenoidal and acoustic contributions, and superscript l and s represent the amplification from long and short wavelength, respectively. For the solenoidal motions, LIA separates the wavelength into long wavelength ($\zeta_0 < 1$) and short ones ($\zeta_0 > 1$) where ζ_0 is a dimensionless frequency that takes account of the periodicity of the upstream velocity field

$$\zeta_0 = \frac{RM_2}{\sqrt{1 - M_2^2}} \frac{k_x}{k_y}. \tag{A.2}$$

M_2 is the downstream Mach number obtained from RH relations, R is the RH jump for density, and k_x and k_y are the longitudinal and transverse wave numbers. Short wavelength is the waves that run downstream with constant amplitude while the waves with long wavelength emitted from the shock decay exponentially relative to the shock position. The amplifications from the long and short wavelength are given

as

$$A_{3D}^l = \frac{1}{2} \int_0^1 \frac{|Q_{rot}^l|^2 M^4 R^2 \sqrt{M^2 - 1}}{[RM^2 + (M^2 - 1)\zeta_0^2]^{5/2}} d\zeta_0 \quad (\text{A.3})$$

and

$$A_{3D}^s = \frac{1}{2} \int_1^\infty \frac{|Q_{rot}^s|^2 M^4 R^2 \sqrt{M^2 - 1}}{[RM^2 + (M^2 - 1)\zeta_0^2]^{5/2}} d\zeta_0. \quad (\text{A.4})$$

Q_{rot}^l and Q_{rot}^s are the amplitudes of downstream velocities associated with the long and short wavelength, respectively,

$$|Q_{rot}^l|^2 = \frac{\Omega_1^2 2\Omega_1 \Omega_2 e_{lr} + \Omega_2^2 (e_{lr}^2 + e_{li}^2)}{\left(1 + \frac{1-M_2^2}{M_2^2} \zeta_0^2\right)^2} \quad (\text{A.5})$$

and

$$|Q_{rot}^s|^2 = \frac{\Omega_1^2 2\Omega_1 \Omega_2 e_s + \Omega_2^2 e_s^2}{\left(1 + \frac{1-M_2^2}{M_2^2} \zeta_0^2\right)^2} \quad (\text{A.6})$$

where Ω_1 quantifies the amplification of the upstream vorticity and Ω_2 comes from shock oscillations due to upstream perturbations. The two terms are given as

$$\Omega_1 = \frac{(\gamma + 1) M^2}{(\gamma - 1) M^2 + 2} + \frac{M^2 - 1}{M^2} \zeta_0^2 \quad (\text{A.7})$$

and

$$\Omega_2 = \frac{(M^2 - 1) \sqrt{2\gamma M^2 - \gamma + 1}}{M^2 [(\gamma - 1) M^2 + 2]^{3/2}} \quad (\text{A.8})$$

where the coefficients are

$$e_{lr} = \frac{2M^2 M_2 [M^2 - (M^2 + 1)\zeta_0^2] \alpha_0}{4M^4 M_2^2 \zeta_0^2 (1 - \zeta_0^2) + [M^2 - (M^2 + 1)\zeta_0^2]^2}, \quad (\text{A.9})$$

$$e_{li} = \frac{4M^4 M_2^2 \zeta_0 \sqrt{1 - \zeta_0^2} \alpha_v}{4M^4 M_2^2 \zeta_0^2 (1 - \zeta_0^2) + [M^2 - (M^2 + 1)\zeta_0^2]^2}, \quad (\text{A.10})$$

$$e_s = \frac{2M^2 M_2 \alpha_v}{4M^4 M_2^2 \zeta_0^2 (1 - \zeta_0^2) + [M^2 - (M^2 + 1)\zeta_0^2]^2}, \quad (\text{A.11})$$

and

$$\alpha_v = \frac{2}{\gamma + 1} \left(\frac{M^2 - 1}{M} \zeta_1^2 - 1 \right). \quad (\text{A.12})$$

Finally, the acoustic contribution A_{3D}^{ac} accounts for acoustic motions generated by the shock and is given as

$$A_{3D}^{ac} = \frac{1}{2} \int_1^\infty \frac{|Q_{ac}|^2 M^4 R^2 \sqrt{M^2 - 1}}{[RM^2 + (M^2 - 1)\zeta_0^2]^{5/2}} d\zeta_0 \quad (\text{A.13})$$

where

$$Q_{ac} = \left[\frac{M_2 \zeta_0 - \sqrt{\zeta_0^2 - 1}}{\zeta_0 - M_2 \sqrt{\zeta_0^2 - 1}} \right]^2 e_s^2 \quad (\text{A.14})$$

Given from Eq. (A.1) to Eq. (A.14), the amplification factor is a function that depends solely on the mean Mach number, M .

Similar to Reynolds stresses, the amplification of vorticity is defined as the vorticity ratio at x_2 and x_1 which consists of the long and short wavelength parts

$$\begin{aligned} G_{\Omega_{22}} &= \frac{\delta \omega_{2z}^2}{\delta \omega_{1z}^2} \\ &= \int_0^1 [\Omega_1^2 + \Omega_2^2 (e_{lr}^2 + e_{li}^2) + 2\Omega_1 \Omega_2 e_{lr}] \sin^5 \theta d\zeta_0 \\ &\quad + \int_1^\infty [\Omega_1^2 + \Omega_2^2 e_s^2 + 2\Omega_1 \Omega_2 e_s] \sin^5 \theta d\zeta_0 \end{aligned} \quad (\text{A.15})$$

where the first term on the right hand side comes from the long wavelength while the second term is the contribution from the short wave length. $\theta = k_x/k_y$ is the incidence angle that defines a set of upstream waves with different directions with

respect to the shock. Each term also takes account of the amplification of upstream vorticity and shock oscillations. The amplification of vorticity can be written as a function of M as well.

A main conclusion for all LIA predictions is that turbulence amplification is completely quantified by the single parameter M . Such dependence is consistent with the assumptions behind the analyses, namely, inviscid flows and weak perturbations. These assumptions are reasonable with low turbulence intensities as observed in the good agreement between DNS data and LIA (Larsson & Lele, 2009; Ryu & Livescu, 2014).